Route-based time-dependent life-cycle carbon and NOx emissions analysis of heavy-duty trucks

By

Arnav Sinha

A thesis submitted in partial fulfillment of

the requirements for the degree of

Master of Science

(Mechanical Engineering)

at the

UNIVERSITY OF WISCONSIN-MADISON

2024

Abstract

The electrification of the transportation sector is gaining traction due to the potential for greenhouse gas (GHG) emissions reductions to combat climate change. Class-8 trucks are a major contributor to emissions within this sector; therefore, battery-electric (BE) alternatives with zero tailpipe emissions are being considered as a replacement. However, a more comprehensive analysis of vehicle emissions must be conducted to cover the entire lifecycle of a vehicle. Hence, a life cycle analysis (LCA) can be used to evaluate emissions from all phases during a truck's life. The current literature lacks studies conducted on Class-8 trucks, time-of-day impact on GHG emissions from electricity generation, and nitrogen oxide (NO_x) emissions. Therefore, this thesis aims to investigate the potential carbon dioxide (CO_2), and NO_x emissions reductions achieved with battery electric (BE) and series-hybrid (SHE) trucks when compared to a conventional diesel internal combustion engine (ICE) Class-8 truck along a long-haul and two drayage routes. In this work, a dynamic and modular vehicle simulation tool was developed to simulate the performance and emissions of said powertrains. Additionally, the LCA accounted for emissions contributions and uncertainties from production, maintenance, fuel production, electricity generation, and distribution. The emissions from charging the BE truck are assessed under different assumptions: the US average grid, a time-dependent electricity grid based on the truck routes, and a future grid assumption applied to the same. The time-dependent route-based analysis accounts for regional and time-of-day variations in the electricity grid mix and its impact on the resultant emissions. The future grid assumption took the increase in the use of renewable sources of electricity over ten years into account. The LCA results show that BE trucks are well suited for operation on more stop-and-go routes within regions with a large share of renewable sources of electricity, emitting 23% and 6% less CO_2 and NO_x respectively than the SHE truck during drayage application in

California (CA). On the other hand, SHE trucks are best for cross-country trips on highways and operations in regions with large shares of electricity from non-renewable sources. The SHE truck emitted 36% and 46% less CO_2 and NO_x respectively than the BE truck during long-haul transport. After considering future grid emissions reduction from 2023-2032, the BE truck's emissions were reduced by 10-12% compared to the ICE truck. Despite this reduction, the BE truck had greater emissions during long-haul and drayage transport in a more carbon-intensive region than the SHE truck.

Acknowledgments

I would like to acknowledge a few individuals who were instrumental in me completing this study and my degree. I would like to thank my advisor Professor Kokjohn for his guidance and for the research opportunity at the University of Wisconsin – Madison. The HEART simulation toolbox project was key in my development as an engineer. I will remember to always question my results thanks to Professor Kokjohn. Next, I would like to thank Dr. Harsh Sapra for taking time out of his busy schedule to provide prompt assistance and feedback. I was able to greatly improve my visual and verbal presentation skills during my time as a master's student thanks to his feedback.

I would like to acknowledge some of the Engine Research Center's (ERC) students, current and former, staff, and faculty. I am grateful to Dr. Aravindh Viswanathan and Saurabh Gupta for helping me get settled in a research environment, Joshua Leach for assistance in technical matters, and Professor Rothamer and Ghandhi for agreeing to be on my committee and providing constructive criticism.

I would like to thank The U.S. Army Combat Capabilities Development Command Army Research Laboratory for supporting this research. Dr. Constandinos Mitsingas's continued feedback was critical for the continued improvement of the HEART toolbox.

This research was sponsored by the US Army Research Laboratory and was accomplished under Cooperative Agreement Number. The views and conclusions contained in this document are those of the authors and should not be interpreted as representing the official policies, either expressed or implied, of the Army Research Laboratory or the U.S. Government. The U.S. Government is authorized to reproduce and distribute reprints for Government purposes, notwithstanding any copyright notation herein. Lastly, I thank my parents and my partner Grace for all their support and encouragement during times of hardship.

Table of Contents

List of Figures

List of Tables

Introduction

The transportation sector comprised the largest share (28%) of greenhouse gas (GHG) emissions in the US in 2022 [1]. Medium (MD) and heavy-duty (HD) vehicles contributed the second-highest amount of GHG emissions (23%) in the transportation sector [1]. The electrification of these vehicles is seen as a path towards reducing GHG emissions. Battery-electric (BE) trucks are considered an enticing alternative to conventional diesel trucks as they typically release no tailpipe emissions and have a higher powertrain efficiency [2] [3]. As projected by the National Renewable Energy Laboratory (NREL), 69% of CO_2 emissions will be reduced by 2050, and 80% of all medium and heavy-duty vehicles will be converted to BE vehicles [4]. However, tailpipe emissions alone do not tell the entire story of a vehicle's environmental impact and, therefore, a more comprehensive approach should be taken. Life cycle analysis (LCA) can evaluate the potential environmental effects, and the resources consumed throughout a product's lifecycle, covering extraction of raw materials, production, usage, maintenance, and disposal. This method has proven to be a beneficial technique, and it has been commonly accepted in the last two decades [5]. An LCA analysis is crucial when comparing vehicles with different powertrains as the material composition of electric vehicle components such as motors and batteries is quite different than that of a truck powered by a diesel engine [6]. Each material also has its process of extraction and refinement. Additionally, an LCA analysis covers emissions from the upstream processes during vehicle operation such as fuel refining and electricity generation.

1.1. Regional and hourly electricity grid variation

The mix of resources used for generating electricity varies based on the region and time of day. Figure 1.1.1 demonstrates the 2023 electric grid generation resource mix and the corresponding CO_2 emissions intensity of the US average, Indiana, and California. In 2023, the total electricity generated in California consisted of 43% natural gas, 44% renewable sources, 8% nuclear power, and 2% miscellaneous sources such as biomass. On the other hand, the total electricity generated in Indiana consisted of 37% coal, 22% renewable sources, and 41% natural gas [7]. California and Indiana cover the two spectrums of high and low CO_2 emissions intensity in the US, with California and Indiana having average CO_2 emissions intensities in 2023 of 316 g/kWh and 712 g/kWh, respectively.

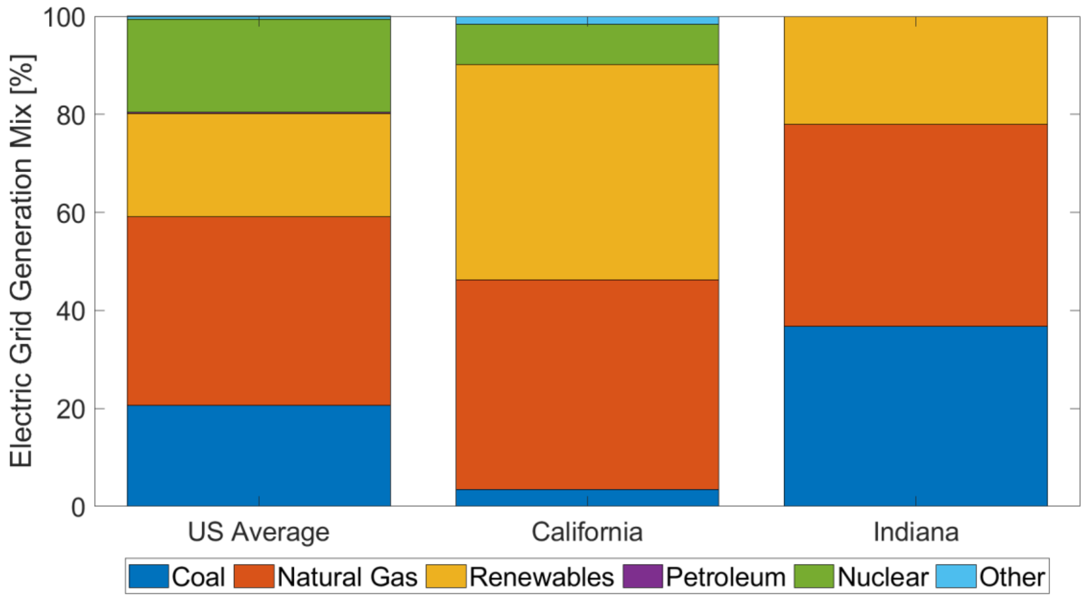

Figure 1.1.1. *Comparison of the 2023 electric grid generation resource mix for a) US Average b) California c) Indiana.*

However, the mix of electricity grid resources also changes throughout the day. The balancing authority of a region controls the grid's resource mix so that the balance of supply and demand for electricity can be maintained safely and economically [8]. Figure 1.1.2 demonstrates the electric grid generation resource mix and CO_2 emissions intensity as a function of time on 07/01/2023 in California with the California Independent System Operator (CISO) balancing authority [9]. During the nighttime hours (8 pm to 5 am), natural gas was the primary source of electric generation. However, during the daytime hours, natural gas usage dropped due to the increased employment of solar energy. Hence, the CO_2 intensity decreased by about 40% from nighttime to noon since solar energy, being a renewable energy source, emits a null amount of CO_2 during operation. In summary, an analysis of regional electricity grid generation mixture with hourly variation revealed that operating and charging the BE truck in different regions and times could have a significant impact on the CO_2 and NO_x emissions when charging the truck. These emissions are likely to decrease in the future as more renewable sources of electricity are employed, the next section will discuss the possible implications of this change.

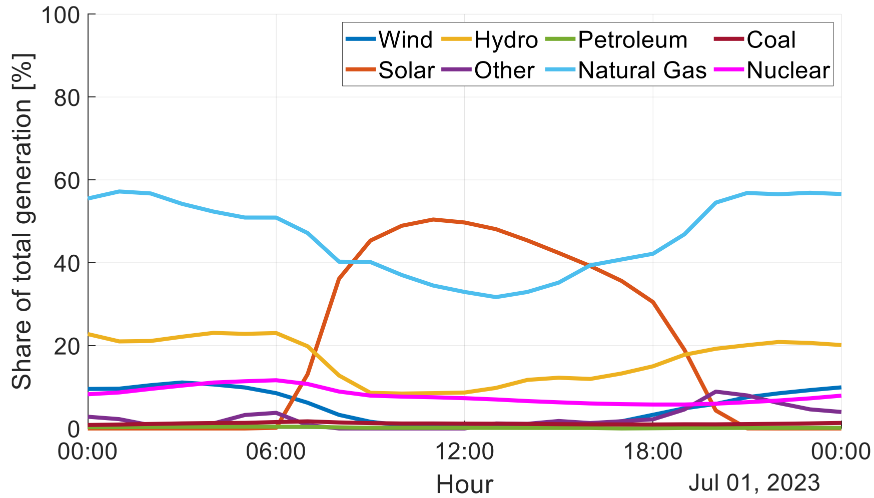

(a)

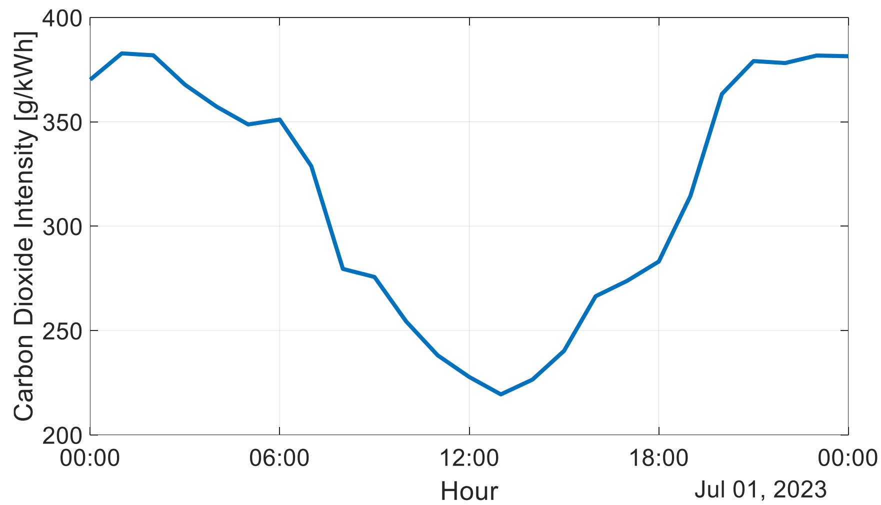

(b)

Figure 1.1.2. *a) Hourly electricity generation mix in California on 07/01/2023 b) CO_2 emissions intensity as a function of time for the same.*

1.2. Impact of future grid mix variation

Coal and natural gas are the two most common electricity generation sources in the US in 2023 [10]. However, the fraction of electricity from coal and natural gas power plants will likely decrease because the electricity grid mix will become less carbon-intensive in the future [11]. Figure 1.2.1 illustrates the US electricity generation projection and shares from selected fuels and renewable sources. The U.S. Energy Information Administration (EIA) expects renewables to surpass natural gas as a source of electricity by 2030. In addition, the EIA predicted that the share of electricity generation from renewables will increase to 26% and that from coal power plants will decrease to 3% by 2050.

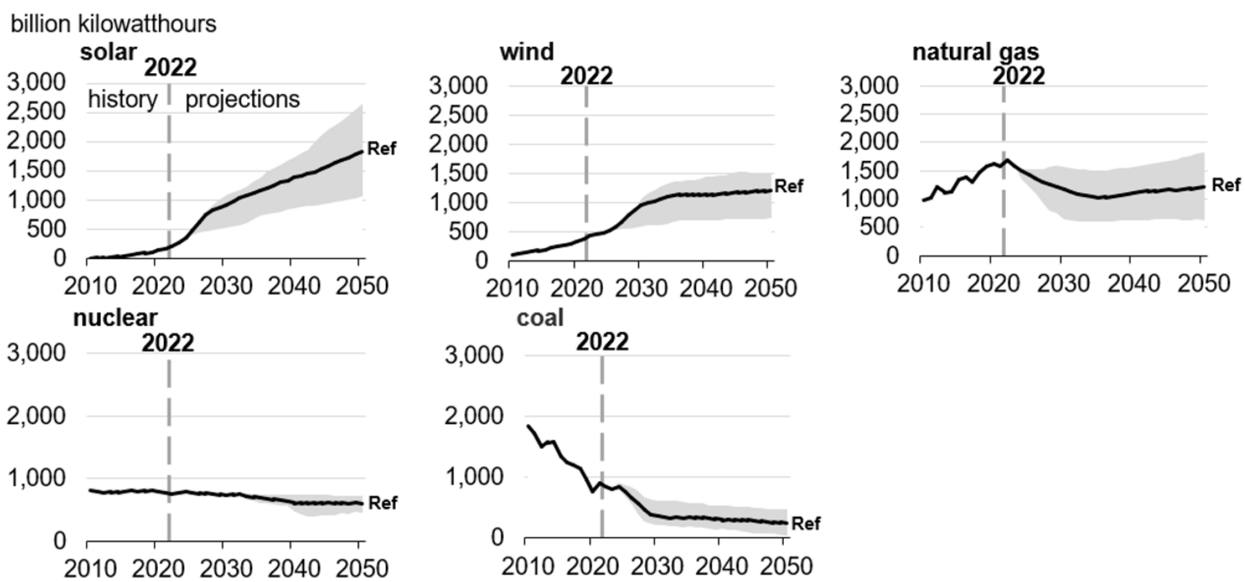

Figure 1.2.1. *Projection of the US electricity generation from selected fuels and renewable sources [11]*

The increased share of electricity from renewable sources will decrease charging or 'Well-to-Tank' (WTT) emissions of a BE truck, thus highlighting their potential for emissions reduction in future transport systems. Therefore, it is crucial to incorporate the future grid mix when comparing emissions from conventional and electrified vehicles.

2. Literature Review

In recent years, emissions analysis of MD and HD vehicles has gained significant research interest. For instance, Iyer et al. [6] performed an LCA of Class 3 to 6 MD vehicles and Class 8 HD trucks. The researchers concluded that a significant decrease in lifetime CO_2 emissions was only seen with electric MD vehicles on a more "stop and go" drive cycle. Marmiroli et al. [12] also came to similar conclusions with light-duty (LD) trucks. The Class-8 sleeper trucks, mostly driving on highways, saw a marginal reduction in freight CO_2 when switching from diesel to BE trucks. This discrepancy was due to the BE truck being unable to take advantage of regenerative braking on highways. This highlighted the importance of testing vehicle models with different drive cycles. However, regional and time-of-day variations in the electricity grid were not accounted for. Lastly, their study did not include hybrid powertrains despite showing great potential.

Boggio et al. [13] noted that hybrid trucks can reduce emissions by 30% compared to diesel in their WTW CO_2 emissions analysis. The hybrid trucks demonstrated a great increase in range over the diesel and BE trucks. This can help save time by reducing the number of refueling stops. However, this study only looked at WTW emissions rates from MD trucks in Europe. It is crucial to consider the emissions from producing battery packs for the SHE and BE trucks. Zhao et al. [14], in their study of MD trucks, noted that BE trucks only had a marginal reduction in CO_2 emissions compared to diesel trucks. The study concluded that in the BE truck's case, the CO_2 emissions had only moved upstream to battery production and electricity generation. Espinoza et al. [14] arrived at a similar conclusion: vehicle production and maintenance phase are the largest contributors to a BE truck's lifetime CO_2 emissions.

Some LCA studies have accounted for regional variation in the electricity grid and its impact on electric vehicles' emissions. Zhao et al. [15] conducted a multi-region LCA study on MD and refuse trucks and concluded that BE vehicles did not see a reduction in CO_2 emissions in regions with significant use of coal for electricity generation such as the American Midwest. Kelly et al. [16] and Sen et al. [17] came to a similar conclusion and noted that coal use reduction for electricity generation is vital to making electric Class 8 trucks more viable. However, both studies assumed that the BE trucks were charging within one region. Class 8 trucks often travel cross country encountering widely varying electricity grid mixes on a single route. Additionally, these studies did not use a route-based analysis and assumed the average electricity source mix for each region which is not an accurate representation of the electricity grid as shown in section 1.1.

As discussed in section 1.1, the electricity grid is likely to become less emissions-intensive in the future and therefore some studies have included this assumption in their LCA. Kelly et al. [16] concluded that by 2035, BE Class 8 trucks showed over a 50% reduction in LCA CO_2 emissions compared to a 2022 diesel equivalent. Short and Crownover [18], arriving at a similar conclusion, noted about a 20% decrease in CO_2 emissions for BE trucks from 2021 to 2030. Both studies, however, presented some shortcomings, only average grid mixes were assumed for the BE truck instead of a route-based time-dependent grid, and neither study considered uncertainties in parameters such as fuel and battery production emissions and were limited to CO_2 emissions only.

The EPA has set ultra-low NO_x emissions standards for HD trucks made in the year 2027 or later at 0.035 g NO_x/bhp-hr which is about an 80% reduction from the standards over 20 years ago [19]. Therefore, it is critical to evaluate the potential NO_x emissions reduction from switching to BE and hybrid trucks. Liu et al. [20] compared the well-to-wheel (WTW) GHGs and criteria pollutants between BE and diesel Class 8 trucks. They found that the BE truck demonstrated a 35-78% reduction in WTW NO_x emissions, across multiple regional grid mixes in the US, compared to the ICE truck. Their study, however, excluded emissions from the production phase. Marmiroli et al. [12] conducted an LCA of light-duty (LD) trucks in Italy and noted that BE trucks had the highest photochemical oxidation potential dominated by emissions from producing the battery pack. Photochemical oxidants are secondary pollutants formed by sunlight acting on NO_x and reactive hydrocarbons [21]. However, their study was limited to LD trucks in Italy with an average electricity grid mix. Additionally, uncertainties in the results were not considered in either study.

The above literature review highlights some gaps that need to be addressed, which are discussed as follows. There have been limited LCA studies conducted on Class-8 trucks in the US. The few that exist often do not account for uncertainties in emissions such as Iyer et al. [6]. Many studies do not have their BE truck's specifications based on a real-world equivalent such as in the case of Sen et al. [17] and Kelly et al. [16]. Additionally, very few studies include Class-8 hybrid trucks, despite being a potentially critical step towards electrification while the charging infrastructure for BE trucks catches up. There is also a need to consider the variation in electricity generation based on the time of day, region of operation, and driving routes. Although LCA studies have begun to acknowledge the regional variation in electricity generation, they do not consider the variation in the electricity grid based on the time of day and trucking routes. The novelty of this paper is the incorporation of a route-based time-dependent electricity grid for BE charging emissions calculation, inclusion of a Class 8 hybrid truck as well as an LCA NO_x emissions with an uncertainty analysis. In this paper, Section 3 describes the research methodology followed up by the description of the Simulink powertrain models of the trucks. Section 0 covers the trucking routes, and truck specifications with the BE truck's specifications being based on the Tesla Semi. This is followed up by an explanation of the route-based time-dependent charging analysis of the BE truck. The uncertainty analysis parameters are summarized in **Error! Reference source not found.**.

3. Research Methodology

This study used a dynamic vehicle powertrain simulation tool to simulate the performance of three different class 8 trucks based on drive cycle data provided as input. Using a route-based time-dependent approach, the simulation results were used to calculate tailpipe, diesel production, and electricity generation emissions. An LCA was performed to incorporate emissions from production and maintenance. Uncertainties with all stages of the LCA were considered by assuming a normal distribution for certain parameters which are tabulated in **Error! Reference source not found.**. Freight emissions analysis was performed to account for the trucks' cargo-carrying capacity. Figure 3.1 shows the steps of the approach employed for this research.

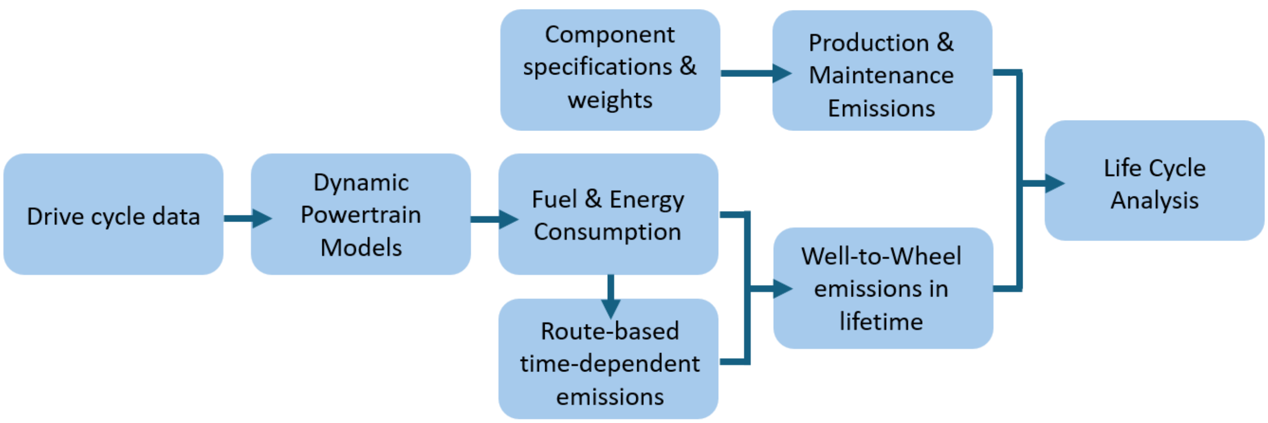

Figure 3.1. *Research methodology.*

3.1. Model Components

All simulations for this study were performed using a dynamic and modular vehicle powertrain simulation tool developed in MATLAB/Simulink [22]. This section describes the individual models that were used to create the powertrain models for the three trucks.

3.1.1. Engine Model

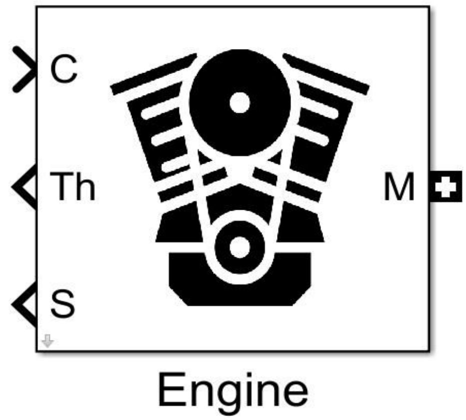

Figure 3.1.1.1. *Internal Combustion Engine (ICE) model in Simulink*

The engine model is a 0-D mean value model. 0-D means time is the only dependent variable [23]. The mean value model implicitly assumes all processes and effects are spread out over the engine cycle by not considering the discrete cycles of the engine [23]. The generic engine model is composed of three subsystem models: the intake model, fuel controller model, and torque calculation model, as demonstrated below.

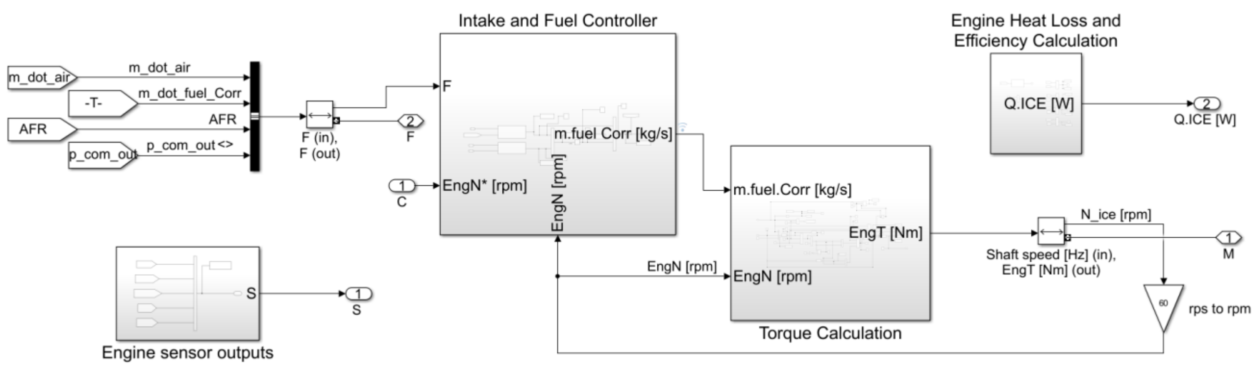

Figure 3.1.1.2 *Internal overview of the engine model in Simulink*

3.1.1.1. Intake System

The engine can be regarded as a volumetric pump in terms of the air system (i.e., a device that forces a volume flow proportionate to its speed) [23]. To calculate the mass flow rate of the compression–ignition (CI) engine, the intake of the generic engine block utilizes a speed–density air mass flow model. The speed–density model uses the speed–density equation to calculate the engine air mass flow rate [24]. The mass flowrate of air is calculated as

$$\dot{m}_{air\_port} = \rho_{in} \times \dot{V}, \tag{3.1}$$

where ρ_{in} is the density of the gas at the engine's intake (related to the intake pressure and temperature by the ideal gas law) and $\dot{V}$ is the volumetric flow rate of air. The density of the intake air is calculated under the ideal gas law as

$$\rho_{in} = \frac{MAP}{R_{air} \times MAT}, \tag{3.2}$$

where MAP is the cycle-averaged intake manifold pressure, R_{air} is the ideal gas constant for the air and burned gas mixture, and MAT is the cycle-averaged intake manifold gas absolute temperature. The volume flow rate of air into the intake system can be defined as

$$\dot{V} = \frac{V_d \times N}{n}, \tag{3.3}$$

where V_d is the engine displaced volume, N is the engine speed, and n is the crankshaft revolutions per power stroke. Therefore, the air mass flow rate of the intake port can be denoted as a function of the intake manifold gas pressure, intake manifold gas temperature, engine speed, displacement of the engine, and the crankshaft revolutions per power stroke, as shown in the equation below. In addition, the air mass flow rate of the intake port is denoted in the intake model as m_dot_port Simulink Function block

$$\dot{m}_{air\_port} = \frac{MAP \times V_d \times N}{n \times R_{air} \times MAT}, \tag{3.4}$$

Volumetric efficiency in an internal combustion engine is defined as the ratio of the air-fuel mixture's mass density drawn into the cylinder at atmospheric pressure to the mass density of the same air volume in the intake manifold during the intake stroke [25]. At full load, the volumetric efficiency is crucial in determining the engine’s capacity to aspirate a mixture of air. Because of the numerous factors that influence it, accurate prediction is quite difficult. Such factors include exhaust gas recirculation (EGR) and ram effects in the intake runner, among others. Therefore, measurements of this number will be necessary for an accurate model.

A two-dimensional map of speed and load generated under steady-state circumstances or thorough fluid dynamic simulations of the intake system are typically used [23]. In this current model, the volumetric efficiency is assumed to be 110%. Accordingly, the actual mass flow rate of air into the engine is equal to the air mass flow rate of the intake port times volumetric efficiency, demonstrated as

$$\dot{m}_{air} = \dot{m}_{air\_port} \times n_{vol}, \tag{3.5}$$

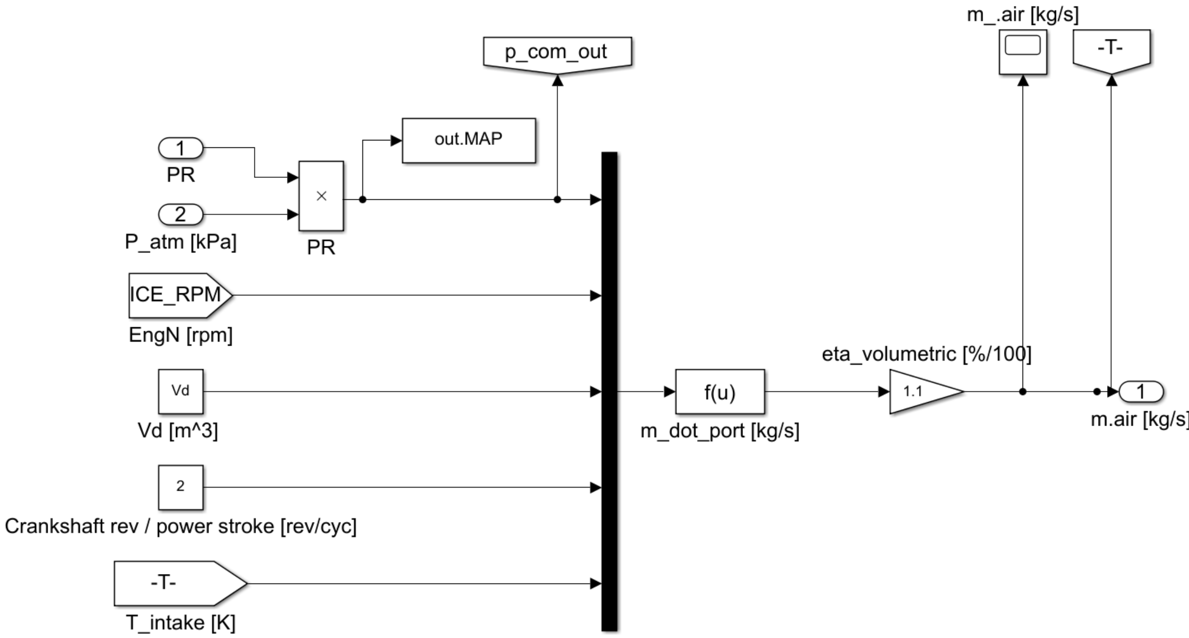

Figure 3.1.1.1.1 *Intake system model in Simulink*

3.1.1.2. Fuel Controller

The fuel controller plays a significant role in the power and torque delivery of the engine. In this model, the fuel controller is modeled from a PI controller. In the fuel controller model, the fuel controller targets the commanded speed and the actual engine speed and eventually applies the correction to provide the required fuel rate. The figure below demonstrates the Simulink fuel controller model.

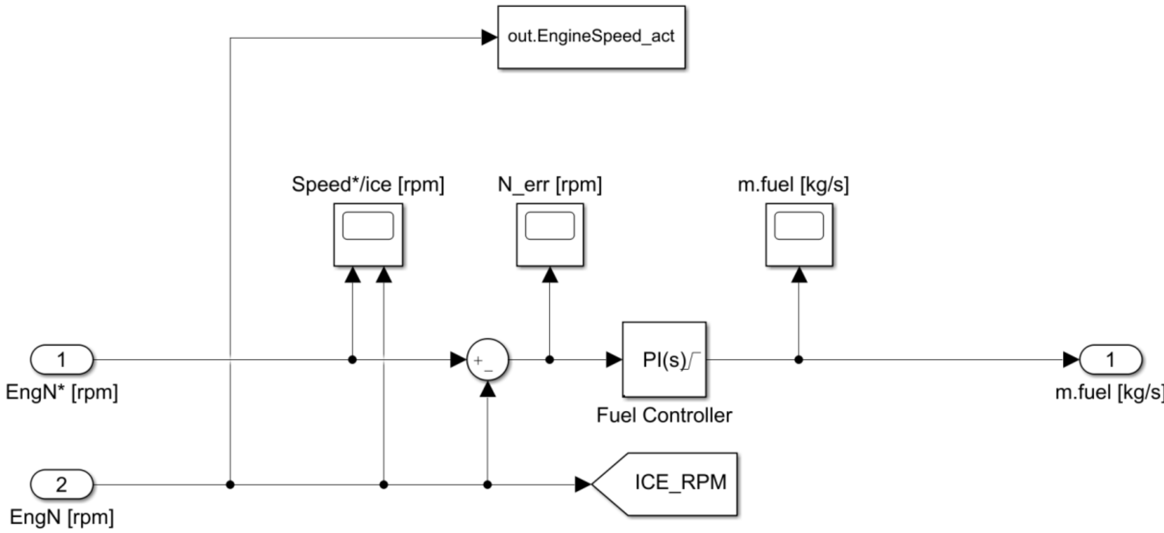

Figure 3.1.1.2.1 *Fuel controller model in Simulink*

3.1.1.3. AFR Controller

As discussed previously, the required mass flow rate of fuel is calculated from the fuel PI controller. Although CI engines combust fuel in a locally rich zone, it is globally lean, which enhances their efficiency. Therefore, an additional saturation block is required to limit the fuel rate to the set air-to-fuel ratio (AFR). In this model, the initial AFR is calculated by dividing the mass flow rate from intake by the mass flow rate from the fuel controller. The corrected AFR can then be limited with a saturation block set with an upper limit of 500 and a lower limit of 17. Eventually, by dividing the mass flow rate from intake to the corrected AFR, the corrected mass flow rate of the fuel can be provided, as shown in the figure below.

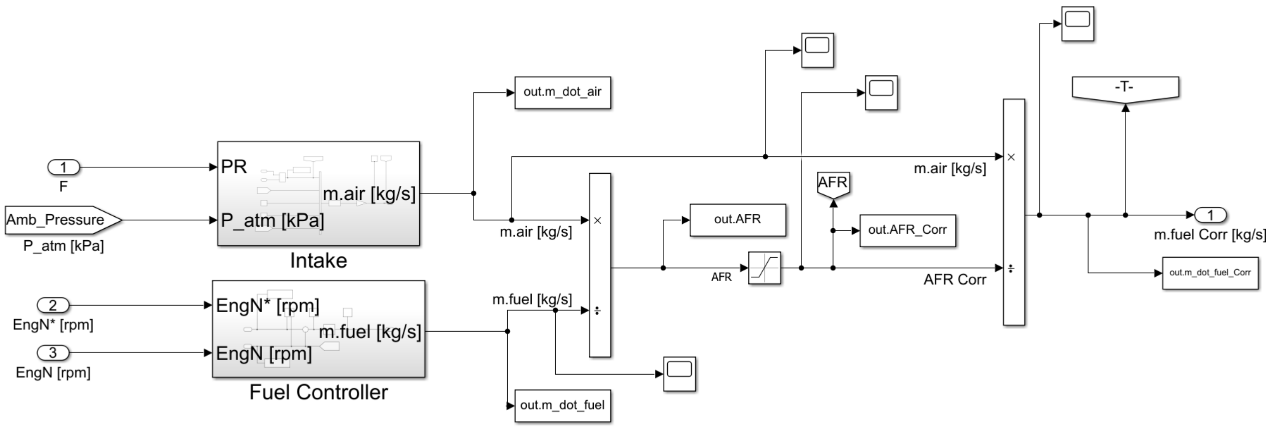

Figure 3.1.1.3.1 *Air-to-fuel ratio (AFR) controller with intake and fuel controllers*

3.1.1.4. Brake Torque Calculation

Since the engine torque mainly depends on engine size, which is referred to as displaced volume V_d, it is advantageous to use a normalized formulation introducing the brake mean effective pressure. This is denoted as

$$BMEP = \frac{2\pi n T}{V_d}, \tag{3.6}$$

where n is the crankshaft revolutions per power stroke, T is the engine torque. Torque can also be denoted as

$$T = \frac{\dot{W}_b}{2\pi N}, \tag{3.7}$$

where $\dot{W}_b$ is the power of the engine, and N is the engine speed. $\dot{W}_b$ can be calculated based on the brake thermal efficiency of the engine, which is given by

$$\dot{W}_b = BTE \times \dot{m}_f \times LHV, \tag{3.8}$$

where BTE is the brake thermal efficiency of the engine, $\dot{m}_f$ is the mass flow rate of the fuel, and LHV is the lower heating value of the fuel. Brake thermal efficiency is the ratio of energy in the brake power to the fuel energy [35], [36]. It contains all losses, including friction loss, pumping loss, exhaust loss, etc. A Sankey diagram of engine efficiency is shown below

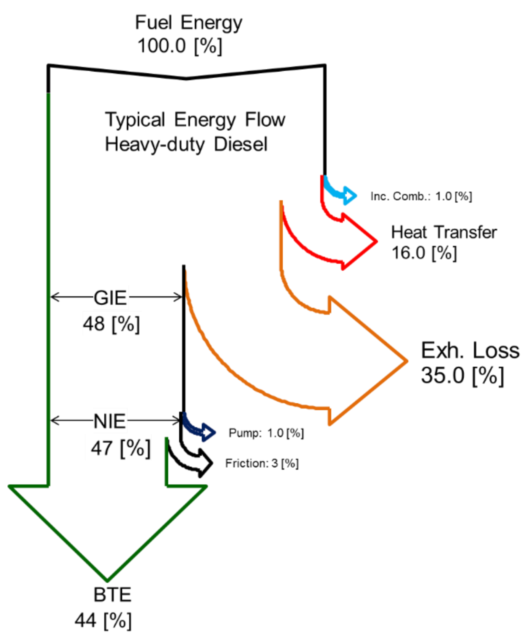

Figure 3.1.1.4.1 *Sankey diagram of engine efficiency*

Using the above figure, BTE can be denoted as

$$BTE = \eta_{mech} \times \eta_{oce} \times GIE, \tag{3.9}$$

where η_{mech} is the mechanical efficiency. It contains all the mechanical losses between the fuel input and power output, including mainly friction losses. It is calculated by dividing brake work and net indicated work, which can also be denoted as the dividend of $BMEP$ and $IMEP_n$. The equation for calculating the η_{mech} is demonstrated below

$$\eta_{mech} = \frac{BMEP}{IMEP_n}, \tag{3.10}$$

$BMEP$, or brake mean effective pressure, is the average pressure forcing down the pistons inside your engine that provides the measured torque output. Like the brake thermal efficiency, $BMEP$ incorporates all the losses. Therefore, $BMEP$ can be calculated by summing up the $FMEP$ and $IMEP_n$, which is the net indicated mean effective pressure that includes the average pressure in the cylinders during the complete four-stroke cycle. The $BMEP$ calculation is demonstrated as

$$BMEP = IMEP_n + FMEP, \tag{3.11}$$

where η_{oce} is the open cycle efficiency, calculated by net indicated work divided by gross indicated work, and it contains the pumping losses. Lastly, GIE is the gross indicated efficiency. It is calculated based on gross work divided by input fuel energy. It contains heat transfer losses, exhaust losses, and incomplete combustion. The open cycle efficiency is calculated as

$$\eta_{oce} = \frac{IMEP_n}{IMEP_g}, \tag{3.12}$$

where $IMEP_g$ is the gross indicated mean effective pressure, which incorporates the average pressure in the cylinders during the compression and the expansion strokes only. $IMEP_n$ is the net indicated mean effective pressure, which includes the average pressure in the cylinders during the complete thermodynamic cycle, in this case, the four-stroke cycle [25]. Since $IMEP_n$ is composed of the complete thermodynamic cycle, it can be calculated by $IMEP_g$ plus $PMEP$, which is the pumping mean effective pressure that incorporates the work per cycle carried out by the piston on the in-cylinder gases during the inlet and exhaust strokes. The calculation of $IMEP_n$ is shown in the equation below. Usually, $PMEP$ is positive for naturally aspirated engines and negative for supercharged and turbocharged engines at high loads. In this model, the $PMEP$ value is assumed to be -1.02% of $IMEP_g$.

$$IMEP_n = PMEP + IMEP_g, \tag{3.13}$$

$IMEP_g$ is the gross work delivered to the piston over the compression and expansion strokes per cycle per unit displaced volume. Therefore, it can be denoted as

$$IMEP_g = \frac{W_g}{V_d}, \tag{3.14}$$

where W_g is the gross work. The gross indicated efficiency, GIE, equals the product of combustion efficiency and *thermodynamic* efficiency and reflects the total work yielded by the combustion of the fuel [25]. GIE can be calculated by W_g over m_f times LHV, and it is demonstrated as

$$GIE = \frac{W_g}{m_f \times LHV}, \tag{3.15}$$

Therefore, according to Equation 3-16, W_g can be calculated as

$$W_g = GIE \times m_f \times LHV, \tag{3.16}$$

Lastly, the fuel mass, m_f, can be calculated from the corrected fuel flow rate provided by the AFR controller. The calculation for calculating the instant fuel mass is shown as

$$m_f = \frac{\dot{m}_{f,corr} \times n \times 60}{N}. \tag{3.17}$$

where $\dot{m}_{f,corr}$ is the corrected fuel flow rate. Accordingly, by combining all the equations mentioned above, the engine's actual torque can be calculated from the fuel flow rate.

3.1.1.5. Turbocharger Model

The turbocharger model is also the 0-D power balance model. The model consists of three main parts: an exhaust manifold, turbine, and compressor, as shown below. The turbine and compressor models are constructed by the power balance equations. The turbocharger modeling is based on the work by Moraal and Kolmanovsky [26]. However, to perform the calculation in the turbine model, several inputs are required. This includes the mass, temperature, specific heat, heat capacity ratio, and pressure of the exhaust. All the values mentioned above were calculated in the exhaust manifold subsystem, as shown in **Error! Reference source not found.**.

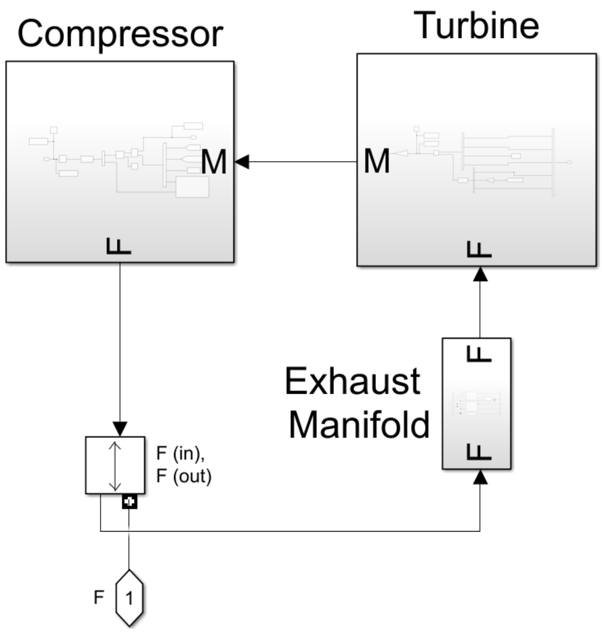

Figure 3.1.1.5.1 *Turbocharger model in Simulink*

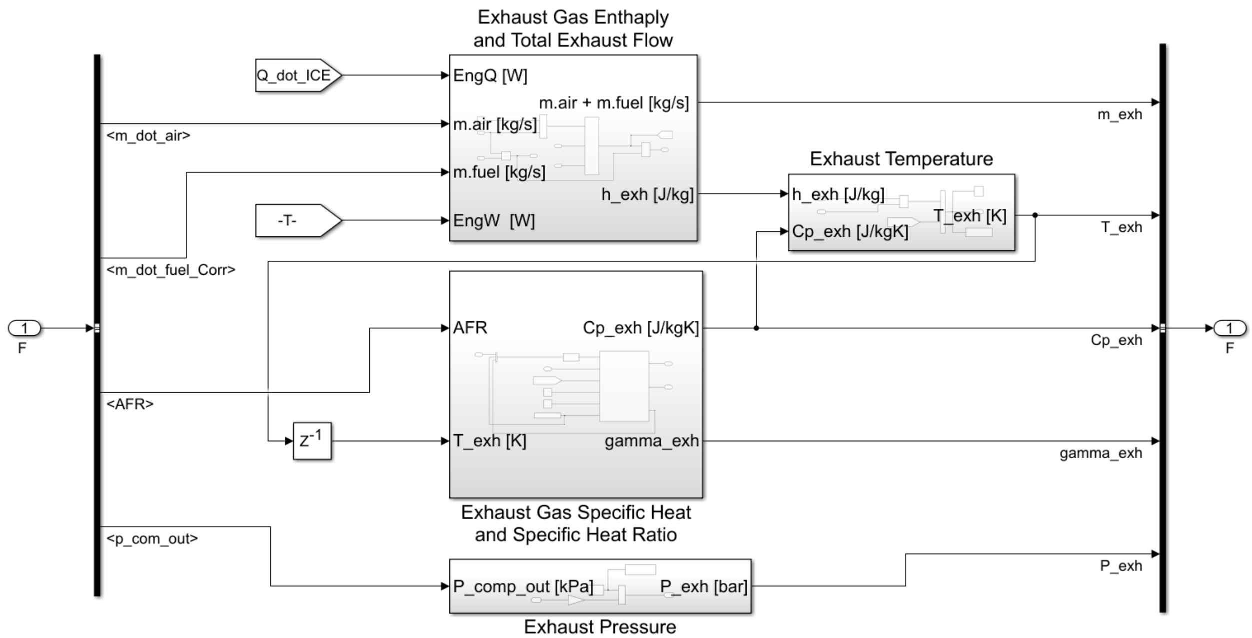

***Figure 3.1.1.5.2** Exhaust manifold model in Simulink*

3.1.1.6. Compressor Model

To boost the engine, it is necessary to obtain the pressure ratio between the compressor inlet pressure and compressor outlet pressure so the intake air can raise the pressure and thereby increase the intake air density. The compressor's power can be obtained from the turbine model with the assumption of certain mechanical efficiency. The mechanical efficiency is set to 98% in this model. The compressor's power is related to the mass flow rate through the compressor and the change of the enthalpy throughout the compressor, according to the first law of thermodynamics. This can be demonstrated as

$$P_{compressor} = \dot{m}_{air} \times \left(h_{c,out} - h_{c,in}\right), \quad (3.18)$$

where $\dot{m}_{air}$ is the mass flow rate of air through the compressor, and $h_{c,in}$ and $h_{c,out}$ are the enthalpies of the compressor inlet and turbine outlet. By assuming constant specific heat coefficients, the compressor power can be calculated as

$$P_{compressor} = \dot{m}_{air} \times c_p \times \left(T_{c,out} - T_{c,in}\right). \quad (3.19)$$

By assuming the isentropic process for the compressor, the temperature ratio can be related to the pressure ratio using the relation below. This means the entropy of the fluid or gas remains constant and can be calculated as

$$\left(\frac{T_{c,out,is}}{T_{c,in}}\right) = \left(\frac{P_{c,out}}{P_{c,in}}\right)^{\frac{\gamma-1}{\gamma}}, \tag{3.20}$$

where γ is the heat capacity ratio, which can also be denoted as $\frac{c_p}{c_v}$. However, since the expansion through the compressor is not isentropic, the isentropic efficiency $0 \leq \eta_{c,is} \leq 1$ of the compressor is introduced. In this study the isentropic efficiency for compressor and turbine is set to 80%. This is shown as

$$\eta_{c,is} = \frac{T_{out,is} - T_{in}}{T_{out} - T_{in}}, \tag{3.21}$$

Combining Equations 3-20 and 3-21 yields

$$\left(\frac{T_{c,out,is}}{T_{c,in}}\right) = 1 + \frac{1}{\eta_{c,is}}\left(\left(\frac{P_{c,out}}{P_{c,in}}\right)^{\frac{\gamma-1}{\gamma}} - 1\right), \tag{3.22}$$

By combining Equations 3-21 and 3-22, the power of the compressor power can be modeled

$$P_c = \dot{m}_{air} \times c_p \times \frac{T_{in}}{\eta_{c,is}}\left(\left(\frac{P_{c,out}}{P_{c,in}}\right)^{\frac{\gamma-1}{\gamma}} - 1\right). \tag{3.23}$$

The implementation of the compressor power equation in Simulink is shown below

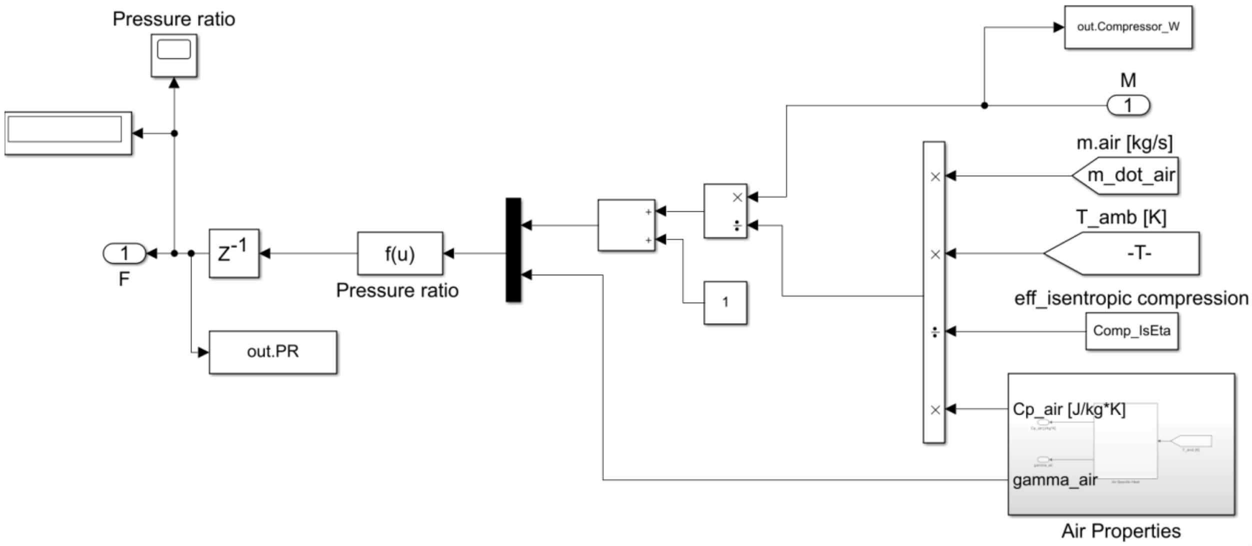

Figure 3.1.1.6.1 *Turbocharger's compressor model in Simulink*

3.1.1.1. Turbine

The power of the turbine is calculated similarly to the compressor model

$$P_{turbine} = \dot{m}_{exh} \times c_p \times \left(T_{t,in} - T_{t,out}\right), \tag{3.24}$$

$$\left(\frac{P_{t,in}}{P_{t,out}}\right)^{\frac{\gamma-1}{\gamma}} = \left(\frac{T_{t,in}}{T_{t,out,is}}\right), \tag{3.25}$$

$$\eta_{t,is} = \frac{T_{in} - T_{out}}{T_{in} - T_{out,is}}, \tag{3.26}$$

By combining equations 3-24, 3-25, and 3-26, the turbine power expression can be obtained. The turbine power expression is denoted as

$$P_{turbione} = \dot{m}_{exh} \times c_p \times \eta_{t,is} \times T_{in}\left(1 - \left(\frac{P_{turbine,in}}{P_{turbine,out}}\right)^{\frac{\gamma-1}{\gamma}}\right). \tag{3.27}$$

The implementation of the turbine power equation in Simulink is shown below

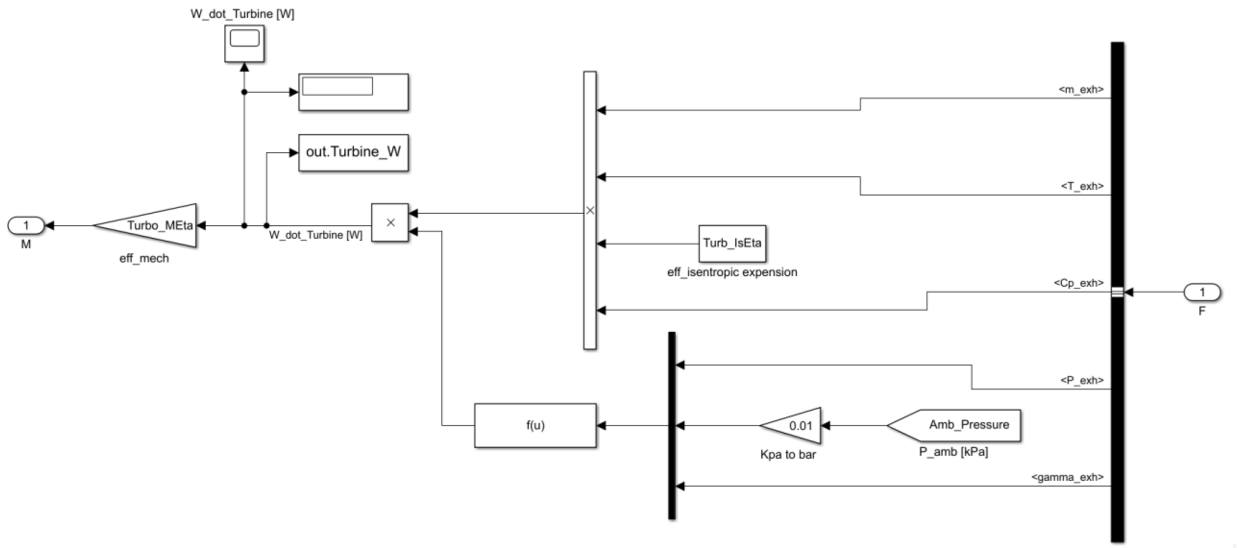

Figure 3.1.1.6.2 *Turbocharger's turbine model in Simulink*

3.1.1.2. Exhaust Manifold

As shown from the turbine calculation above, several inputs are required to perform the turbine power calculation. This includes the mass flow rate, temperature, specific heat, heat capacity ratio, and exhaust pressure. The exhaust mass rate and temperature can be obtained by the engine energy balance calculation. Considering the IC engine as a control volume, the steady-flow energy conservation equation can be written as

$$P_{fuel} = P_{ICE} + \dot{Q}_{ICE} + \dot{Q}_{exh}, \tag{3.28}$$

where P_{fuel} is the energy supply by the fuel, P_{ICE} is the power provided by the CI engine, $\dot{Q}_{ICE}$ is the heat transfer rate to the cooling medium, and $\dot{Q}_{exh}$ is the exhaust heat. P_{fuel} can also be denoted as the product of the mass fuel flow rate and the LHV of the fuel [27]

$$P_{fuel} = \dot{m}_f \times LHV, \tag{3.29}$$

In addition, $\dot{Q}_{exh}$, the energy of the exhaust, is related to the mass flow rate through the exhaust and the total enthalpy change across the exhaust. It is derived from the first law of thermodynamics,

$$\dot{Q}_{exh} = \dot{m}_{exh} \times h_{exh}, \tag{3.30}$$

The mass flow rate of the exhaust can be considered as the total mass (air + fuel). Therefore, the exhaust energy can be written as

$$\dot{Q}_{exh} = \left(\dot{m}_{air} + \dot{m}_{fuel}\right) \times h_{exh}, \tag{3.31}$$

Treating the exhaust gas as an ideal gas with constant specific heat, the exhaust energy is calculated

$$\dot{Q}_{exh} = \left(\dot{m}_{air} + \dot{m}_{fuel}\right) \times c_p \times (T_{exh} - T_{air}). \tag{3.32}$$

where T_{air} is the outside ambient air temperature, T_{exh} is the temperature of the exhaust gas, and c_p is the average specific heat of the air gases at the mean exhaust temperature. By utilizing Equation 3-32, the exhaust temperature and exhaust mass flow rate can be calculated. The implementation of the exhaust temperature and exhaust mass flow rate calculation in Simulink is shown in **Error! Reference source not found.** and **Error! Reference source not found.**

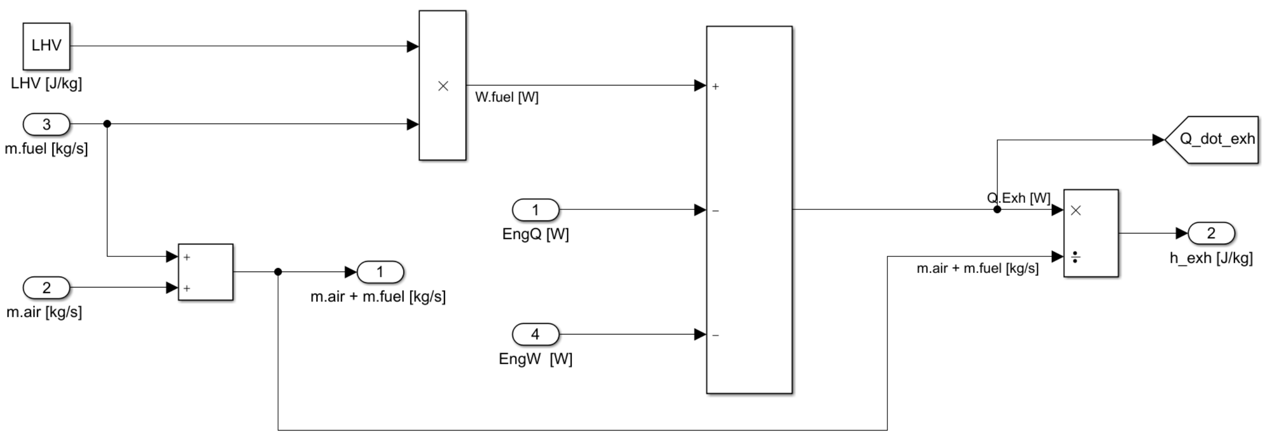

Figure 3.1.1.6.3 *Exhaust gas enthalpy and total exhaust flow model*

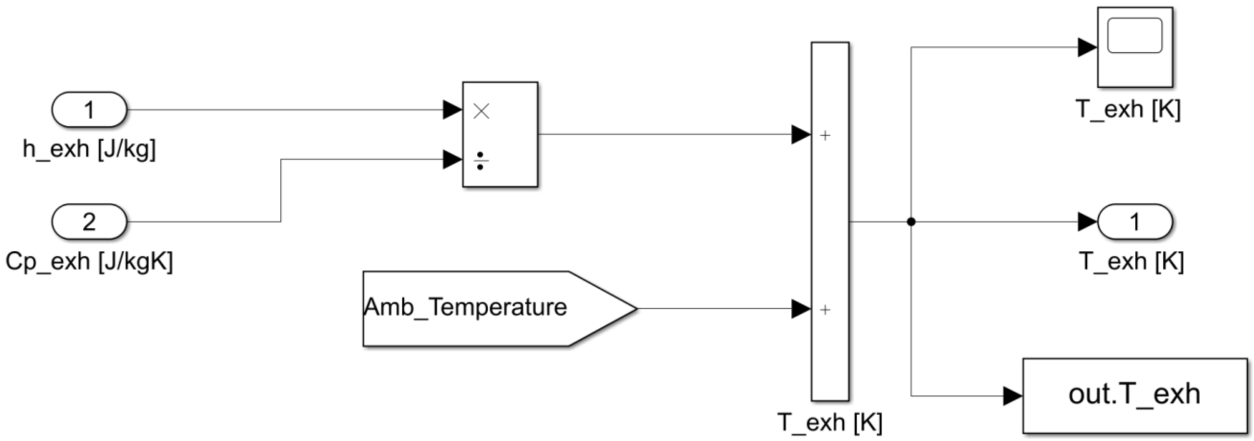

Figure 3.1.1.6.4 *Exhaust temperature model*

Usually, the turbine inlet exhaust pressure is modeled based on isentropic expansion and heat transfer across a turbocharger turbine [28]. Therefore, in this model, we assumed the exhaust pressure to be the same as the turbine inlet pressure. In addition, ΔP across the compressor outlet, turbine inlet at 0.2 bar, and turbine inlet pressure is greater than the compressor outlet pressure. Accordingly, the equation calculating the exhaust pressure can be shown as

$$P_{exh} = P_{c,in} + 0.2\ bar, \tag{3.33}$$

Moreover, the implementation of the exhaust pressure equation in Simulink is shown below

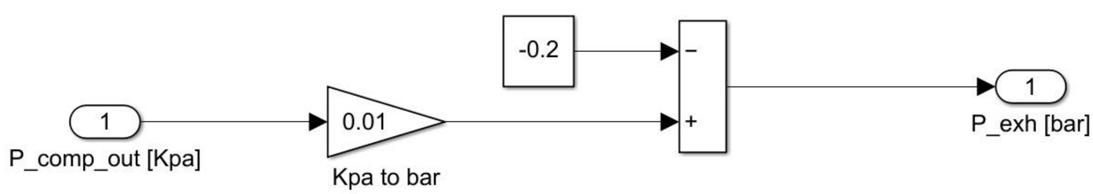

Figure 3.1.1.6.5 *Exhaust pressure model*

Compared to the composition of air, diesel exhaust gas contains increased concentrations of water vapor (H_2O) and CO_2, the main combustion products [29]. The specific heat of the exhaust gas can be calculated as a function of temperature by applying the ideal gas-specific heats of various common gases. In addition, the molar mass of each combustion species can be determined as a function of the AFR and the number of carbon, hydrogen, and oxygen atoms of the fuel. Finally, by calculating the mole fraction of each species, the specific heat of the exhaust at constant volume and temperature can be determined; hence, the specific heat ratio can be calculated. All calculations are performed in the exhaust-specific heat block, which is a MATLAB function block. The implementation of the exhaust gas-specific heat and specific heat ratio calculation in Simulink are shown below

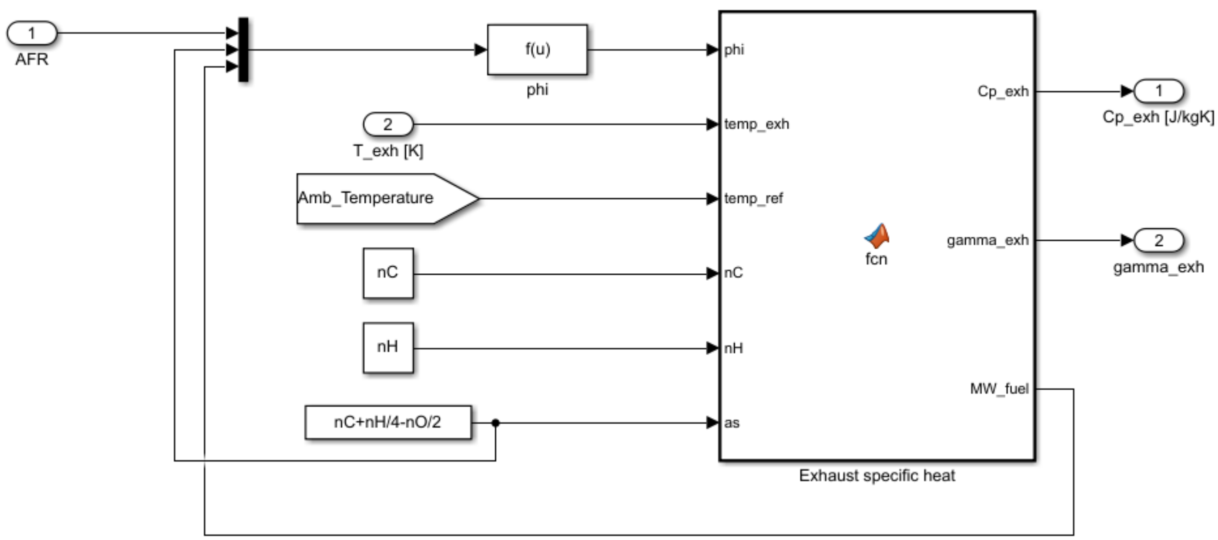

Figure 3.1.1.6.6 *Exhaust gas-specific heat and specific heat ratio model in Simulink*

3.1.2. Battery Model

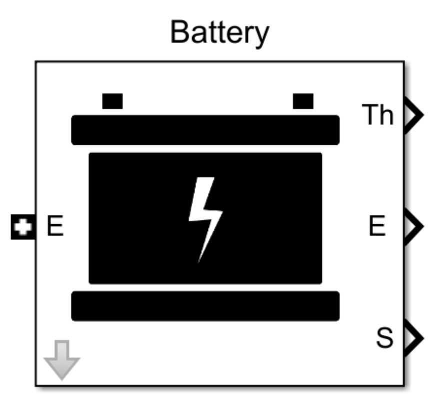

Figure 3.1.2.1 *Battery model in Simulink*

The battery model is based on work done by Sapra [22] and an adaptation of the modeling approaches presented in Mousavi and Nikdel [30] and Tremblay et al. [31]. Battery operation modeling can be mainly divided into two main categories (i.e., electrochemical and electrical circuit models) based on the modeling objective, details, and accuracy. Electrochemical models are complex and detailed but accurate, as they capture the detailed thermo-electrochemical processes during battery operation. These models are not used for system-level and dynamic studies [32].

Electrical circuit models are relatively simpler and simulate individual battery elements such as internal resistance, battery capacity, and voltage, which can be modeled as functions of state-of-charge (SOC), open-circuit voltage, temperature, etc. Because of their simplicity, low computation demands, and ability to capture relevant information, these models are especially useful for system-level battery performance modeling in automotive, land-based, marine, and aerial power generation. EC models can be combined with thermal models to simulate battery heat generation and temperatures because operating temperature affects many performance parameters, such as energy efficiency, capacity, reliability, lifetime, and life cycle cost [33]. Furthermore, battery thermal management is a crucial aspect of safe performance monitoring in power generation due to the high charge and discharge rates of batteries used in applications such as automotive and marine. Therefore, this article focuses on a generic electrical circuit and thermal battery model for system-level modeling.

The generic electrical circuit and thermal battery model operates under the following assumptions and boundary conditions:

- Battery capacity is independent of the current.

- The internal resistance is assumed to be constant during cycles and is independent of current amplitude.
- The effects of temperature and battery aging on the battery output are not considered
- Self-discharge is not considered.
- The temperature of the solid is spatially uniform.
- Heat generation from the enthalpy of mixing is neglected.
- The heat flow absorbed by conduction is the same as convection.

3.1.2.1. General Electrical Circuit Model

A generic battery model can be used to model various types of batteries. The model is ideal for studying dynamic simulations of different powertrains. The cell model calculates the cell terminal voltage (V) during the discharging and charging cycle by employing the following equations based on the Sheperd equation [30]

$$V_{dis} \ = \ E_0 \ - K_{dr} \ \frac{1}{SOC} i^* - R_0 \, i - \ K_{dv} \, Q \left(\frac{1}{SOC} - 1\right) + Ae^{-Bit}, \qquad (3.34)$$

$$V_{dis} \ = \ E_0 \ - K_{cr} \ \frac{Q}{\lambda Q + it} i^* - R_0 \, i - \ K_{cv} \, Q \left(\frac{1}{SOC} - 1\right) + Ae^{-Bit}, \qquad (3.35)$$

where E_0 is the open-circuit voltage, Q is the battery capacity; R_0 is the internal resistance; and i is the battery current. K_{dr} and K_{cr} are the polarization resistance coefficients for the discharge and charge cycles, respectively. The second term in the equations represents the polarization ohmic voltage drops, which are different for the charge and discharge cycles. λ simulates the shift in the polarization resistance during the charge cycle, and i^* is the filtered battery current that captures the dynamic response of the slow voltage during the step change in current [30]. The third term simulates the impact of internal resistance during the cycles. Term four of Equations 3-34 and 3-

35 estimates the polarization overvoltage, where K_{dv} and K_{cv} are the polarization over-voltage coefficient for the corresponding cycles. Finally, the last term replicates the exponential dynamic voltage shown below. Coefficients A and B account for the voltage drop during the exponential zone and the charge at the end of the exponential zone. Equations 3-34 and 3-35 show that a decrease in SOC reduces the voltage as the polarization overvoltage term becomes influential, while its impact is negligible near full capacity.

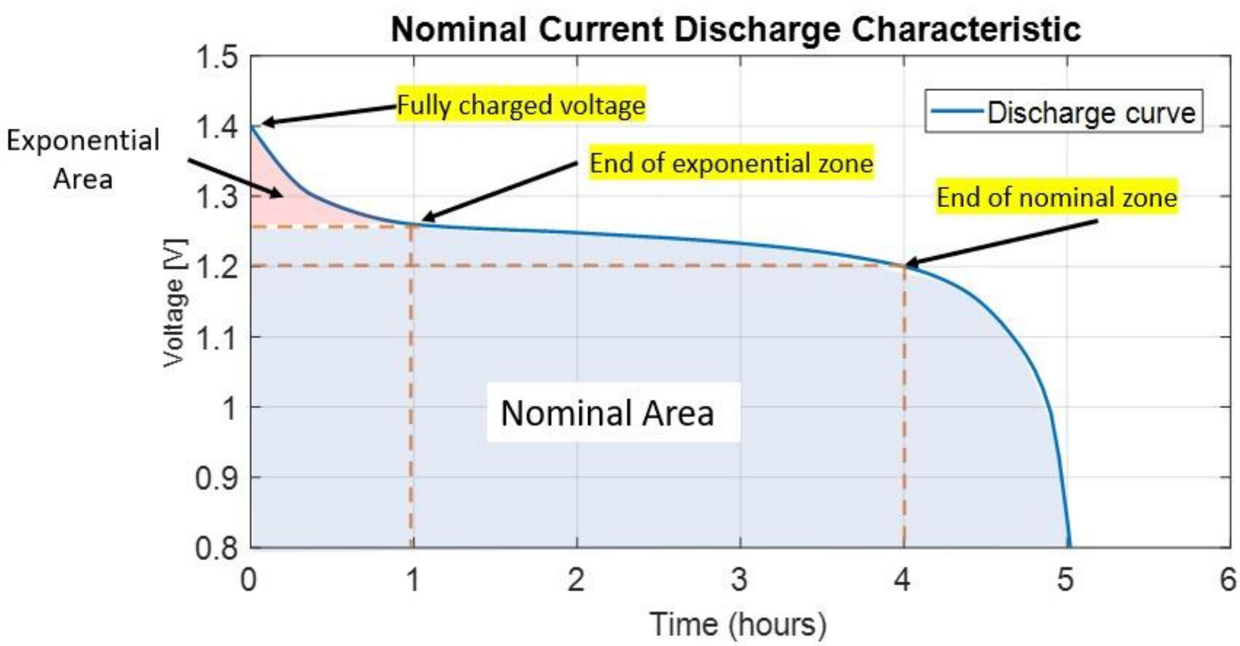

Figure 3.1.2.1.1 *Typical battery discharge curve [31]*

The parameters and coefficients required for the model can be obtained from the manufacturer data. A parameter extraction framework can be developed to calculate the values based on a typical discharge curve provided by the manufacturer, as presented in [31]. The various electrical and thermal battery parameters used in the current model for the lithium-ion battery were obtained from the literature [31]

3.1.3. Motor Model

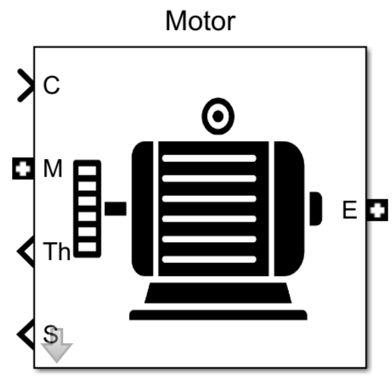

Figure 3.1.3.1 *Electric motor model in Simulink*

The motor component model which is based on work done by Sapra and Saemi [22]. The motor component model simulates an electric motor that accounts for the electric performance, motor efficiency, heat generation, and sizing. The figure below shows the outlook of the motor component block. This block has one control (C) input that provides the motor reference speed which comes from a connected shaft model discussed in section 3.1.5. The motor component model also requires a mechanical (M) and electrical (E) two-way connection to function. Additionally, a sensor (S) and a thermal (Th) output port are provided.

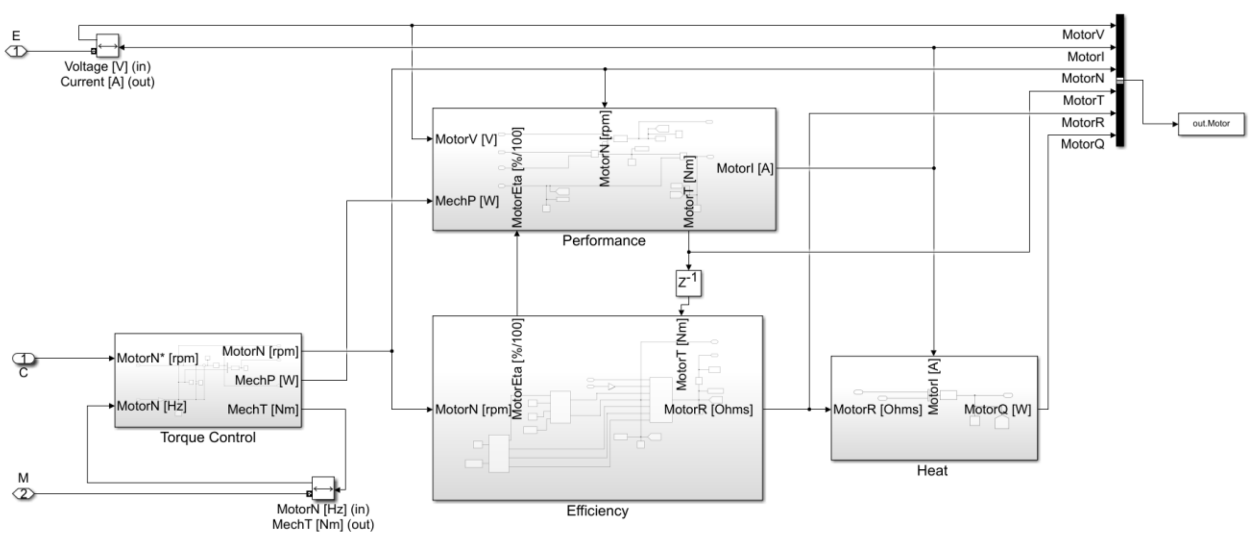

Figure 3.1.3.2 *Overview of the internals of the motor model in Simulink*

The figure above presents the inner workings of the motor model, which is divided into four sub-systems. The ‘Torque Control’ sub-system estimates the instantaneous mechanical torque based on the motor speed and its reference value. In combination with the ‘Speed Setpoint Controller’ block, the motor employs a cascade form of control by generating a motor speed reference based on the vehicle/aircraft speed and then using this motor speed reference for the torque controller in the motor model. Motor speed and mechanical torque are used to estimate the mechanical power input of the motor. Next, the ‘Performance’ sub-system calculates the electrical power (P_{mot}) and torque (T_{mot}) of the motor. Motor current (I) is estimated by dividing the electrical power with motor voltage (V), which is input from the DC Bus component (section 3.1.6) via the two-way electrical connection (E).

$$P_{mot} = \frac{P_{mech}}{\eta_{mot}}, \tag{3.36}$$

$$T_{mot} = \frac{60 \times P_{mot}}{2\pi \times N}. \tag{3.37}$$

The motor efficiency (η_{mot}) is calculated in the ‘Efficiency’ sub-system. Efficiency is calculated by employing a MATLAB function called ‘sim_motor2_2023_v2’. This MATLAB function is used in combination with the ‘size_machine’ and ‘wind_machine’ functions to calculate the motor efficiency, resistance, mass, and volume. The above functions were developed by Saemi [22]. Lastly, the sub-system ‘Heat’ estimated the motor heat generation based on the I^2R losses, where resistance (R) is obtained from the above described MALAB functions.

3.1.4. Generator Model

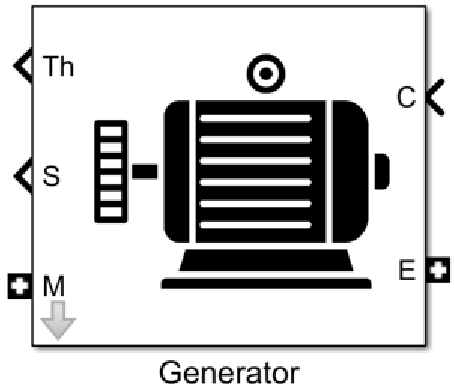

Figure 3.1.4.1 *Generator model in Simulink*

The generator model simulates an electric generator that accounts for the electric performance, generator efficiency, heat generation, and sizing. The working of the model is based on work done by Sapra and Saemi [22]. The figure above shows the outlook of the generator component block. This block has one control (C) input that provides the generator reference current for the model. In the series-hybrid truck architecture discussed in section 3.2, this reference current input is generated by using the 'Rule-based Controller' block which is covered in section 3.1.7. The generator component model also requires a mechanical (M) and electrical (E) two-way connection to function. Additionally, a sensor (S) and a thermal (Th) output port are provided.

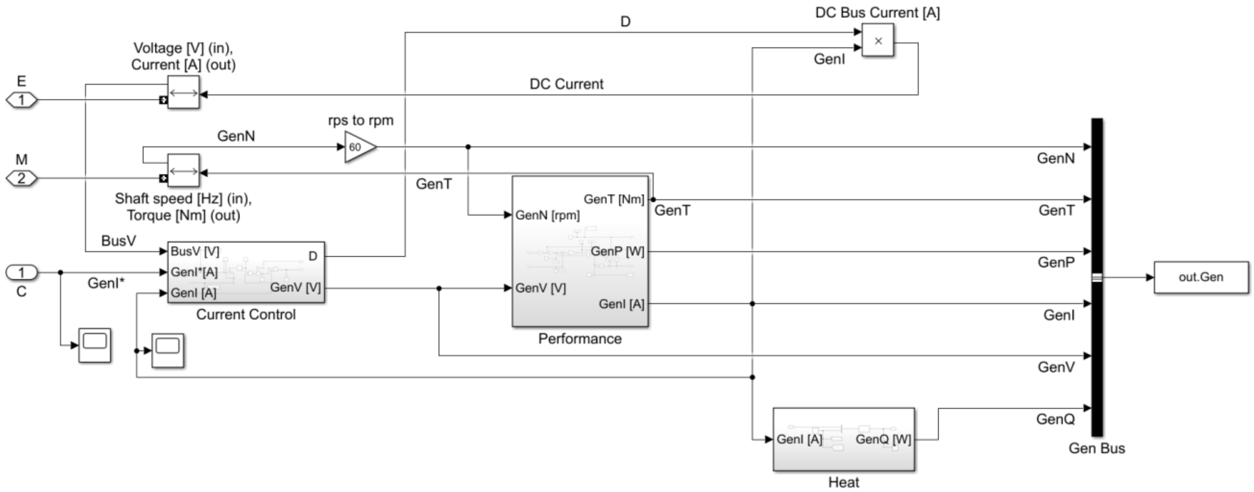

Figure 3.1.4.2 *Overview of the internals of the generator model in Simulink*

The figure above presents the inner workings of the generator model, which is divided into three sub-systems. The ‘Current Control’ sub-system employs a PI current controller to generate a reference voltage for the duty-cycle (D) based on the generator current and its reference value. The duty cycle is multiplied by the DC bus voltage to estimate the generator voltage. This voltage is then communicated to the ‘Performance’ subsystem to estimate the back-emf ($V_{gen,bemf}$). The ‘Performance’ sub-system calculates the difference between the $V_{gen,bemf,}$ and the generator voltage (V_{gen}) to estimate the generator current (I_{gen}). The generator current, through the duty-cycle, is then exchanged via the electrical two-way connection (E) as an output, while the DC Bus voltage is communicated as an input.

$$V_{gen,bemf} \; = \; N_{gen} \times k_{t,gen}, \tag{3.38}$$

$$I_{gen} = \frac{V_{gen,bemf} - V_{gen}}{R_{gen}}. \tag{3.39}$$

The torque constant ($k_{t,gen}$) and resistance (R_{gen}) are estimated by employing a MATLAB function called ‘gen_wind_machine’. This MATLAB function is used in combination with the ‘sim_gen’ and ‘gen_size_machine’ functions. Similar to the electric motor models, these functions were developed by Saemi [22] to calculate the efficiency, resistance, mass, and volume of the electrical machine.

After calculating the generator current, the mechanical generator power is estimated as a product of the generator back-emf voltage and generator current. This mechanical power and speed are further used to calculate the mechanical generator torque, which is an output exchanged via the mechanical two-way connection (M). Next, the electrical power of the generator is modeled by multiplying the previously calculated mechanical power with generator efficiency. Lastly, the sub-system 'Heat' estimates the motor heat generation based on the ${I_{gen}}^2R_{gen}$ losses, where generator resistance is obtained from the above described MALAB functions.

3.1.5. Shaft Model

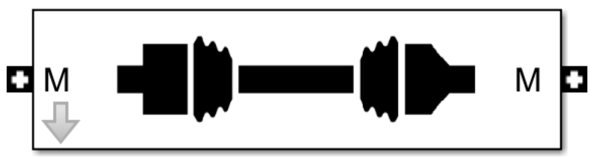

Figure 3.1.5.1 *Mechanical shaft model in Simulink*

A shaft model is useful in establishing a mechanical connection between the load and drive components or controller systems. The shaft component is connected between the engine and generator in the SHE powertrain, between the drive cycle input block and the engine in the ICE powertrain and between the motor controller and electric motors in the BE powertrain model. As seen in **Error! Reference source not found.**, the shaft component uses two mechanical two-way connection ports to connect with the drive and load side. These two connection ports transmit torque (T) and shaft speed.

$$n = \int \frac{T_{Drive} - T_{Load}}{2\pi I}. \tag{3.40}$$

The shaft model accounts for the angular momentum balance. To estimate the shaft speed (n), this component model requires the sum of the inertia (I) of all the components connected to the shaft as user input. This inertia value can be used as a calibration parameter to tune the dynamic response of the connected system. Secondly, this shaft model also requires an initial shaft speed value in [Hz or rps] as an initial condition for the integrator.

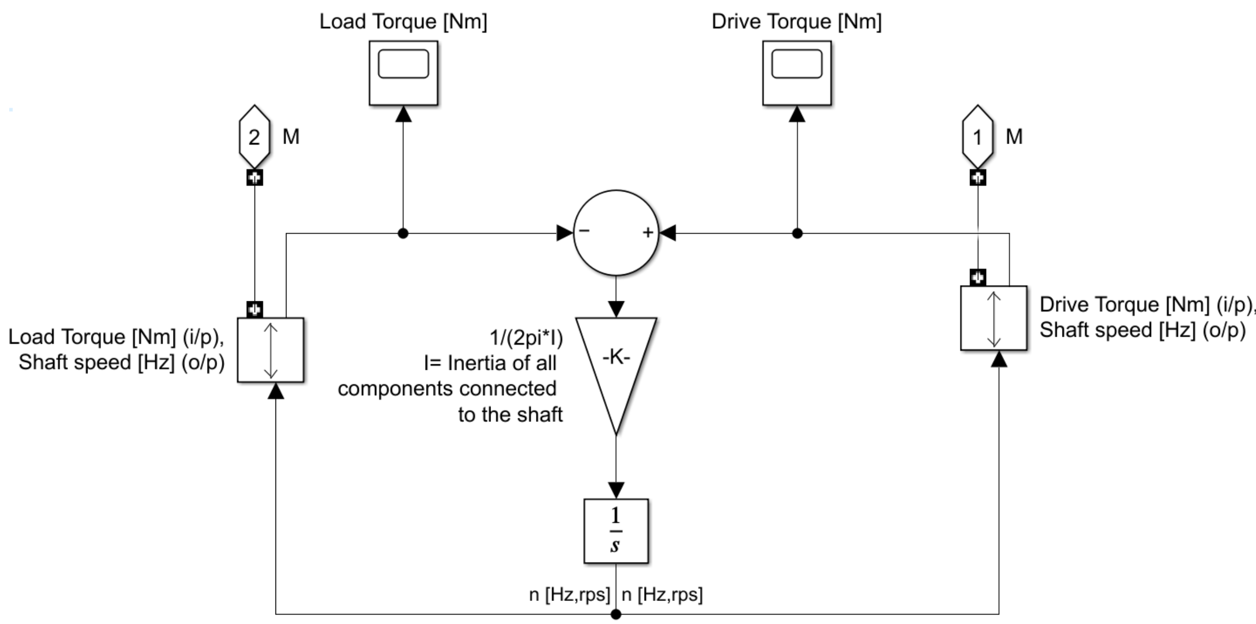

Figure 3.1.5.2 *Overview of the internals of the shaft model*

3.1.6. DC Bus Model

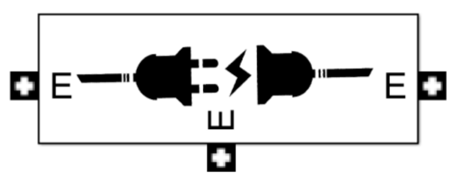

Figure 3.1.6.1 *DC Bus model in Simulink*

The DC bus component model acts as the communication and transfer link between the electrical components. For instance, in the SHE truck model, the DC bus communicates electrical signals between the motor, battery, and generator models. This three-way electrical distribution bus is depicted in Figure 3.1.6.24. The device routes appropriate current and voltage between these connected components. This component model also employs two-way connection ports. Two-way connection ports allow for bi-directional information flow while simplifying the interfaces between the component models. For each two-way connection port, the following naming scheme is applied. The first/top parameter represents the value coming into the port/component model and the second value represents the value going out. For example, in the figure below 'E' two-way connection port on the left represents the current demand from the motor coming into the DC bus and the voltage from the bus going out of the port.

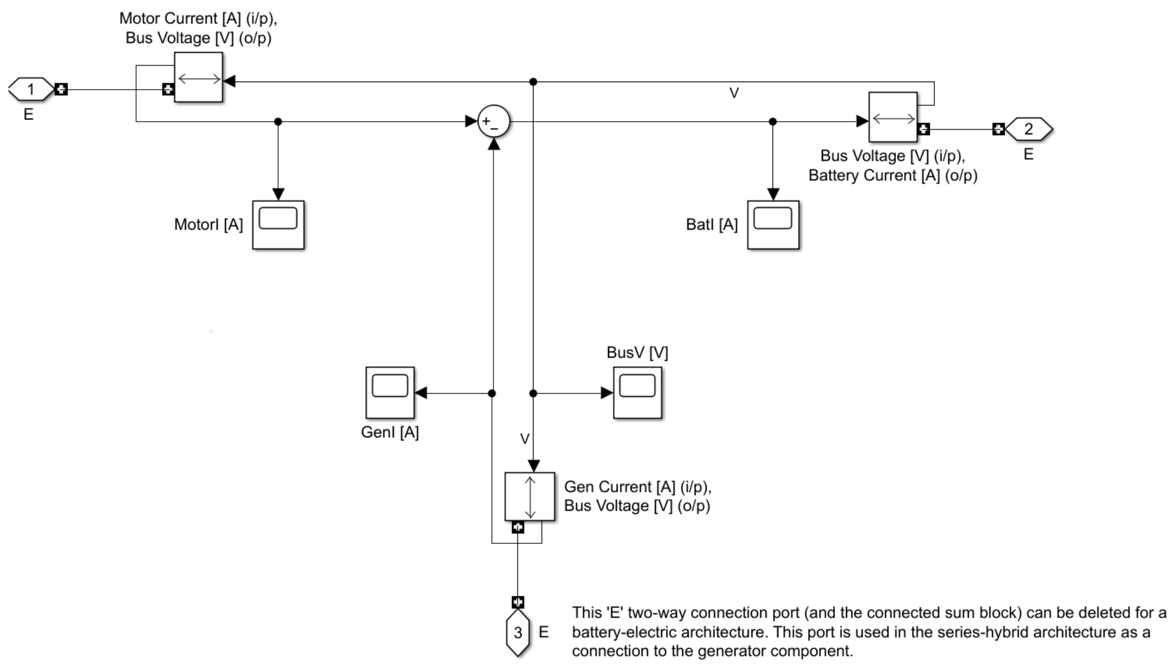

Figure 3.1.6.2 *Overview of the DC bus model internals*

The DC Bus component model can be easily modified to include fewer or more electrical connections. For instance, in the case of a battery-electric architecture, the middle 'E' two-way connection communicating with the generator can be simply deleted as there is no generator in a pure battery-electric power plant. In this case, the subtraction (or sum) block can also be deleted to allow a direct connection between the battery and the motor.

3.1.7. Rule-Based (RLB) Controller Model

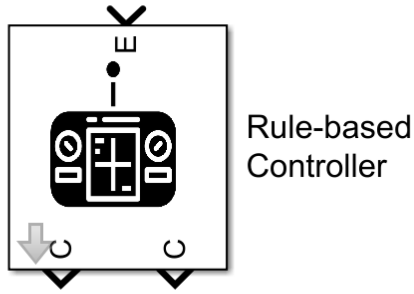

Figure 3.1.7.1 *Rule-Based (RLB) controller model in Simulink*

The rule-based controller component model is a simple algorithm that provides the supervisory control logic to decide the operation modes or the instants when the battery discharges while delivering the load and when the engine-generator unit supplies the required propulsion load and charges the battery. The working of the controller is based on the work of Gao et al. [34]. The rule-based controller is employed in the SHE truck to dictate the reference engine rpm and generator current setpoints based on the battery SOC value.

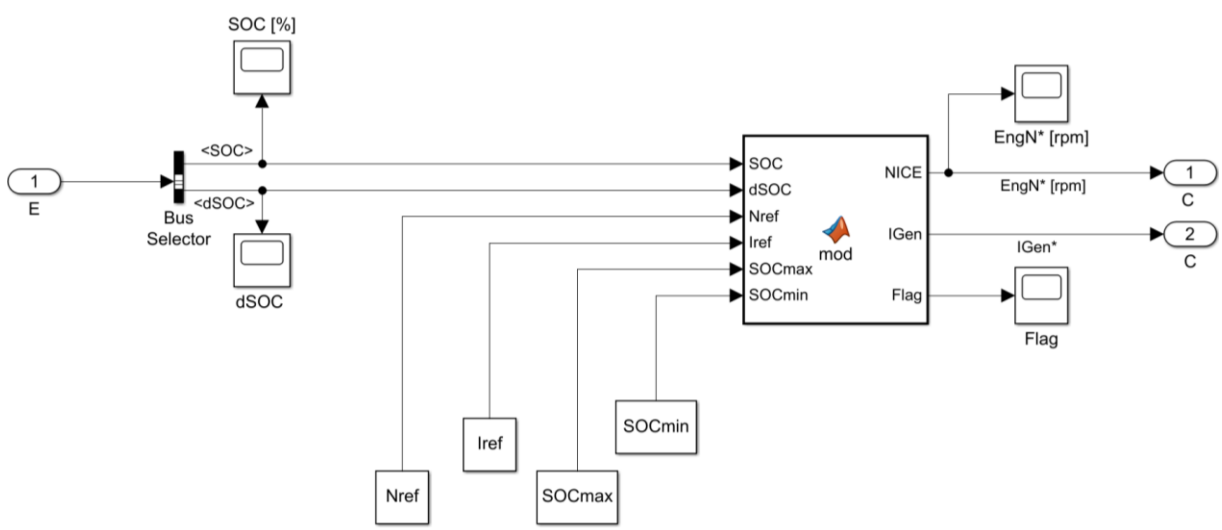

Figure 3.1.7.2 *Overview of the rule-based controller model internals*

The rule-based algorithm is set up as a MATLAB function and uses battery SOC and the filtered derivative of SOC (SOC’) as inputs. The battery supplies the load demand when the SOC is greater than a user-prescribed max SOC or between the user-defined min SOC and max SOC while the SOC’ is negative or zero. In other conditions, the engine-generator charges the batteries based on the user-defined engine rpm setting. In this manner, the battery SOC is maintained between the defined SOC limits after the simulation is initiated at any initial SOC value. It is important to note that these minimum and maximum SOC values along with the engine rpm and generator current setpoints can be varied as user-inputs from the ‘RLBControl’ component input file or the controller mask. The component input file is shown below.

```
function [NICE,IGen,Flag]= mod(SOC,dSOC,Nref,Iref,SOCmax,SOCmin)
 if SOC>=SOCmax && dSOC>=0;
    NICE = 0;
    Flag = 0;
    IGen = 0;
 elseif SOC>=SOCmax && dSOC<0;
    NICE = 0;
    Flag = 1;
    IGen = 0;
 elseif SOC<SOCmax&SOC>=50 && dSOC>0;
        NICE = Nref;
        Flag = 2;
        IGen = Iref;
 elseif SOC<50&SOC>=SOCmin && dSOC>0
        NICE = Nref;
        Flag = 3;
        IGen = Iref;
 elseif SOC<SOCmax&SOC>=SOCmin && dSOC<=0;
     NICE = 0;
     Flag = 4;
     IGen = 0;
 elseif SOC < SOCmin
     NICE = Nref;
     Flag = 5;
     IGen = Iref;
 else
     NICE = 0;
     Flag = 6;
     IGen = 0;
 end
```

Figure 3.1.7.3 *Inside the rule-based controller MATLAB function block*

3.1.8. Motor Controller Model

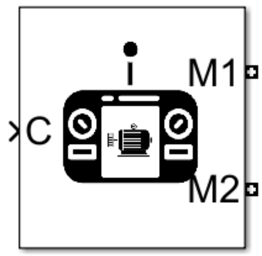

Figure 3.1.8.1 *Motor controller model in Simulink*

The motor controller model is a simple algorithm that provides the supervisory control logic to decide which electric motor to use to provide the propulsion load in a two-motor powertrain. The working of the controller is based on the work of [35]. This controller is employed in the BE truck powertrain model to dictate which of the two motors to use based on the input load torque transmitted via the control port (C) on the left. The first mechanical port (M1) is to be connected to the larger motor and the second port (M2) is to be connected to the smaller of the two electric motors via shaft models. The user must provide the maximum torques of the two connected electric motors for the model to function. **Error! Reference source not found.**9 below shows the internal workings of the model in Simulink. The if statement block decides which of the three controller modes to select based on the input load torque. If the load torque is less than the maximum torque of the smaller motor, then the controller has the smaller motor provide all the load torque (Low Load Mode). If the load torque is greater than the smaller motor's maximum torque but less than the larger motor's maximum torque, then the controller has the larger motor provide all the load torque (High Load Mode). Finally, in "Assist Mode", both electric motors work together. The larger motor provides most of the load torque with the smaller motor assisting. This mode is utilized when the input load torque is greater than the maximum torque of the larger motor. Once the torque reference value is calculated by one of the mode subsystems blocks, the merge block in Simulink merges the reference torque signals and sends the output to the connected shaft models via two-way connection blocks.

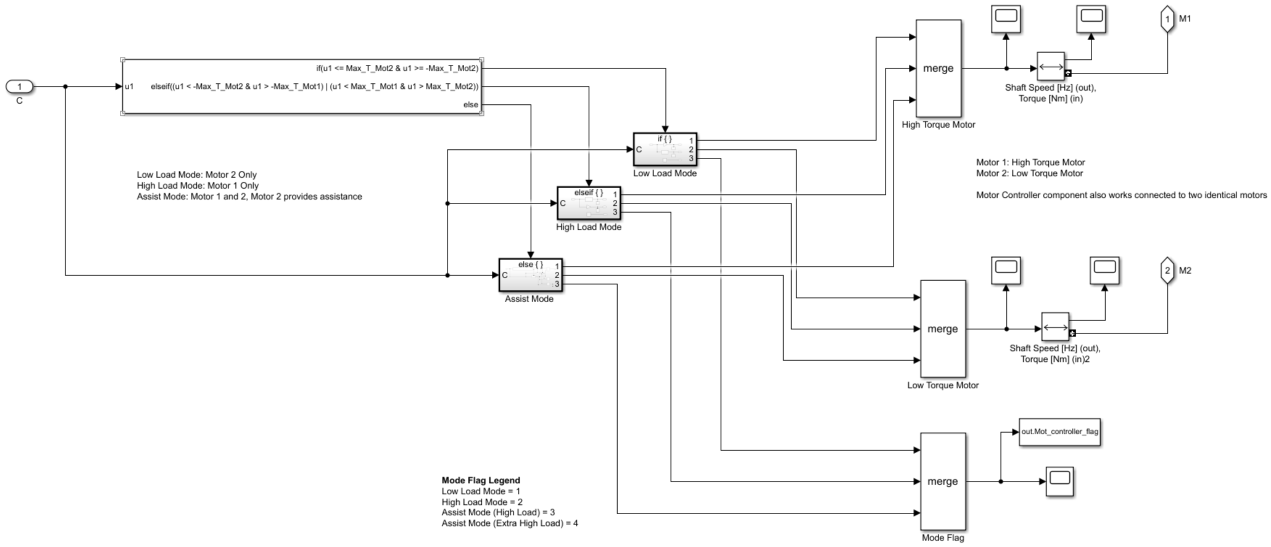

Figure 3.1.8.2 *Overview of the motor controller internals*

3.2. Powertrain Simulation Models

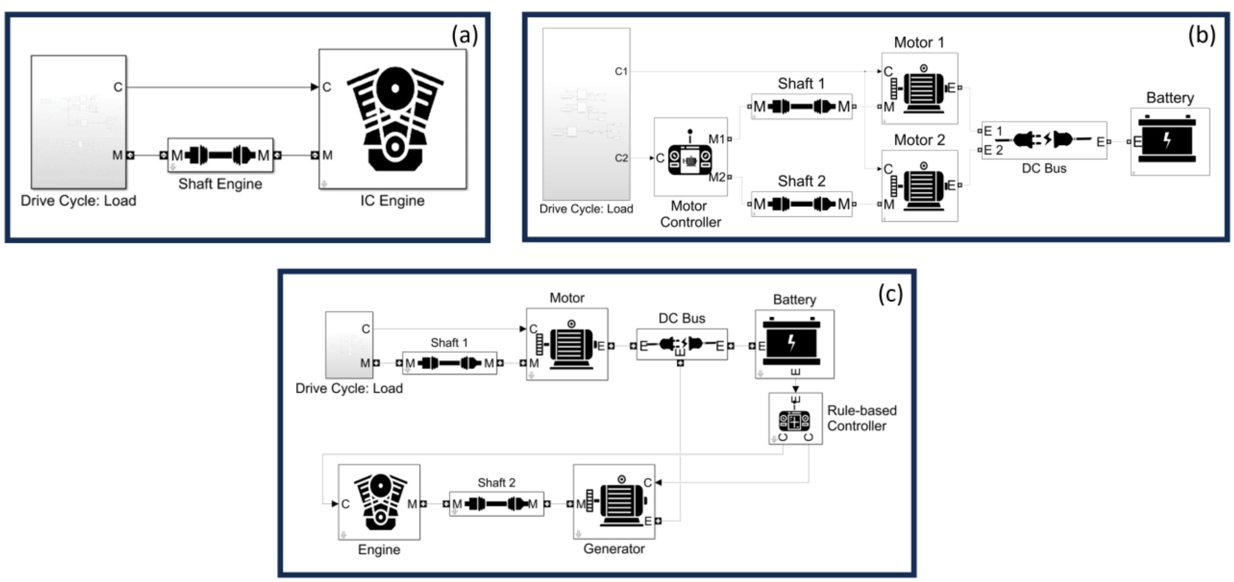

Figure 3.2.1 *Truck simulation models in Simulink (a) Diesel (ICE) (b) Battery-Electric (BE) and (c) Series-Hybrid Electric (SHE)*

Error! Reference source not found. displays the high-level view of the ICE, BE, and SHE truck models. The three components of the ICE truck model were the drive cycle, shaft, and IC engine model. The drive cycle model encompassed the engine load torque and speed from NREL's drive cycle data [36]. The shaft model calculates shaft speed by accounting for the inertia effect. Finally, the ICE model is a 0-D mean value and energy balance model that calculates instantaneous engine performance and fuel consumption. Note that the drive cycle and shaft models are also used in the BE and SHE truck models and function similarly to the ones in the ICE truck model.

The six components of the BE truck model were the drive cycle, motor controller, two shafts, electric motor, DC bus connector, and battery model. The motor model is dynamic, that is it calculates current to the battery as a function of motor efficiency. The battery is an electrical circuit model based on the modified Shepherd equation [31]. It can simulate battery elements, such as internal resistance, battery capacity, and voltage, modeled as functions of state-of-charge (SOC) or open-circuit voltage. The DC bus model manages the current from the motor entering the battery model. The two shafts transmit torque and shaft speed to the two electric motors. The BE truck model was tested and validated against experimental data, the results of which can be found in section 8.2.

The eight components of the SHE truck model were the drive cycle, shaft, motor, DC Bus, battery model, Rule-Based Controller, generator, and IC engine model. The rule-based controller is responsible for controlling the activation of the engine to charge the battery by supplying the speed setpoint to the engine and the current setpoint to the generator. The generator charges the battery and works similarly to the motor model. The DC bus model manages the current from the motor and generator entering the battery model. Every component has user-defined parameters that were added via a mask in Simulink which are tabulated in section 0. Values required to calculate emissions, such as the fuel and battery energy used, were collected from these simulation models by providing the target drive cycle and user-defined parameters as inputs. The following section discusses the emissions calculation approach in detail.

3.3. Emissions calculation

This section will describe the analytical models used to estimate the vehicles' total CO_2 and NO_x emissions within the scope of this paper which has been illustrated in **Error! Reference source not found.**. Although BE trucks produce no tailpipe emissions during operation, most of the emissions are associated with upstream electricity generation [20]. Therefore, it is critical to estimate the total emissions using a 'Well-to-Wheel' (WTW) analysis [37] [38].

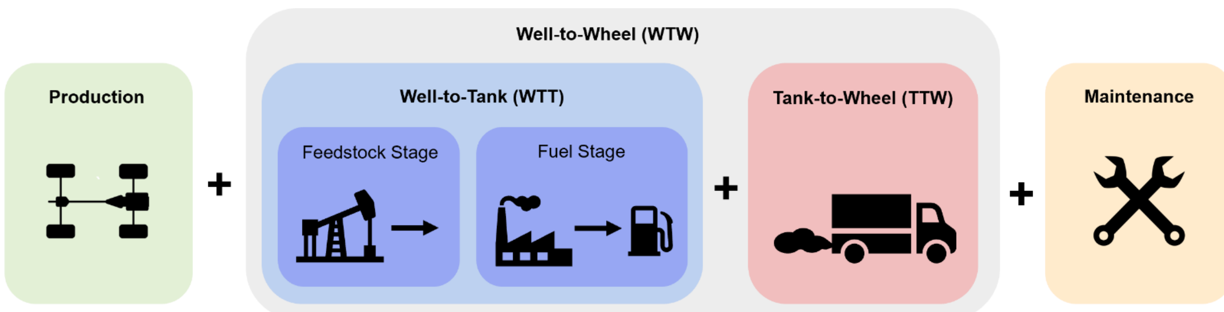

Figure 3.3.1 *Phases of the life-cycle analysis within the scope of this study*

3.3.1. Well-to-Wheel emissions

The WTW emissions are crucial for comparing the in-use emissions for all trucks because it captures the emissions of the entire energy flow; this includes the process of extracting fossil fuel or generating electricity to the emissions at the vehicle's tailpipe [39]. Well-to-Wheel emissions have two stages: Well-to-Tank (WTT) and Tank-to-Wheel (TTW). The WTT stage covers the production/extraction of the fuel from the primary source of energy (feedstock stage) to the vehicle's energy storage system (fuel stage). The energy storage system is the fuel tank for the ICE and SHE trucks and the battery for the BE and SHE trucks. The TTW stage covers the emissions associated with the vehicle's operation [38]. The emissions generated from WTW are illustrated in the equation below. E_{WTT} and E_{TTW} are the WTT and TTW emissions respectively in kg.

$$E_{WTW} = E_{WTT} + E_{TTW} \tag{3.41}$$

3.3.2. Well-to-Wheel for ICE and SHE truck

The feedstock stage for both ICE and SHE trucks includes the emissions from fuel extraction, transportation to the refinery, and storage. The fuel stage consists of the emissions associated with the fuel refining and distribution to the gas station [40]. The TTW emissions encompass the emissions from fuel combustion during the truck operation. 3.4 The total WTW emissions associated with the ICE and SHE trucks $\boldsymbol{E_{WTT,Diesel}}$ are estimated by:

$$E_{WTT,Diesel} = \left(I_{Feedstock,Diesel} + I_{Fuel,Diesel}\right) \times U_{Diesel} \tag{3.41}$$

$$E_{TTW,Diesel} = I_{TTW,Diesel} \times U_{Diesel} \tag{3.42}$$

$$E_{TTW,Diesel,NO_x} = \int_{t_{start}}^{t_{end}} \dot{I}_{TTW,Diesel,NO_x} \times P_{Engine} \times dt \tag{3.44}$$

$$E_{WTW,Diesel} = E_{WTT,Diesel} + E_{TTW,Diesel}, \tag{3.45}$$

$I_{Feedstock,Diesel}$ and $I_{Fuel,Diesel}$ are the WTT emissions intensities for diesel fuel's feedstock and fuel stage. $I_{TTW,Diesel,CO_2}$ is TTW or tailpipe CO_2 emissions intensity. $\dot{I}_{TTW,Diesel,NO_x}$ is the NO_x emissions rate in g/kWh. Furthermore, U_{Diesel} is the volume of diesel used and P_{Engine} is the engine power that comes from the MATLAB/Simulink models.

3.3.3. Well-to-Wheel for BE truck

In this study, the WTW phase for the BE truck is divided into the feedstock, generation, and transmission stages. The TTW emissions were neglected for this analysis because BE trucks are assumed to emit no tailpipe emissions in this study. The WTW phase for BE trucks has been illustrated in **Error! Reference source not found.**.

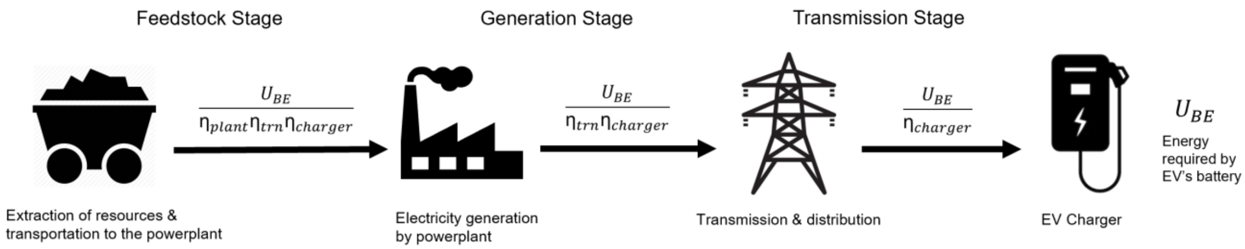

Figure 3.3.3.1 *Well-to-wheel (WTW) stages for BE Truck.*

The feedstock stage in the BE trucks includes the production of fuel that spans from the extraction of the primary source of energy to the corresponding power station [40]. The generation stage included the emissions from the power plant's electricity generation. According to GREET 2023, the transmission stage included electricity transmission and distribution through the transmission line [7]. Transmission and charging losses from the power grid and charging station were also accounted for in the emissions calculation of the BE truck. The total WTW emissions associated with the BE truck $E_{WTW,BE}$ is calculated by

$$E_{WTT,BE} = I_{BE} \times \frac{U_{BE}}{\eta_{charger}}, \tag{3.46}$$

$$I_{BE} = \sum \left(\frac{I_{Feedstock}}{\eta_{plant}\eta_{trn}} + \frac{I_{Generation}}{\eta_{Transmission}} + I_{trn} \right) \times f_{source}, \tag{3.47}$$

$$E_{TTW,BE} = 0, \tag{3.48}$$

$$E_{WTW,BE} = E_{WTT,BE.} \tag{3.49}$$

where I_{BE} is the WTT emissions intensity for the BE truck in g/kWh. I_{BE} combines the emissions intensity and efficiency from the feedstock, generation, and transmission stages of various power plants, this breakdown has been illustrated in **Error! Reference source not found.**. The $\eta_{Plant}, \eta_{trn},$ and $\eta_{charger}$ are the powerplant, transmission, and charging station efficiencies respectively. Furthermore,U_{BE} is the total battery energy required to charge the battery. The amount of energy that needs to be recharged is obtained from the BE truck Simulink model.

The emissions intensity varied with the electric grid generation source and its corresponding mixture; the CO_2 and NO_x emissions intensity was calculated by finding the sum of all grid generation sources and multiplying it by each corresponding fraction f_{source}. The f_{source} term accounts for the amount each electricity source contributes to the grid. The f_{source} term remains constant for the US average grid assumption and varies every minute for the time-dependent assumption. Section 4.3.2 details what powerplants are part of this study's scope and section 4.3.3 explains how the time-dependent analysis calculated the f_{source} term.

4. Scope of study

This section discusses the scope of the LCA study: the long-haul and drayage drive cycle data used as input for the simulation models, specifications of the truck powertrains, the routes along which the trucks operate, diesel fuel production, tailpipe emissions, electricity generation, and grid assumptions and scenarios.

4.1. Drive Cycles

The first drive cycle chosen was the Fleet DNA Long-Haul Daily Trip Representative. The drive cycle was created by NREL and represents a comprehensive driving cycle for a long-haul truck [41]. The drive cycle lasted for 19.7 hours, with a total distance of 983.5 miles, an average speed of 48 mph, and 47 stops. The maximum torque required for this drive cycle is 2413 N-m. Figure 4.1.1 NREL's Fleet DNA long-haul representative drive cycle a) torque b) speed data [23].

shows the torque and speed of the drive cycle.

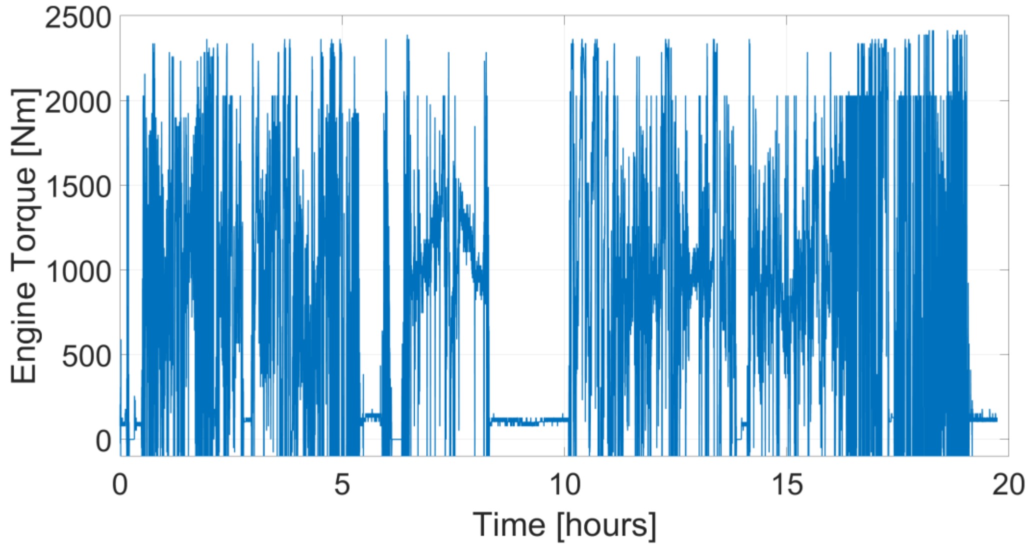

(a)

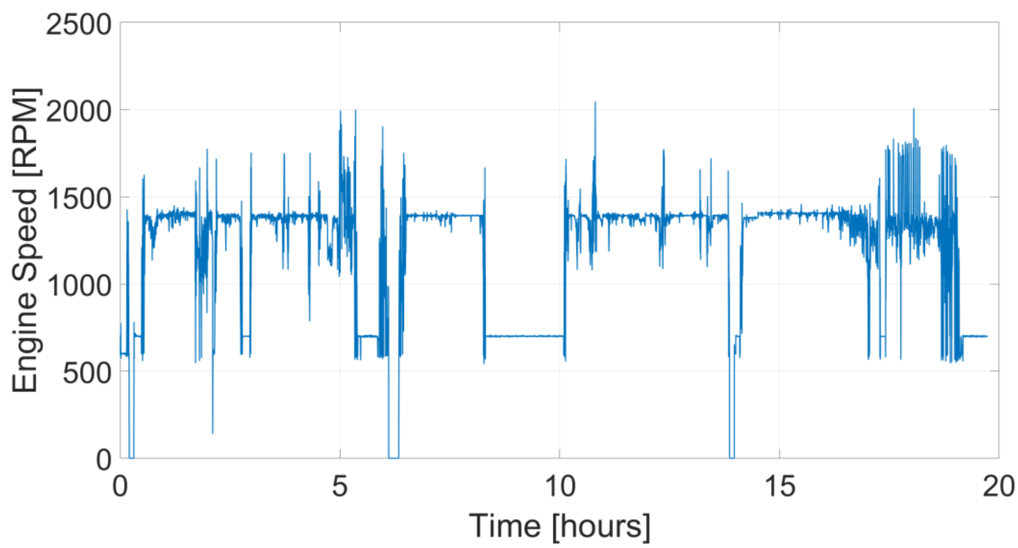

(b)

Figure 4.1.1 *NREL's Fleet DNA long-haul representative drive cycle a) torque b) speed data [23].*

The second drive cycle chosen was the Fleet DNA Drayage Representative. This drive cycle was also created by NREL [42]. This drive cycle was chosen to be in contrast to the long-haul drive cycle as it has 176 stops and a lower average speed of 17 mph indicating a more "stop and go" driving [36]. Additionally, this drive cycle was included because California now requires all new drayage trucks to be zero-emissions vehicles starting in 2024 [43]. The drive cycle lasted 8.6 hours, with a total travel distance of 96.9 miles. The maximum torque and power required for this drive cycle are 2283 N-m and 319 kW, respectively. Figure 4.1.2 NREL's Fleet DNA drayage representative drive cycle (a) torque (b) speed data [23].

shows the torque and speed from the drive cycle.

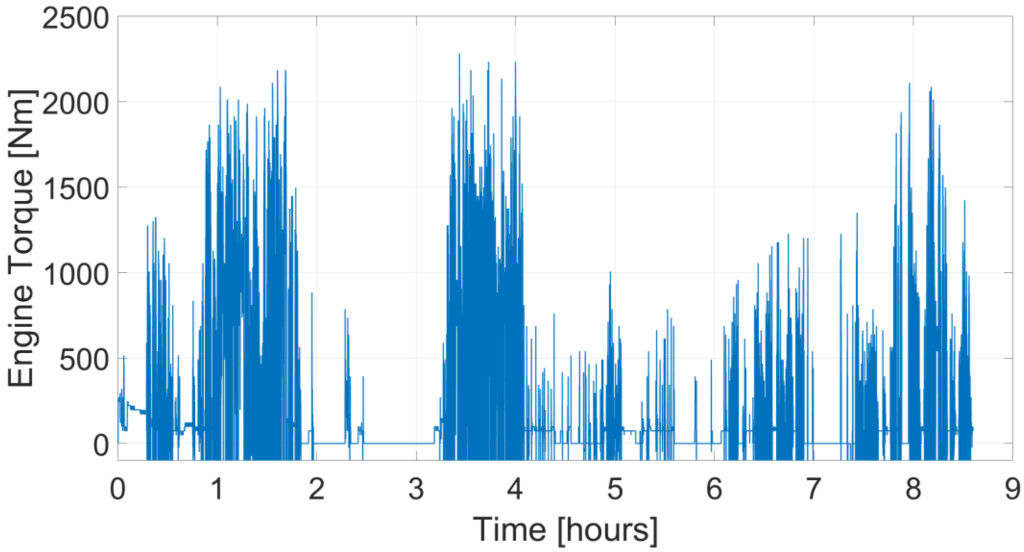

(a)

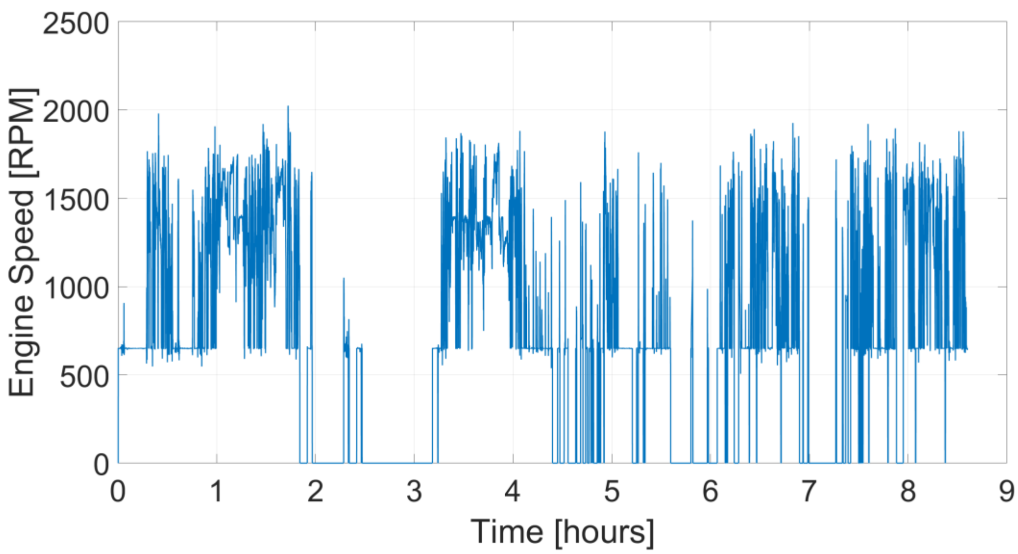

(b)

Figure 4.1.2 *NREL's Fleet DNA drayage representative drive cycle (a) torque (b) speed data [23].*

4.2. Vehicle Specifications

This section covers the specifications of the powertrain components of the three trucks. Key specifications have been summarized in **Error! Reference source not found.**, the input parameters for the Simulink models have been tabulated in section 0.

Table 4.2.1 *Summary of key vehicle specifications*

	Diesel Truck (ICE)	**Battery-Electric Truck (BE)**	**Series-Hybrid Electric Truck (SHE)**
Engine Displacement	14.9 L	-	10 L
Engine Power / Torque	565 hp / 2,779 N-m	-	402 hp / 1,900 N-m
Motor Power / Torque	-	548 kW / 3000 N-m 235 kW / 1300 N-m	400 kW / 2,500 N-m
Generator Power / Torque	-	-	300 kW / 1900 N-m
Battery Capacity	-	900 kWh	200 kWh

4.2.1. ICE truck

The specification of the ICE truck in this analysis is based on the Cummins X15 engine [44]. As mentioned in section 3.3.2, the total WTW emissions are directly proportional to the fuel used. For several reasons, the fuel used in an internal combustion engine can vary. However, the fuel's lower heating value and gross indicated thermal efficiency serve as the primary factors that affect the fuel mass [25]. The mass of fuel m_{fuel} required was calculated using

$$m_{fuel} = \frac{W_g}{\eta_{gross} \times LHV}, \tag{4.1}$$

where W_g is the gross work of the engine, LHV is the fuel's lower heating value, and η_{gross} is the gross indicated efficiency (GIE) of the engine. The lower heating value (LHV) varies based on the type of fuel used for the engine. GIE varies based on the engine's efficiency. Currently, 97% of US class 8 trucks are powered by diesel [45]. Therefore, low-sulfur diesel fuel with LHV of 42.6 MJ/kg was used for the analysis [7]. The GIE was varied from 46.7-47.8% as part of the uncertainty analysis [46]. The truck was set to have a fuel tank capacity of 120 gallons (454 Liters) [47].

4.2.2. BE Truck

The specifications of the BE truck are based on the Tesla Semi. Section 8.2goes into more detail about how the model was validated and how the specifications of the motor and battery were estimated. The Tesla Semi has three motors. The two motors for the front axle are referred to as the "Accelerator Unit" and one motor for the rear axle is referred to as the "Highway Unit" [48]. The twin "Accelerator Unit" motors have been assumed to be a single motor in the simulation as no lateral movement of the vehicle is being considered. The regenerative braking efficiency is set to vary from 58-64% as part of the uncertainty analysis [49] [50] .The Tesla Semi is estimated to have a battery pack capacity of 900 kWh with a 1000 V powertrain [48]. The battery pack consists of Tesla's own 21700 lithium-ion cells [51]. The manufacturer's specification sheet for this cell was not available and therefore the specifications of a similar lithium-ion cell, the Samsung 40T were used [52]. The 1000 V powertrain with a maximum cell voltage of 4.2V limits the number of cells in series of the battery to 238. Based on the total capacity required and the maximum output of the battery, the number of cells in parallel to 209. The minimum SOC is assumed to be 4% based on testing by Tesla [48].

4.2.3. SHE Truck

The engine model in the SHE truck uses the same fuel and GIE values as the ICE truck. According to Kim et al. [53], the engine and generator are sized to account for 90% of the drive cycle's requirements for a Series-Hybrid heavy-duty vehicle. This led to the engine being rated to produce 300 kW (402 hp). According to Kulikov et al. [54], a long-haul, heavy-duty diesel engine typically has the lowest brake-specific fuel consumption (BSFC) at 1,100 RPM to 1,300 RPM with 70% to 100% load. Therefore, the engine speed is held at a constant 1,200 RPM by the rule-based controller when charging the battery. Based on these specifications, the Cummins X10 was selected to be the basis for the engine model [55]. The truck was set to have the same fuel tank capacity as the ICE truck. The rated torque and power of the generator was set to 1900 N-m and 300 kW [53]. As mentioned by Dehesa [56], the engine typically provides torque to charge the battery around 1C, charging the battery rapidly while mitigating battery degradation. Therefore, the generator current is set at 650 A, ensuring the engine load falls into the most efficient zone, and the average charging C rate is around 1C. The traction motor is the only power source powering the wheels. Therefore, the rated power and torque of the motor were set to 400 kW (536 hp) and 2,500 N-m to be able to meet the demands of both drive cycles [36]. The regenerative braking efficiency is the same as the BE truck's. The induction motor's maximum voltage was set to 750V [53]. The battery pack capacity was set to 200 kWh. The pack consists of the same cells as the BE truck model. This limits the number of cells in the series of the battery to 179 and the number of cells in parallel to 62. The control scheme of the rule-base controller for the series hybrid was adapted from Gao et al. [34], which manages the charging operation by keeping the battery's SOC between 20% and 80%.

4.3. Electricity and diesel fuel use and production

This section covers the assumptions, data, and scenarios regarding diesel fuel use and production, BE truck charging, and electricity generation.

4.3.1. Diesel fuel use and production

Eqs. (3.41) to (3.4) demonstrated how the WTW CO_2 and NO_x emissions of the ICE and SHE trucks were influenced by fuel consumption and the WTT and TTW emissions intensity. The total amount of fuel was obtained from the ICE and SHE truck Simulink models. The parameters and emissions intensity values alongside their uncertainties have been summarized in **Error! Reference source not found.**. In this study, diesel feedstock and fuel stage emissions were assumed constant for all regions as no literature supporting regional variation was found.

Table 4.3.1.1 *CO_2 and NO_x emissions intensities for the WTW phase of diesel fuel*

Parameter		Minimum	Maximum	Average	Standard Deviation	Source
Feedstock	**CO_2 [g/L]**	150	380	265	38.3	Sun et al. [57]
	NO_x [mg/L]	16.8			0	GREET 2023 [7]
Fuel Stage	**CO_2 [g/L]**	181			0	GREET 2023 [7]
	NO_x [mg/L]	60	82.6	71.35	3.75	Sun et al. [57]
Tank-to-Wheel	**CO_2 [kg/L]**	2.683			0	GREET 2023 [7]
	NO_x [g/kWh]	0.22	0.34	0.28	0.02	Neely et al. [58] and Ma et al. [59]

4.3.2. Charging and electricity generation

The charging phase served as the main contributor to the WTW CO_2 and NO_x emissions for the BE truck. The BE truck in this study was charged at Electrify America's Hyperfast charger which is capable of charging at 350 kW and 437.5 A [60]. The charger's efficiency was varied from 85-95% as part of the uncertainty analysis [61]. This study considered coal, natural gas, petroleum, renewables, and nuclear energy as the primary electricity sources based on their prevalence across the US [10]. For petroleum, fuel production consists of the emissions associated with fossil fuel extraction, transportation to the refinery, storage, refining, production, and distribution to the fossil fuel-fired power station. For natural gas, this includes conventional natural gas and shale gas recovery, processing, transportation to the refinery, storage, refining, and distribution to the natural gas power station. For coal, production includes coal mining, cleaning, and distribution to the coal power station. Lastly, for nuclear energy, fuel production is the emissions from Uranium mining, enrichment, storage, and distribution to a nuclear power station. The emissions intensities of all stages of the power plants were obtained from GREET 2023 and are assumed to be constant throughout this study [7]. This data has been summarized in the **Error! Reference source not found.** below.

Table 4.3.2.1 *CO_2 and NO_x emissions intensities of different power plants' stages*

	Feedstock		Generation		Transmission & Distribution	
	CO_2 [g/kWh]	**NO_x [mg/kWh]**	**CO_2 [g/kWh]**	**NO_x [mg/kWh]**	**CO_2 [g/kWh]**	**NO_x [mg/kWh]**
Petroleum	33.6	18.01	908	0.7499	44.55	33.9
Natural Gas	70.5	57.43	421	333.4	23.76	17
Coal	15.8	6	987	762.7	51.12	39
Nuclear	2.42	0.29	0	11.4264	0.123	0.5841
Renewables	0	0	0	0	0	0

The EV charger, powerplant, and transmission efficiencies were varied as part of the uncertainty analysis with their values coming from various literature. This data has been tabulated in **Error! Reference source not found.** below.

Table 4.3.2.2 *Summary of EV charger, transmission and powerplant efficiencies with uncertainties*

Parameter	Minimum	Maximum	Average	Standard Deviation	Source
Level 3 EV Charger	85%	95%	90%	1.5%	Recurrent Auto [61]
Electricity Transmission	85%	92%	89%	1.2%	Schonek [62]
Coal Powerplant	27%	37%	32%	1.7%	Campbell [63]
Natural Gas Powerplant	50%	60%	55%	1.7%	NREL [64]
Petroleum Powerplant	30%	32%	31%	0.3%	Cleveland [65]
Nuclear Powerplant	33%	37%	35%	0.66%	University of Calgary [66]

The first charging scenario used to evaluate emissions from charging used the 2023 US average electricity grid. This electricity generation fraction data was obtained from the U.S. Energy Information Administration. It included 16.2% coal, 43.1% natural gas, 21.4% renewable sources, 18.6% nuclear power, and less than 1% miscellaneous sources, such as biomass [10]. As discussed in section 1.1, regional and time-of-day variations in the grid must be accounted for when calculating emissions from charging. Therefore, this study includes two additional charging scenarios for the BE truck. First, is recharging the battery using the time and location-based electricity generation mix also known as a “Time-dependent” analysis. This allowed for a more accurate emissions analysis because class 8 trucks in the US often travel cross-country and do not always stay within a state. This analysis considers the emissions impact of regional and time-of-day grid variation when charging. Lastly, annual reductions in electricity generation emissions based on future grid decarbonization were applied to the time-dependent analysis. The future grid assumption is covered in section 4.4. The time-dependent charging analysis and how all the powerplants were accounted for are explained in depth in the following section.

4.3.3. Time-dependent BE charging

This section discusses the detailed methodology of the time-dependent WTW emissions analysis for the BE truck by demonstrating calculations for the first stop along the long-haul route. The charging locations for the BE truck were manually found through Google Maps [67]. All dates and times are represented in Pacific Time to maintain consistency. **Error! Reference source not found.** marks the location of all the charging stops the BE truck had to make along the long-haul route. The final emissions calculations and locations for all charging stops along the long-haul and drayage routes are presented in section 8.5, section 8.6, and section 8.7.

Figure 4.3.3.1 *Recharging stop locations for the BE truck along the long-haul route.*

The trip started at location A on the map in San Francisco, CA. All eight charging stops during the forward journey are numbered in green. The truck then arrived at destination B Chicago, IL where it charged. The return trip then began, all eight charging stops during the return journey are numbered in orange. Finally, the truck returned to location A in San Francisco. The location, balancing authorities, and charging period of all stops have been summarized in Table 8.5.1 for the long-haul trip. The BE truck was charged at Electrify America with their “Hyperfast” charger. The charger was capable of charging the truck at 350 kW and 437.5 A [60]. A constant current was assumed during charging. Therefore, the charging time represents a minimum time as it ignores the constant voltage phase at the end of charging. The charging time, the energy required to fully charge the battery, and the C-rate were gathered by applying the constant charging current to the Simulink battery model. In this section, only the first stop's analysis, Lovelock, NV, is demonstrated. A similar approach was applied throughout all routes.

The trip began on 2023/07/01 at 6 am in this case. The distance between the starting location (San Francisco, CA) and the first charging location (Lovelock, NV) is 301 miles. According to the simulation, it took 6 hours and 38 minutes to cover the distance with the battery SOC dropping from 100% to 8.7%. The truck began charging on 2023/07/01 at 12:39 pm at a constant rate of 437.5 A. It took 2 hours and 5 minutes to charge the truck back to 100% SOC. The trip then continued on 2023/07/01 at 02:44 pm.

According to Eq. (3.4), the emissions intensity varies with the fraction of the electricity generation mix. In addition, the fraction depends on region and time. At Lovelock, NV, the real-time electric grid mixture during the charging period was obtained from its balancing authority, the Nevada Power Company (NEVP), on EIA's Hourly Electric Grid Monitor [9]. This was used to calculate the grid emissions intensities and thus the total CO_2 and NO_x emissions could be estimated as well. The data of the Hourly Electric Grid Monitor incorporates two critical data elements: hourly electricity generation by energy source and hourly subregional demand of the 65 electricity balancing authorities that operate the electric grid in the Lower 48 states in the US [9]. To determine the emissions intensity as a function of the desired time increment, some adaptations were made to the model. The first adaptation was to obtain the fraction of the electricity grid generation mix from the EIA data. Similar to past studies [68], The fraction of the electricity grid generation mix $f_{\mathrm{p,h}}$ from source type p during hour h is calculated using

$$f_{p,h} = \frac{G_{p,h}}{\sum_p G_{p,h}}, \tag{4.2}$$

$G_{p,h}$ is the electricity generation from source type p during hour h in MW. While the electricity grid generation mix $f_{\mathrm{p,h}}$ is given and calculated hourly, the fraction with minute increments was more ideal. This was because the vehicle charging periods were calculated based on minutes in the scope of this study. Therefore, the electricity grid generation mix $f_{\mathrm{p,h}}$ was interpolated every minute using the 'spline' method in MATLAB. Figure 4.3.3.2 Electricity grid data for the stop at Lovelock, NV (a) Share of the total electricity generation (b) CO_2 and (c) NO_x emissions intensity.

(a) plots the grid mixture for the charging period at Lovelock, NV. The emissions intensity in a minute was then calculated. Grid emissions I_{min} in g/min was calculated by the summation of emissions from the different power types p feeding the grid. The calculation is demonstrated below.

$$I_{min} = \sum_p I_p \times f_{p,min}, \tag{4.3}$$

I_p is the emissions intensity of the different types of power source p in g/kWh. The CO_2 and NO_x emissions intensity of different power sources were obtained from GREET 2023 and are summarized in **Error! Reference source not found.**. Figure 4.3.3.2 Electricity grid data for the stop at Lovelock, NV (a) Share of the total electricity generation (b) CO_2 and (c) NO_x emissions intensity.

(b) and (c) plots the CO_2 and NO_x emissions intensity for the charging period at Lovelock, NV.

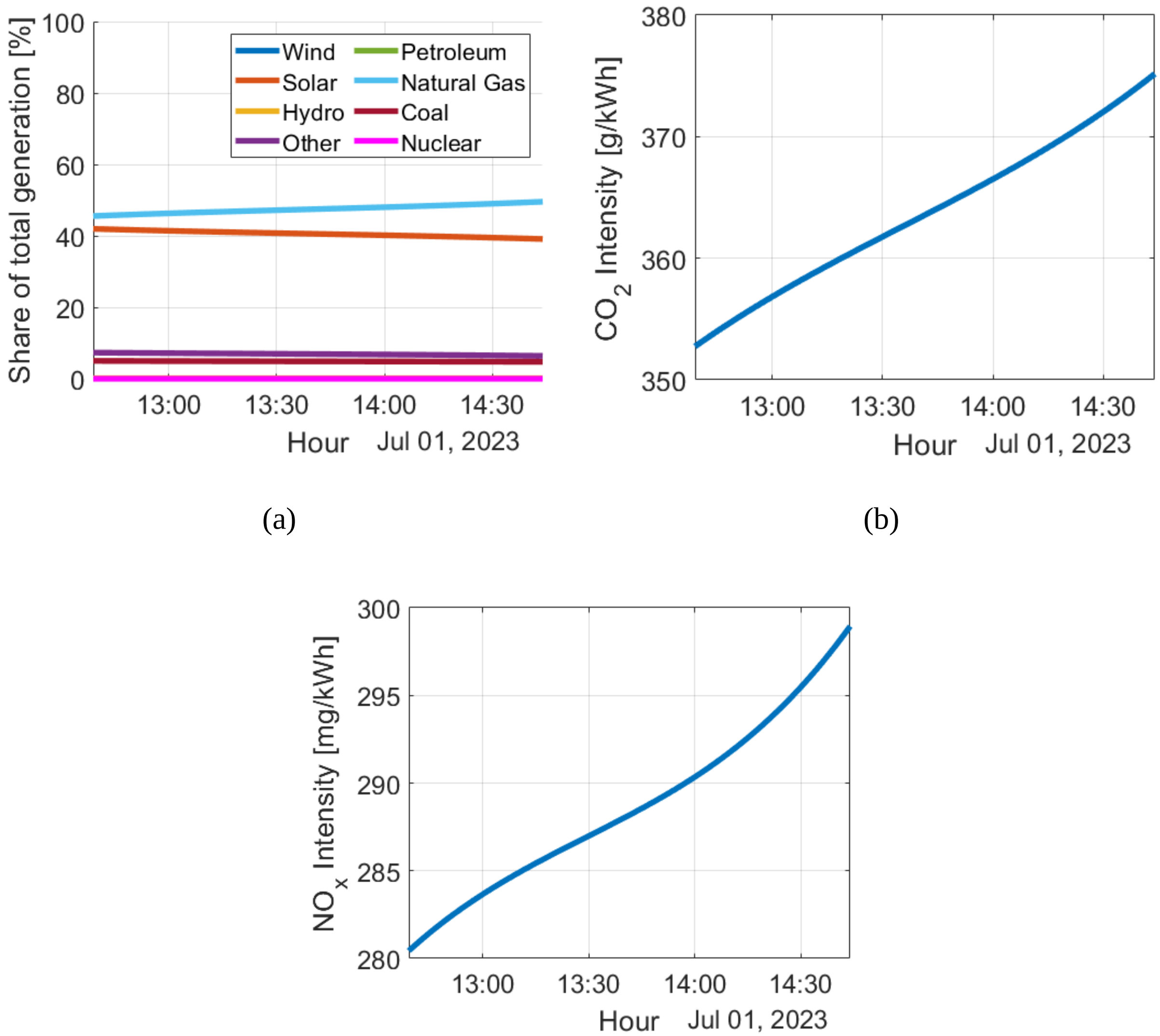

(a) (b)

(c)

Figure 4.3.3.2 *Electricity grid data for the stop at Lovelock, NV (a) Share of the total electricity generation (b) CO_2 and (c) NO_x emissions intensity.*

The mass flow rate of emissions was calculated using the given CO_2 and NO_x emissions intensity every minute. The emissions mass flow rate $\dot{m}_{emissions}$ in kg/min was calculated using

$$\dot{m}_{emissions} = \quad I_{min} \times \dot{W}_{charge} \, , \tag{4.5}$$

$\dot{W}_{charge}$ is the charging rate which is 350 kW for Electrify America's Hyperfast chargers. The CO_2 and NO_x emissions mass flow rate at the first charging station is presented in *Figure 4.3.3.3 Emissions mass flow rate at Lovelock, NV (a) CO_2 (b) NO_x*

. The total amount of emissions at each charging location and period was determined by taking the integral of the emissions mass flow rate ($\dot{m}_{emissions}$). The total amount of emissions E_L of location L in kg was calculated as:

$$E_L \;=\; \int_{t_{start\ charging}}^{t_{end\ charging}} \dot{m}_{\mathrm{emissions}}\,, \tag{4.6}$$

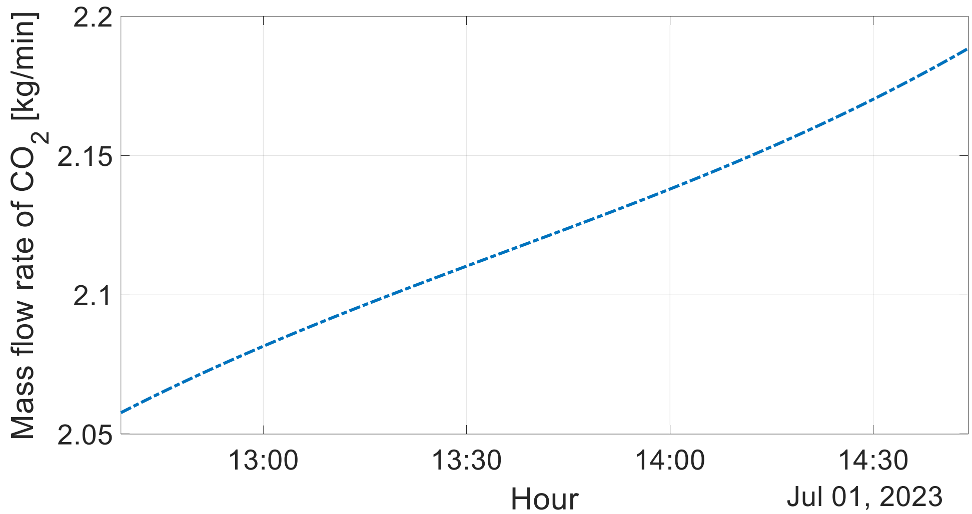

(a)

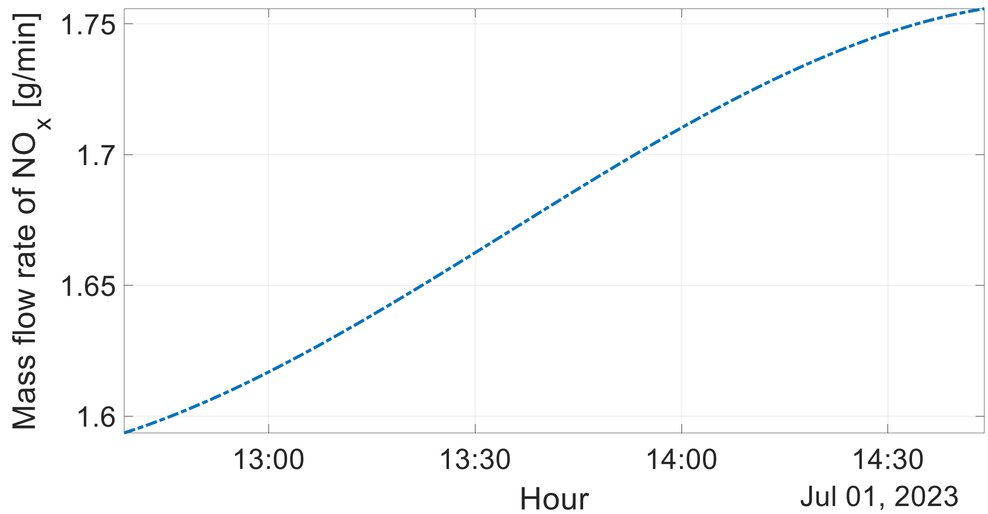

(b)

Figure 4.3.3.3 *Emissions mass flow rate at Lovelock, NV (a) CO_2 (b) NO_x*

where $t_{start\ charging}$ and $t_{end\ charging}$ are the start and end times for charging. This gives us 269 kg of CO_2 and 212 g of NO_x emissions from charging the truck at Elko, NV. Lastly, the total emissions, $E_{WTW,BE,time-dependent}$, for the trip was calculated by summing up each charging location's emissions.

4.4. Future Grid Assumption

EIA projects that by 2050 the share of renewable energy will increase by 138% and that coal, natural gas, and nuclear power plant energy will decrease by 10%, 67%, and 26%, respectively [11]. Therefore, it is crucial to consider the future reduction in emissions of the BE truck. The EIA's Annual Energy Outlook 2023 projected the net electricity generation from different energy sources. Data from EIA shown in Figure 1.2.1 and Eq. (3.4.7) were used to obtain the fraction of the future grid mix and its corresponding CO_2 and NO_x emissions intensity. **Error! Reference source not found.** and **Error! Reference source not found.** illustrates the projection of the grid CO_2 and NO_x emissions intensity from 2023 to 2050. This assumes the emissions intensity and efficiency of power plants are unchanged from 2023.

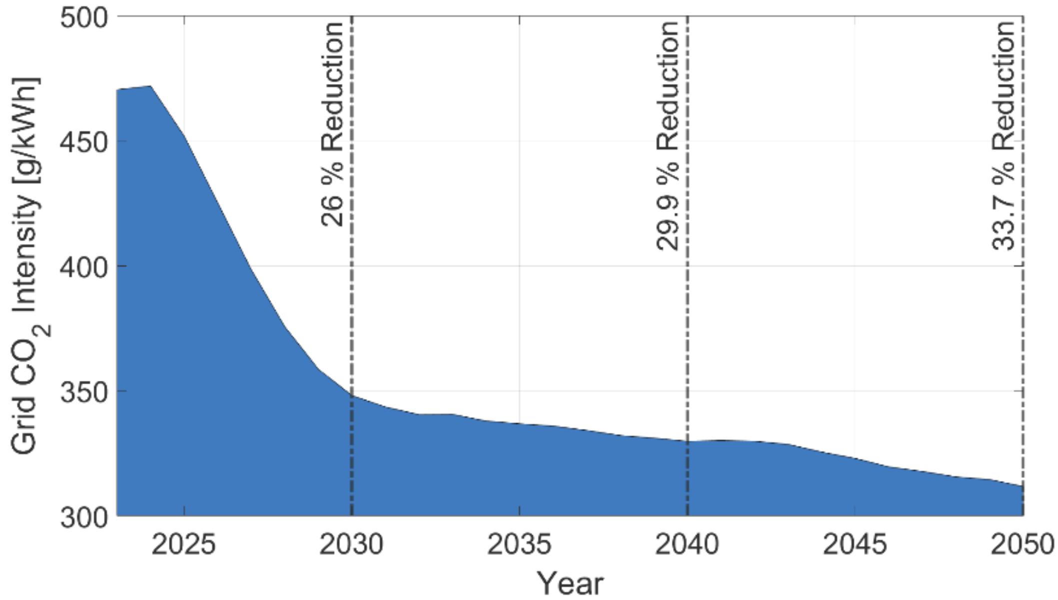

Figure 4.4.1 *Projection of the average US electricity grid CO_2 intensity to 2050*

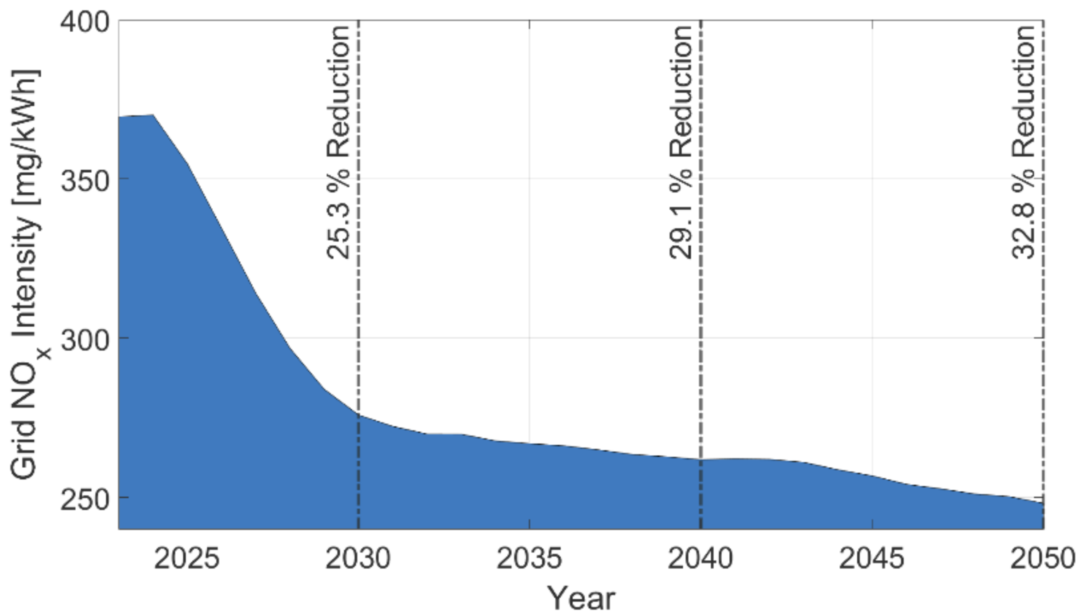

Figure 4.4.2 *Projection of the average US electricity grid NO_x emissions intensity to 2050*

As mentioned in Section 1.2, the truck's lifespan was assumed to be 10 years and therefore a reduction must be applied each year. While EIA only provided the reduction projection for the US average, the same reduction percentage was assumed for the time-dependent life cycle emissions analysis. The utilization phase emissions $E_{Utilization,BE,time-dependent}$ was calculated using

$$E_{Utilization,BE,time-dependent} = \sum_{years} (E_{WTW,BE,time-dependent} \times \left(1 - r_{year}\right) \times \frac{d_{year}}{d_{drive\ cycle}}) , \tag{4.7}$$

where $E_{WTW,BE,time-dependent}$ is the WTW emissions from the time-dependent trip, r_{year} is the reduction of the emissions intensity of the future year, and d_{year} is the total distance the truck travels per year. The r_{year} calculations have been summarized in section 8.4.

4.5. Long-Haul Route

The route for this analysis consists of a 4262-mile round trip from San Francisco to Chicago. This route was selected because it is one of the most common trucking routes in the US [69]. This route was also selected because it covers both low-carbon (California) and high-carbon (Wyoming) grid-intensity states [70]. The trip was assumed to begin on 2023/07/01 at the UPS distribution center in San Francisco (320 San Bruno Ave, San Francisco, CA 94103). The destination was set as the UPS distribution center in Chicago (500 S Jefferson St, Chicago, IL 60607) [67]. The trip ended after the trucks returned to the UPS distribution center in San Francisco. **Error! Reference source not found.** illustrates the long-haul route.

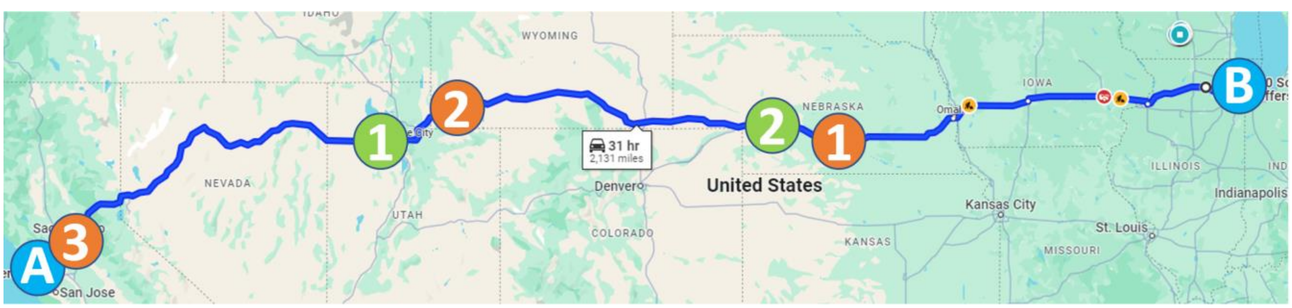

Figure 4.5.1 *Long-haul route with ICE truck's refueling stops in green and orange for forward and return journey respectively*

4.6. Drayage Routes

Drayage is defined as short-haul trips typically between ports, warehouses, and rail yards. These trips act as a link between longer intermodal transportation such as air and sea [71]. To contrast the location-based difference in electricity generation, two drayage routes were selected: A route in California to represent low-carbon grid-intensity states and a route in Indiana to represent high-carbon grid-intensity states [70]. The route in California from the Port of Los Angeles to the Duncot Warehouse (31968 Phillips Rd, McFarland, CA 93250) [67]. The route in Indiana from the FedEx Air Freight Center (4901 Crittenden Dr, Louisville, KY 40209) to a FedEx Office Center (3520 South St, Lafayette, IN 47905) [67]. The routes were based on the freight network maps from their respective states [72] [73]. The trucks will make stops along both routes to complete deliveries. The trips are repeated to simulate one week of driving to capture time-of-day variation in the electricity grid. Note that the start times of all long-haul and drayage trips were part of the uncertainty analysis. Figure 4.6.1 Drayage routes with BE truck's stops in green (a) California (b) Indiana.

illustrates the two drayage routes.

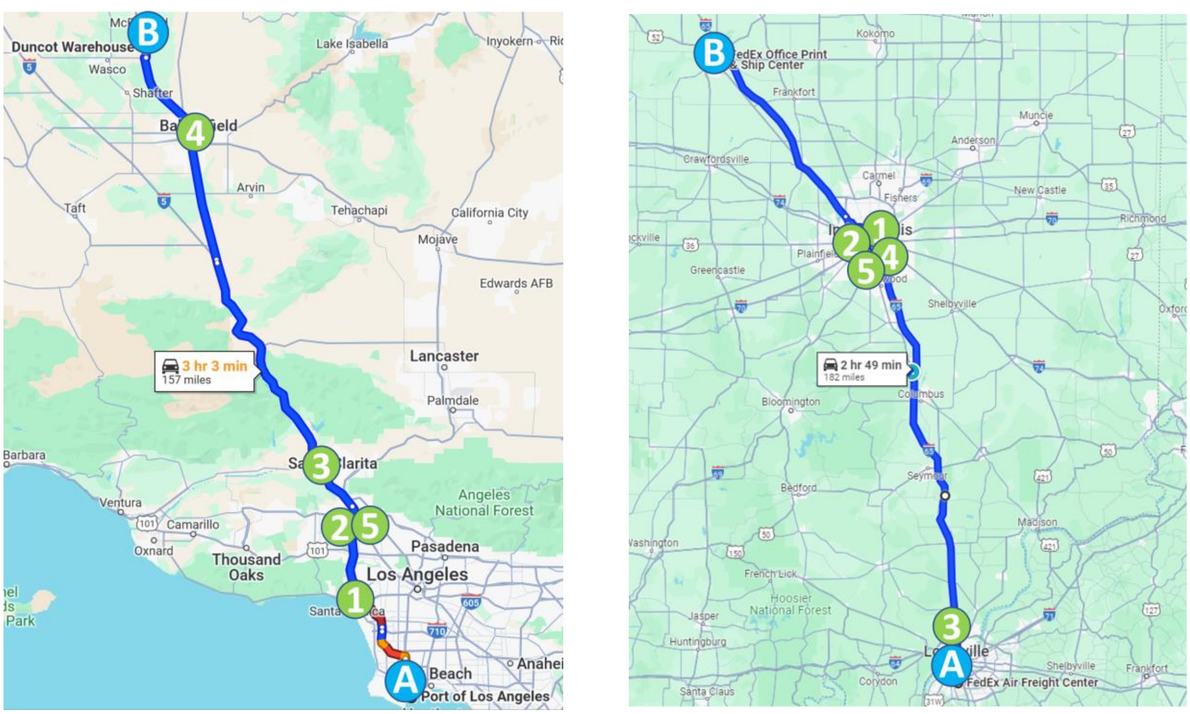

(a) (b)

Figure 4.6.1 *Drayage routes with BE truck's stops in green (a) California (b) Indiana.*

4.7. Life Cycle Assessment (LCA)

LCA is a well-established tool for assessing potential environmental impacts throughout a product's life cycle [74]. LCA assessment of environmental impacts includes vehicles' production, utilization, maintenance, and disposal. Disposal is also known as end-of-life treatment [75]. The goal of this study is to provide a comparative CO_2 and NO_x LCA of a conventional internal combustion engine and battery electric class 8 truck. The scope covers vehicle production and utilization phases. End-of-life phases were excluded from this study. The end-of-life emissions only account for a diminutive amount, less than 1% for ICE trucks and approximately 2% for BE trucks [76]. The life cycle emissions E_{Life} was calculated using

$$E_{Life} = E_{Production} + E_{Utilization} + E_{Maintenance}, \tag{4.8}$$

$E_{Production}$ and $E_{Maintenance}$ are the total production and maintenance phase emissions. $E_{Utilization}$ is the total utilization phase emissions during the truck's life. In this study, the utilization phase of the vehicle was assumed to include traveling one million miles with the target drive cycle over a 10 year period based on previous literature [76]. The utilization phase emissions $E_{Utilization}$ is calculated using

$$E_{Utilization} = E_{WTW} \times \frac{d_{Life}}{d_{Trip}}, \tag{4.9}$$

where E_{WTW} is the WTW emissions in kg. d_{Trip} is the total distance of the trip in miles. d_{Life} is the distance in miles covered in the truck's lifetime.

4.8. Freight Emissions comparison

Trucks exist to transport freight, and cargo capacity plays a crucial role in freight efficiency. Less cargo capacity means more trips are required to transport the same amount of cargo, hence increasing emissions. Therefore, a freight emissions analysis was essential for comparing the emissions of the trucks because the mass of the BE and SHE trucks depends heavily on the mass of the battery. The total mass of an ICE and SHE class 8 truck cannot exceed 80,000 lbs. (36,287 kg) and 82,000 lbs. (37,195 kg) for a BE class 8 truck in the U.S. according to the Federal Highway Administration (FHWA) [77], which limits the amount of cargo the truck can carry. The allowable mass of the cargo m_{cargo} was calculated using

$$m_{cargo} = m_{limit} - m_{truck\ total,} \tag{4.10}$$

where m_{limit} is the mass limit of the truck. $m_{truck\ total}$ is the total mass of a truck. In the transportation sector, it is common to measure the freight emissions in g per ton-mile [78]. This shows the emissions associated with moving one ton of freight for one mile. The freight emissions $E_{frieght}$ was calculated using the equation below. d_{life} is the total distance traveled in miles throughout the lifespan of the truck.

$$E_{frieght} = \frac{E_{Utilization}}{m_{cargo} \times d_{life}}. \tag{4.11}$$

4.9. Vehicle Production Emission

The total emissions from the production of all trucks were calculated. As described in previous literature [79], the vehicles' production emissions had different mixtures of raw materials and were manufactured in different locations. However, within the scope of this paper, only the critical components of the trucks were considered. This approach simplified the LCA and allowed a fair comparison of the trucks. The critical components include chassis, body, trailer, diesel powertrain, electric machines, and battery. The composition and weight of the common components: chassis, body, and trailer were considered the same for all trucks. The emissions associated with the production of the common components $E_{vehicle}$ was estimated using

$$E_{vehicle} = m_{chassis} \times I_{chassis} + m_{body} \times I_{body} + m_{trailer} \times I_{trailer}, \tag{4.12}$$

where $m_{chassis}$, m_{body} and $m_{trailer}$ are the mass of the truck chassis and body. $\mathrm{I_{chassis}}$ and $\mathrm{I_{body}}$ and $\mathrm{I_{trailer}}$ are the corresponding emissions intensity. Total emissions associated with the production of a heavy-duty diesel engine and gearbox, $E_{powertrain}$, was estimated using

$$E_{powertrain} = m_{powertrain} \times I_{powertrain,} \tag{4.13}$$

$$m_{powertrain} = m_{transmission} + \frac{P_{engine}}{\xi_{engine}}, \tag{4.14}$$

The mass of the engine was calculated using the rated power (P_{engine}) and the power density of a heavy-duty diesel engine (ξ_{engine}). $m_{transmission}$ is the transmission system's mass. Emissions associated with the production of an electric motor, E_{motor}, was estimated using the equations below

$$E_{motor} = m_{Motor} \times I_{EM,} \tag{4.15}$$

$$m_{motor} = \frac{T_{motor}}{\Phi_{EM}}, \tag{4.16}$$

where I_{EM} is the electric machine's emissions intensity, encompassing motors and generators. m_{Motor} is the electric motor mass. T_{motor} is the rated motor torque, and Φ_{EM} is the torque density of the electric machine. These equations are also used to calculate the emissions associated with the production of a generator, $E_{generator}$. The emissions associated with the production of a battery pack, $E_{battery}$, was estimated using

$$E_{Battery} = C_{battery} \times I_{battery}, \tag{4.17}$$

where $C_{battery,BE}$ is the battery capacity of the BE truck. $I_{battery}$ is the corresponding emissions intensity. The emissions associated with the production of the ICE ($E_{production,ICE}$), BE

($E_{production,BE}$), and SHE truck ($E_{production,SHE}$) were estimated using the equations below. $E_{EM,SHE}$ is the SHE truck's total motor and generator's production emissions.

$$E_{production,ICE} = E_{vehicle} + E_{powertrain,ICE}, \tag{4.18}$$

$$E_{production,BE} = E_{vehicle} + E_{motor,BE} + E_{battery,BE}, \tag{4.19}$$

$$E_{production,SHE} = E_{vehicle} + E_{EM,SHE} + E_{battery,SHE} + E_{powertrain,SHE}, \tag{4.20}$$

The production emissions of the trucks are associated with the mass of their components, battery capacity, and their corresponding emissions factors. The mass of the vehicle chassis ($m_{chassis}$), body (m_{body}) and, trailer ($m_{trailer}$) were assumed to be the same across all trucks and were obtained from GREET 2023 for a Class 8 Sleeper Cab truck [7]. The power density of a heavy-duty diesel engine ξ_{engine} was 0.28 kW/kg, and the torque density of a heavy-duty electric machine Φ_{EM} was 10.98 N-m/kg. The variation in emissions from producing the lithium-ion battery pack was varied as part of the uncertainty analysis which is tabulated in **Error! Reference source not found.**. The production emissions intensity values for all other truck components were obtained from GREET 2023 [7].

Table 4.9.1 *CO_2 and NO_x emissions intensities and uncertainties of a lithium-ion battery pack*

Parameter	Minimum	Maximum	Average	Standard Deviation	Source
Battery Production CO_2 [kg/kWh]	73	170	121.5	16.17	Syre et al. **[80]**
Battery Production NO_x [g/kWh]	84.1	97.2	90.65	2.18	Winjobi et al. **[81]**

Note that the mass of the battery $m_{battery}$ was calculated using the equation below. The gravimetric density $\xi_{battery}$ for a lithium-ion battery was obtained from GREET 2023 with the value of 0.179 kWh/kg.

$$m_{battery} = \frac{C_{battey}}{\xi_{battery}}, \tag{4.21}$$

4.10. Vehicle Maintenance Emission

The total amounts of emissions from vehicle maintenance were calculated considering only engine oil (ICE and SHE) and battery replacement (BE and SHE) as they are critical to the three trucks. Components common to all trucks such as tires were excluded from the maintenance phase as their emissions would be the same for all trucks. The total emissions associated with replacing the engine oil in a diesel engine's lifetime ($E_{engine\ oil\ replacement}$) is calculated using the equations below

$$E_{engine\ oil\ replacement} = m_{engine\ oil\ total} \times I_{engine\ oil,} \tag{4.22}$$

$$m_{engine\ oil\ total} = V_{engine\ oil} \times \rho_{engine\ oil} \times \left(\frac{d_{Life}}{d_{interval}}\right), \tag{4.23}$$

where $m_{engine\ oil\ total}$ is the total mass of engine oil used throughout the diesel engine's lifetime. $I_{\text{engine oil}}$ is the corresponding emissions intensity obtained from GREET 2023. $V_{engine\ oil}$ is the volume of engine oil required by a heavy-duty diesel engine, which is 43.8 liters [82]. $\rho_{engine\ oil}$ is the density of 10W-30 engine oil which is 0.855 kg/liter [83] . $d_{interval}$ is the oil drain interval mileage.

The total emissions associated with replacing the battery once in an electrified vehicle's lifespan was calculated using Eq. (4.17). A BE Truck's lithium-ion battery pack must be replaced once in a truck's lifetime according to studies by Sen [17] and Espinoza [14]. This was also assumed to be the case for the SHE truck.

5. LCA results in stages

This chapter presents the CO_2 and NO_x emissions from the LCA of Class 8 ICE, BE and SHE trucks operating on long-haul and drayage routes. The LCA results have been broken down into the following stages: production, maintenance, and WTW emissions. A comparison of the three different charging scenarios for the BE truck is presented (a) 2023 US average grid (b) Time-dependent grid (c) Future grid assumption. The trucks' freight CO_2 emissions, WTW NO_x emissions, and a breakdown of the trucks' weight are also discussed in this chapter.

5.1. Vehicle weight comparison

As the purpose of trucks is to transport cargo, it is important to examine the impact of the three powertrains on the trucks' cargo-carrying capacity.

Table 5.1.1 *Class 8 truck weight composition in lbs.*

	Engine & Gearbox	Fuel	Motor	Generator	Battery	Chassis	Body	Trailer	Truck Total	Cargo Capacity
ICE	3,315	710	-	-	-	6,161	3,346	11,264	24,801	55,199
BE	-	-	876	-	11,043				32,695	53,196
SHE	2,363	710	502	382	2,454				27,186	49,305

Error! Reference source not found. provides a breakdown of the weight composition of the three trucks. As mentioned in section 4.8, the maximum allowable weight (including cargo) of the ICE and SHE truck is 80,000 lbs. (36,287 kg) and 82,000 lbs. (37,195 kg) for the BE truck [77]. The weight of common components (chassis, body, and trailer) was assumed to be the same across all vehicles: 11,263 lbs. The common components amounted to about a quarter (25-26%) of the total weight of the trucks including cargo. In the ICE and SHE trucks, the engine and transmission amounted to the second largest share of the total weight (3-4%) with their weights ranging from 2,363-3,315 lbs. The motors and generator are lighter with their weights amounting to 0.6 to 1% of the total for the SHE and BE trucks, respectively. Fuel accounted for less than 1% of the total weight of the ICE and SHE trucks. In both the electrified vehicles, the battery pack had a considerable share of the total weight. The 200-kWh pack in the SHE truck weighed 2,454 lbs., amounting to 3% of the total weight. For the BE truck, the 900-kWh battery was the second largest contributor to its weight after the common components at 11,043 lbs. or 13% of the total weight. The ICE truck had the highest cargo-carrying capacity at 55,199 lbs. This was followed up by the SHE truck at 53,196 lbs. Lastly, the BE truck experienced an 11% reduction in its cargo-carrying capacity compared to the ICE truck at 49,305 lbs. For BE trucks, the battery makes a significant contribution to weight, due to the lower energy density of lithium-ion cells when compared to diesel fuel.

5.2. Well-to-Wheel emissions from a single trip

This section presents the route-based time-dependent WTW CO_2 and NO_x emissions for all three trucks along a single long-haul journey and a week of operation along the drayage routes. The location of the refueling and recharging stops have been mapped out for all trucks for all routes. Note that this study does not account for any regional variation in the production of diesel fuel and therefore the WTW emissions for the ICE and SHE trucks would be the same for all regions.

5.2.1. Time-dependent long-haul route-based

This section presents the WTW CO_2 and NO_x emissions from a single long-haul trip for all trucks. **Error! Reference source not found.**, **Error! Reference source not found.**, and **Error! Reference source not found.** map out all the charging and refueling stops that the BE, ICE, and SHE trucks had to make along the trip. The emissions are plotted as a function of time for all trucks in Figure 5.2.1.3 Cumulative WTW CO2 and NOX emissions for the long-haul trip (a) ICE Truck (b) BE Truck (c) SHE Truck.

with a 6 am trip start time. The dotted lines represent refueling/charging stops and the two destinations. All stops have also been tabulated in Table 8.5.1, Table 8.6.1, and Table 8.7.1

Figure 5.2.1.1 *Locations of refueling stops on the long-haul trip for the SHE truck.*

The ICE truck consumed 606 gallons (2,294 liters) of diesel fuel for the 4,262-mile trip. This gave an average fuel consumption of 7 miles per gallon, marginally higher than the typical state average MPG of 6.1 [84]. The ICE truck's greater fuel economy can be attributed to the cross-country highway route requiring fewer stops than a route within a state. The SHE truck consumed 308 gallons (1,439 liters) of diesel fuel because of its intermittent engine operation, this amounted to an average fuel consumption of 11 miles per gallon. In total, the ICE truck emitted 7,089 kg CO_2 and 4,250 g of NO_x throughout the trip. As expected, the SHE truck had reduced emissions at 4,285 kg CO_2 and 2555 g of NO_x. For both trucks, the bulk of these emissions came from the tailpipe (TTW). The BE truck stopped to recharge 16 times during the trip. The trip used 10,203 kWh of energy from the battery and covered 4,262 miles. This amounted to an efficiency of 2.4 kWh/mile. As mentioned in section 3.3.3, a BE truck typically has no TTW emissions, therefore WTW is assumed to consist only of the TTW emissions. The time-dependent charging analysis generated 6,461 kg of CO_2 and 5,014 g of NO_x throughout the journey with the charging stops in Wyoming and Nebraska being the largest contributors. A point of note is that in 2022, on average Nebraska generated 31% and 3% of its electricity from wind and natural gas, respectively [85]. However, **Error! Reference source not found.** (b) and (c) show that this was not representative of the grid at those stops with 40% of electricity coming from coal and 25-30% of electricity coming from natural gas. This is likely due to electricity from wind power being unpredictable and therefore more natural gas had to be used to meet the grid's demands.

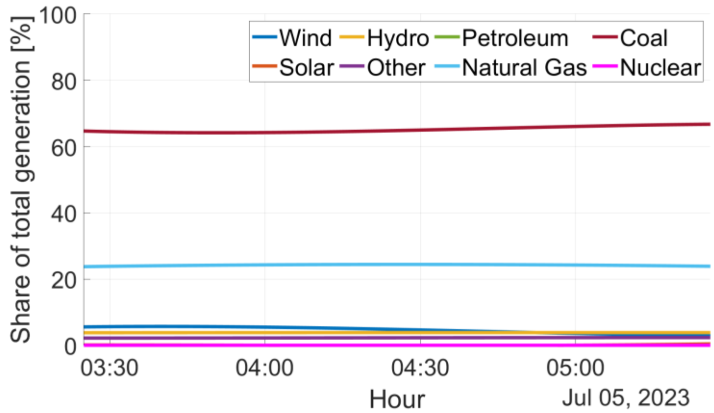

(a)

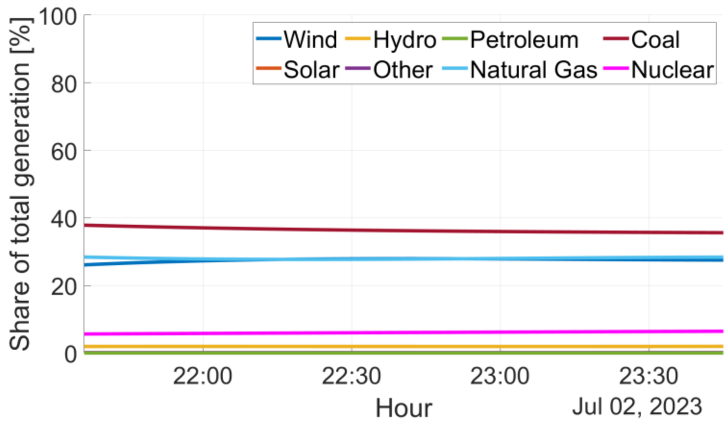

(b)

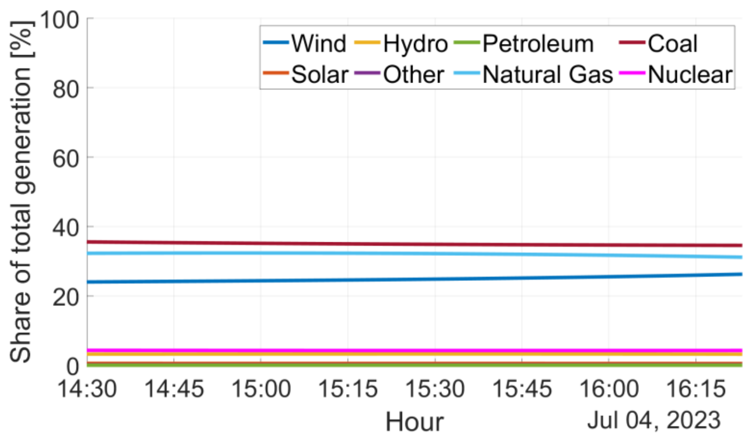

(c)

***Figure 5.2.1.2** Electricity grid share during stops at (a) 14. Rock Springs, WY (b) 6. Lexington, NE (c) 12. Ogallala, NE for the BE truck.*

As shown in Figure 5.2.1.3 Cumulative WTW CO2 and NOX emissions for the long-haul trip (a) ICE Truck (b) BE Truck (c) SHE Truck.

, both the ICE and SHE trucks completed the trip in 3 days and 18 hours. The BE truck, on the other hand, required 5 days to complete the trip. The delay was caused by the time spent charging the truck. On average, 1 hour and 40 minutes was spent at a charging station. Overall, the SHE truck showed a 37% reduction in CO_2 and a 40% reduction in NO_x when compared to the ICE truck's WTW emissions along the long-haul route. The time-dependent analysis on the other hand showed that the BE trucks achieved a negligible reduction of 3% in WTW emissions compared to the ICE truck along the same route.

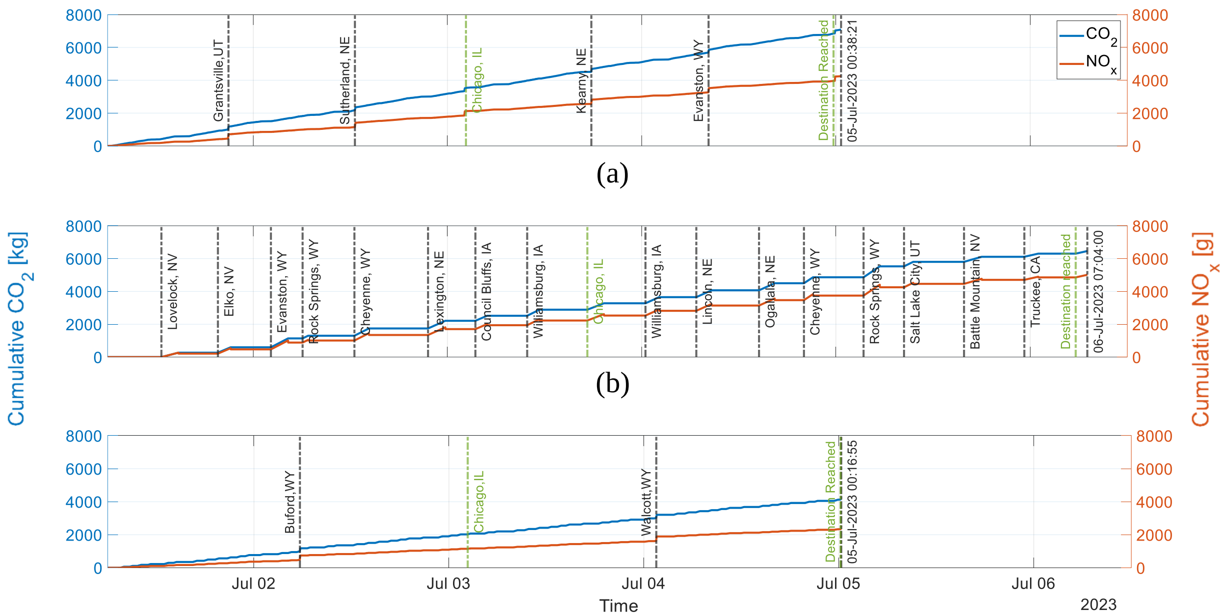

(c)

***Figure 5.2.1.3** Cumulative WTW CO2 and NOX emissions for the long-haul trip (a) ICE Truck (b) BE Truck (c) SHE Truck.*

5.2.2. Time-dependent drayage route-based

This section presents the WTW CO_2 and NO_x emissions from a week of driving along the drayage trip for all trucks. Figure 4.1.2 NREL's Fleet DNA drayage representative drive cycle (a) torque (b) speed data [23].

and Figure 5.2.2.1 Refueling stops for ICE truck along (a) California route (b) Indiana route & SHE stops for the same (c) (d)

map out all the charging and refueling stops that the BE, ICE, and SHE trucks had to make along the two routes. The emissions are plotted as a function of time for all trucks in Figure 5.2.2.3 Cumulative CO_2 and NO_x mass for drayage trips (a) ICE in CA (b) BE in IN (c) BE in CA (d) SHE in CA

. The dotted lines represent refueling/charging stops and the two destinations. All stops have also been tabulated in sections 8.5, 8.6, and, 8.7.

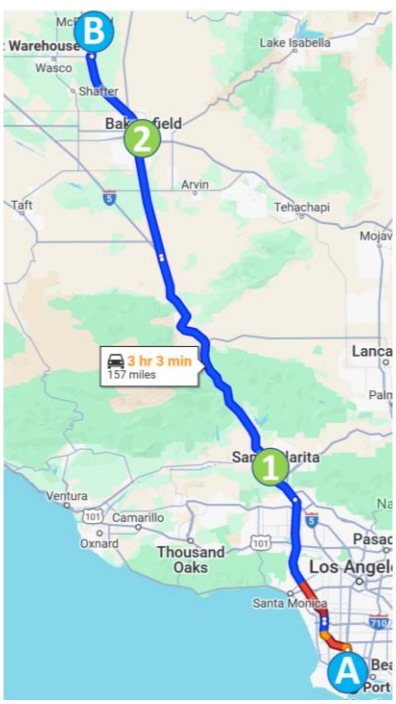

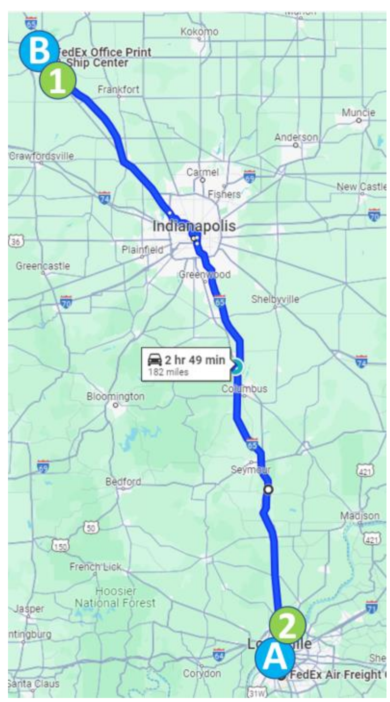

(a) (b)

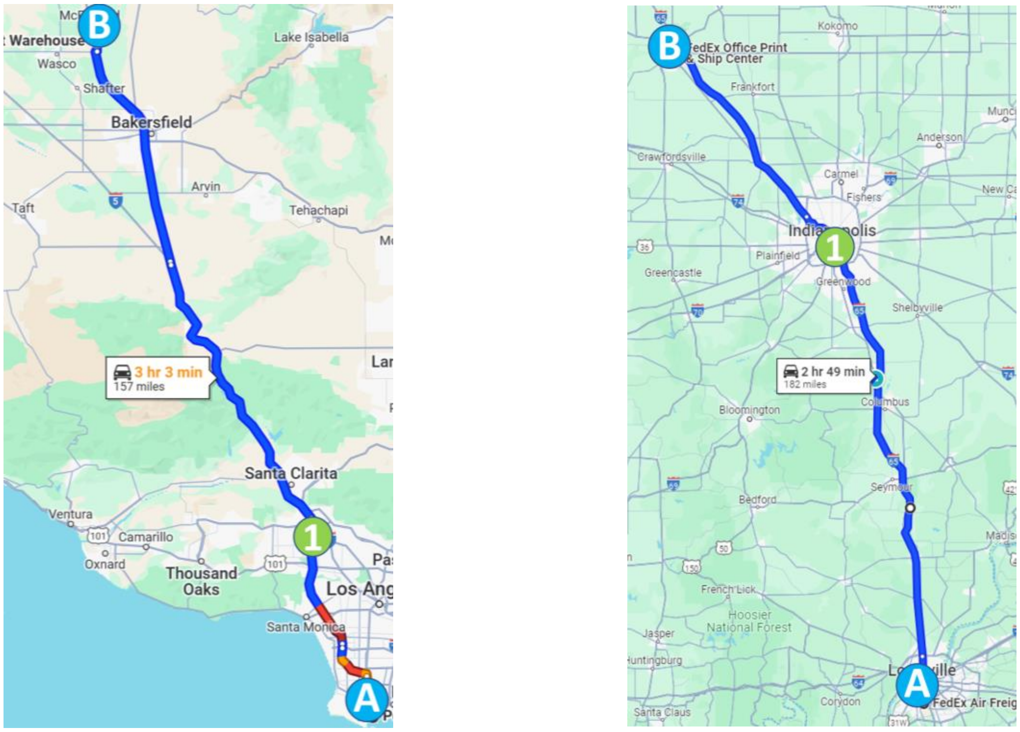

(c) (d)

***Figure 5.2.2.1** Refueling stops for ICE truck along (a) California route (b) Indiana route & SHE stops for the same (c) (d)*

On both drayage routes, the ICE and SHE trucks covered 1,357 miles in 3 days and 10 hours. The BE truck, needing more time to charge, covered the same distance in 3 days and 20 hours. The ICE truck managed an average fuel economy of 5.7 miles per gallon while consuming 236 gallons (894 liters) of diesel. This amounted to an 18% reduction in fuel economy compared to the long-haul trip. Like the long-haul trip, the SHE truck was more fuel-efficient in comparison. The SHE truck consumed 146 gallons (552 liters) of diesel fuel with an average fuel economy of 9.3 miles per gallon. In total, 2,812 kg and 1,708 kg of WTW CO_2 were generated throughout the trip for the ICE and SHE trucks respectively. This illustrates that the diesel engine in the ICE truck is not well suited to the more transient operation along drayage routes.

Along both routes, the BE truck stopped to recharge five times while using 3,628 kWh of battery energy. This amounted to an efficiency of 2.6 kWh/mile. A total of 1,079 kg CO_2 and 852 g of NO_x were emitted from charging the truck in California on average, making it the best-performing truck in this scenario. The charging stops made during nighttime had the highest emissions where natural gas was the primary source of electricity as solar energy could not be employed. This can be seen in Figure 5.2.2.2 Electricity grid share during stops at (a) 1. Burbank (b) 3. Santa Clarita (c) 4. Culver City for the BE truck along the CA route (6 am start)

which presents the electricity grid mix for three of the five stops when the truck started the journey at 6 AM.

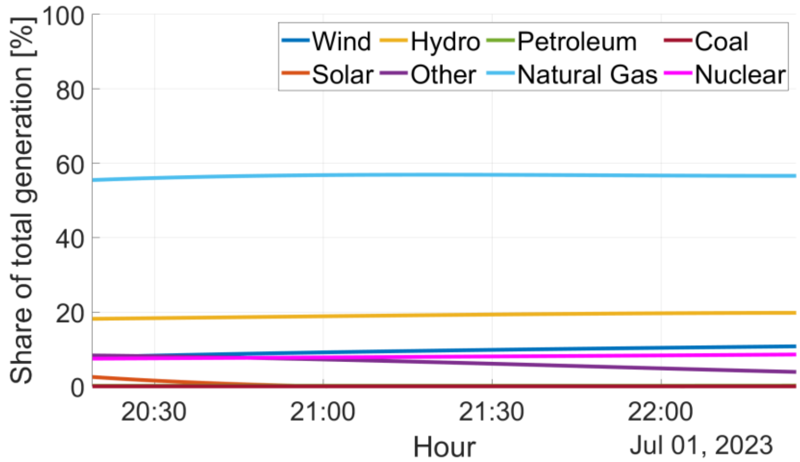

(a)

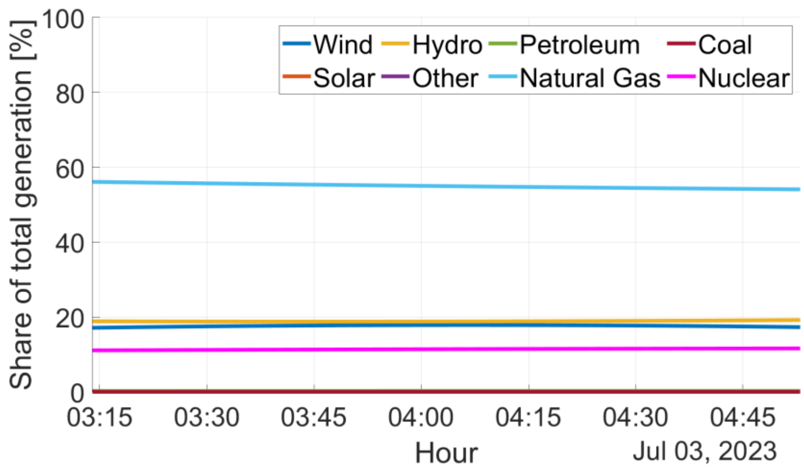

(b)

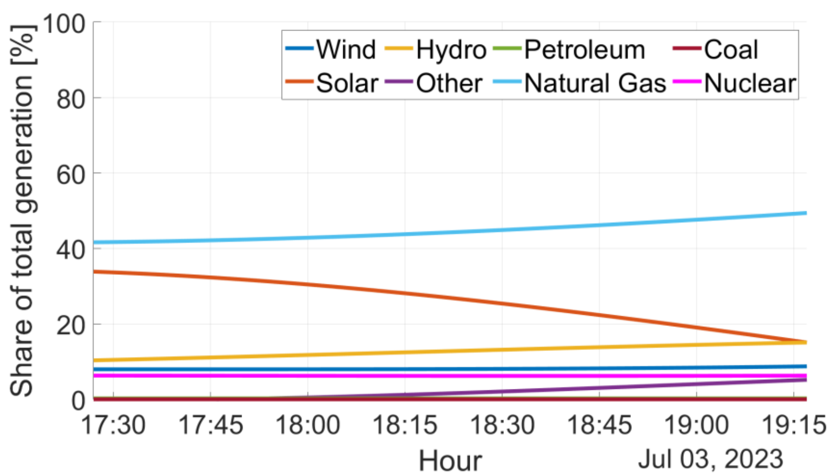

(c)

Figure 5.2.2.2 *Electricity grid share during stops at (a) 1. Burbank (b) 3. Santa Clarita (c) 4. Culver City for the BE truck along the CA route (6 am start)*

In comparison, the SHE truck showed a 37% and a 22% increase in WTW CO_2 and NO_x emissions compared to the SHE truck along the same route. The WTW emissions from the Indiana route presented some interesting results. The ICE truck had the highest CO_2 emissions overall but the BE truck had the highest NO_x emissions at 1,962 g from operating along the same route. Along the Indiana route, the SHE truck was the best performing, showing a 25% and a 44% reduction in NO_x WTW emissions when compared to the ICE and BE trucks respectively.

The two drayage routes highlight the differences in the emissions intensities of the grid that can exist between regions of the United States. As expected, the BE truck is the best choice for operating in regions with more renewables use like California. The BE truck can overcome emissions from a more carbon and NO_x-intensive grid with regenerative braking and greater powertrain efficiency when compared to the ICE truck as shown in the Indiana route case. However, the SHE truck emits less emissions than the BE truck along the same route by combining the electric motor's efficiency benefits without needing to plug into an emissions-intensive grid to charge.

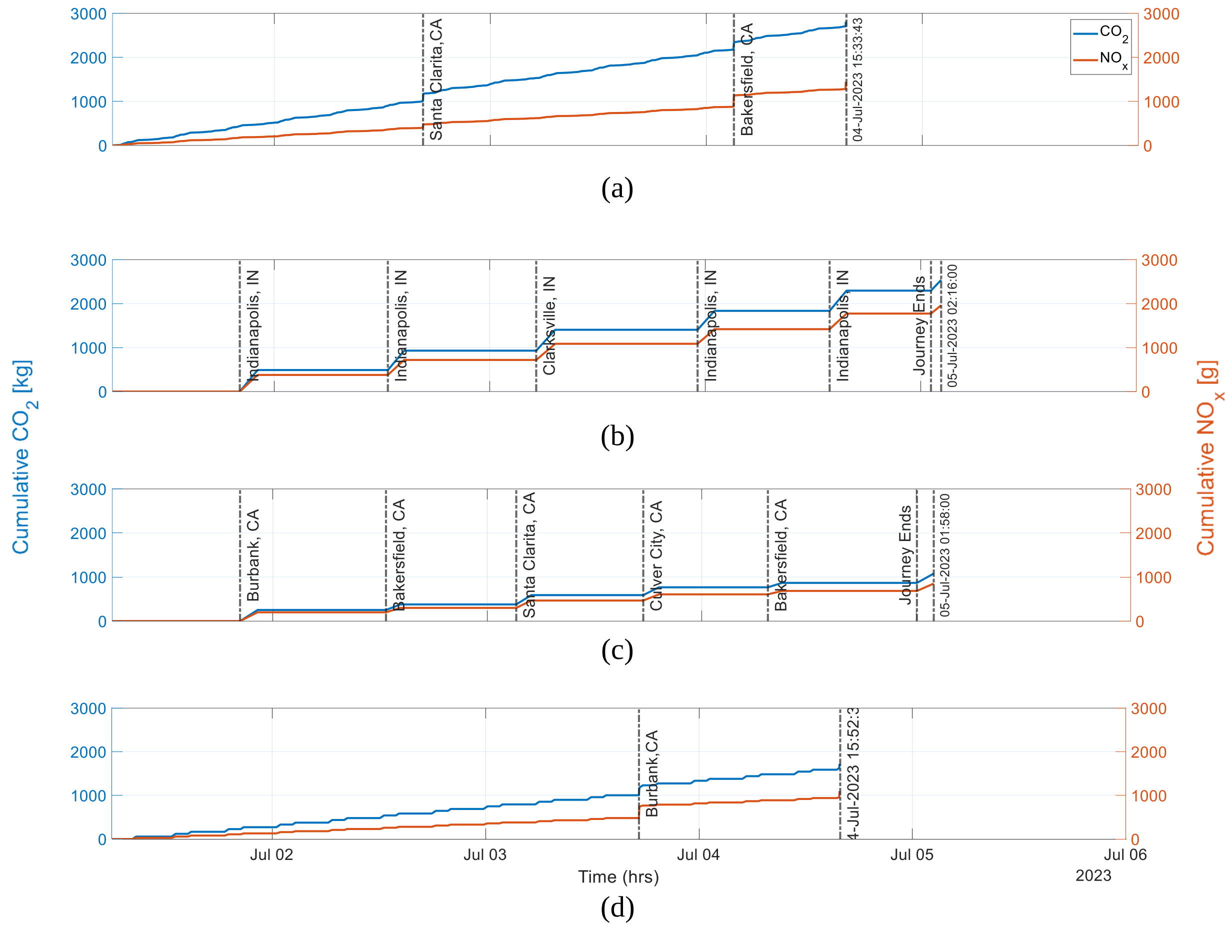

Figure 5.2.2.3 *Cumulative CO_2 and NO_x mass for drayage trips (a) ICE in CA (b) BE in IN (c) BE in CA (d) SHE in CA*

5.3. Life cycle analysis (LCA) results

This section will add the production and maintenance emissions to the WTW emissions, presented in the previous section, to complete the LCA. Life cycle, freight CO_2 and WTW NO_x emissions rates of the ICE, BE and SHE trucks with two drive cycles and three different BE charging scenarios are also presented in this section. Note that for the ICE and SHE drayage results, only a single case of emissions is presented. This was because state-wise and regional variation in fueling emissions intensity data was not found in the literature and therefore both routes will have the same emissions.

The BE truck operation scenario first included charging the truck with the 2023 US average electricity grid. Secondly, a time-dependent trip-based LCA was performed to illustrate a more realistic emissions analysis. Lastly, a future electricity grid assumption was introduced to the time-dependent trip-based LCA. The lifespan of a class 8 truck was assumed to be 10 years traveling one million miles. For this analysis, the lifespan of the BE truck was assumed to start in 2023 and end in 2032.

5.3.1. Vehicle production and maintenance emissions

Error! Reference source not found. depicts the breakdown of the CO_2 and NO_x emissions from vehicle production for the three trucks in tons and kg, respectively. The error bars illustrate the variation in CO_2 and NO_x emissions intensity for battery production. During the production of the body, chassis, and trailer for all trucks, 35 tons of CO_2 and 38.5 kg of NO_x were emitted. The production emissions for the powertrain components: engine, motor, and generator are not significant compared to the total vehicle production, ranging from 1.3 to 4.5 tons of CO_2 and 1.3 to 5 kg of NO_x. However, the process of extracting the materials and manufacturing lithium-ion batteries generates a momentous amount of CO_2 emissions as noted from the literature review. As a result, for the BE truck, the production of the 900-kWh battery emitted 109 tons of CO_2 and 81.6 kg of NO_x on average. Similarly, for a SHE truck, the 200-kWh pack production emitted 24 tons of CO_2 and 18 kg of NO_x on average. In total, 40, 64, and 145 tons of CO_2 and 43.7, 62, and 121 kg of NO_x were emitted to produce the ICE, SHE, and BE trucks respectively. The production of the SHE truck emitted about 1.6 times more CO_2 and 2.8 times more NO_x than that from the ICE truck's production. On the other hand, the BE truck's production emitted about 3.6 times more CO_2 and 2.8 times more NO_x than the ICE truck's.

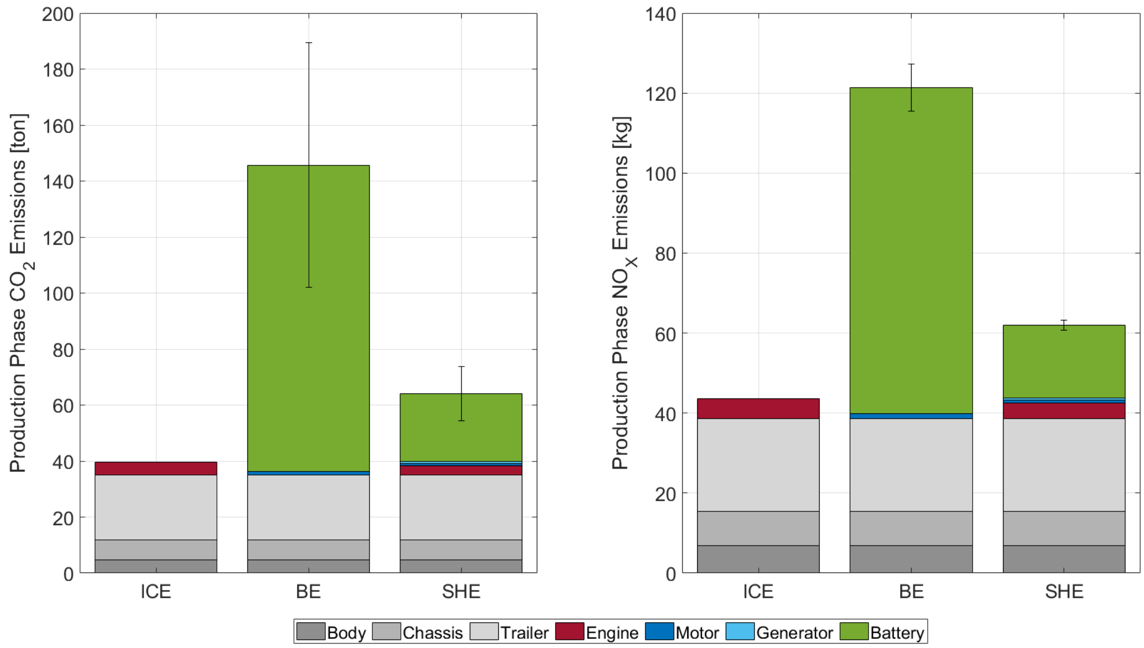

Figure 5.3.1.1 *Comparison of CO2 and NO_x emissions from vehicle production for ICE, BE, and SHE trucks*

The maintenance phase of the trucks includes emissions from replacing the engine oil (ICE and SHE) and replacing the battery (BE and SHE) once in the trucks' life. Figure 5.3.2.1.1 CO2 emissions from Class 8 trucks on the long-haul route using route-based time-dependent analysis (a) LCA (b) Freight, Figure 5.3.2.1.2 NO_x emissions from Class 8 trucks on the long-haul route using route-based time-dependent analysis (a) LCA (b) WTW

, Figure 5.3.2.2.1 CO_2 emissions from Class 8 trucks on the drayage routes using route-based time-dependent analysis (a) LCA (b) Freight, and **Error! Reference source not found.** depict the CO_2 and NO_x emissions, respectively, from vehicle maintenance for the three trucks. The ICE truck achieved 5.7 and 7 miles per gallon on the drayage and long-haul routes, respectively. According to engine manufacturers, this gives the ICE truck an oil drain interval d_{interval} of 50,000 to 60,000 miles [82]. The average of this, 55,000 miles, was taken as the replacement interval. Similarly, the SHE truck's oil drain interval is 75,000 miles given its lighter workload with 9.2 and 11 miles per gallon. Therefore, according to Eq. (4.23), the engine oil needs to be changed 22 and 13 times during the ICE and SHE truck's lifetime. This amounts to 1.1 to 1.9 tons of CO_2 and 2.1 to 3.5 kg of NO_x being emitted from replacing the engine oil in the SHE and ICE trucks based on Eq. (4.22).

The disparity between the emissions from the maintenance phase of the trucks, and the production phase, is due to the large amount of CO_2 and NO_x emissions from the production of lithium-ion batteries. As a single battery replacement was considered in the BE and SHE truck's lifetime, the same amount of emissions were emitted to produce the batteries as in the production stage. In comparison, the emissions from engine oil production are insignificant. Accordingly, 1.9, 25.4, and 109 tons of CO_2 and 3.5, 20.2, and 81.6 kg of NO_x were emitted to maintain the ICE, SHE, and BE trucks respectively.

5.3.2. Complete life cycle emissions

This section presents the life-cycle CO_2 and NO_x emissions as well as the WTW emissions rate for the same in terms of g CO_2/ton-mile and g NO_x/kWh. Note that production and maintenance emissions remained unchanged for all BE truck charging scenarios. In addition, WTT emissions were assumed to be constant across the country as regional variation in data was not found.

5.3.2.1. Long-Haul Route

Figure 5.3.2.1.1 ***CO2 emissions from Class 8 trucks on the long-haul route using route-based time-dependent analysis (a) LCA (b) Freight*** and Figure 5.3.2.1.2 ***NO_x emissions from Class 8 trucks on the long-haul route using route-based time-dependent analysis (a) LCA (b) WTW*** present the CO_2 and NO_x emissions from three trucks driving along the long-haul route. The 2023 US average grid scenario resulted in 1,325 tons of CO_2 and 1,133 kg of NO_x LCA emissions for the BE truck along the long-haul route. This corresponded to a 22% reduction in CO_2 emissions compared to the ICE truck's LCA. However, the BE truck in this scenario had 8% higher NO_x emissions than the ICE truck's LCA because of the additional emissions from producing the two battery packs required in the truck's life. When looking at the WTW NO_x emissions rate, the BE truck in this scenario showed a 7% reduction compared to the ICE truck's emissions rate.

The more realistic case, the time-dependent analysis, netted 1,782 tons of CO_2 and 1,047 kg of NO_x LCA emissions. This scenario resulted in 68.3 g CO_2/ton-mile freight emissions and 0.58 g NO_x/kWh for the BE truck which is a 43% and 49% increase in WTW CO_2 and NO_x emissions, respectively, compared to the 2023 US Average charging case. This brought the BE truck's freight CO_2 emissions to be comparable to that of the ICE truck at about 68 g/ton-mile. However, the BE truck's WTW NO_x emissions rate is now 13% higher than the ICE truck's. After applying the future grid emissions intensity reductions from 2023-2032, the BE truck's WTW CO_2 and NO_x emissions were reduced by about 13%. This assumption reduced the BE truck's freight CO_2 emissions to be 14% lower than the ICE truck's. However, the WTW NO_x emissions rate of the BE truck was still higher at 0.49 g/kWh.

The ICE truck emitted 1,702 tons of CO_2 and 1,047 kg of NO_x. The tailpipe TTW emissions were the predominant contributors to the ICE truck's LCA emissions, amounting to 84% (1,424 tons) of the LCA CO_2 and 61% (635 kg) of the LCA NO_x. This was followed up by the WTT phase at 237 tons CO_2 and 365 kg NO_x (14-35%). Lastly, production and maintenance contributed to less than 5% of the LCA. The SHE truck had the lowest life cycle emissions at 1,134 tons of CO_2 and 745 kg of NO_x on average. It is worth noting that even in the worst case, the SHE truck had the lowest freight CO_2 and WTW NO_x emissions rate compared to the ICE truck and all the BE truck's charging scenarios. On average, the SHE truck showed a 21% reduction in freight emissions (45.3

g CO_2/ton-mile) and a 31% reduction in the WTW NO_x emissions rate (0.29 g/kWh) when compared to the BE truck with the time-dependent future grid assumption. As discussed in section 5.1, the SHE truck only sees a minor penalty to its cargo-carrying capacity due to its much smaller and lighter battery pack which helps keep its freight emissions low.

In section 5.2.1, we saw that the single-trip WTW emissions for the BE truck with the time-dependent charging assumption were lower than that of the ICE truck. However, when the production and maintenance phases of the trucks were incorporated, the life-cycle CO_2 and NO_x emissions in 10 years were higher for the BE truck than the ICE and SHE trucks. For all charging cases, despite zero TTW emissions, the LCA indicated that the emissions for the BE truck moved upstream. In the time-dependent charging case, 12% of the emissions came from producing two batteries required in the truck's lifetime and the WTT phase emissions accounted for 85% of the life cycle emissions. The battery production emissions were the largest contributor to the uncertainty in the BE truck's LCA results and the powerplant efficiencies were the main contributor to the freight CO_2 and WTW NO_x emissions rate. In the ICE and SHE truck cases, the variation in TTW emissions was the primary contributor to the uncertainty in CO_2 and NO_x emissions.

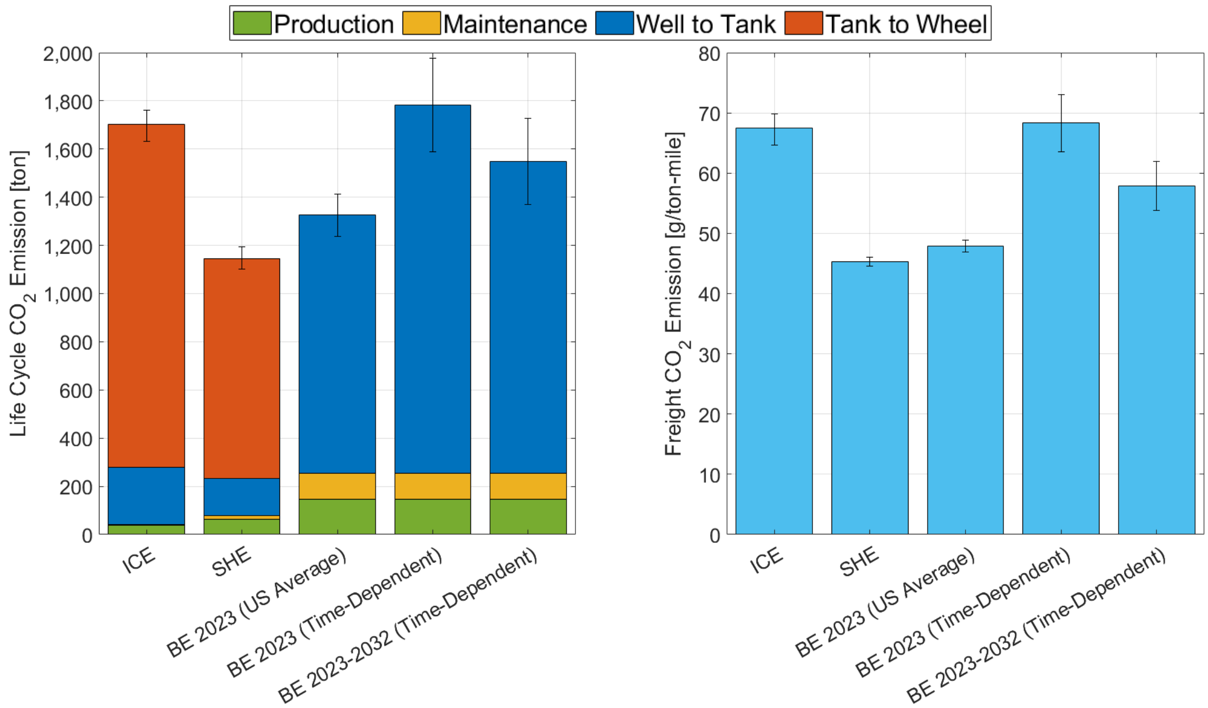

(a) (b)

Figure 5.3.2.1.1 *CO2 emissions from Class 8 trucks on the long-haul route using route-based time-dependent analysis (a) LCA (b) Freight*

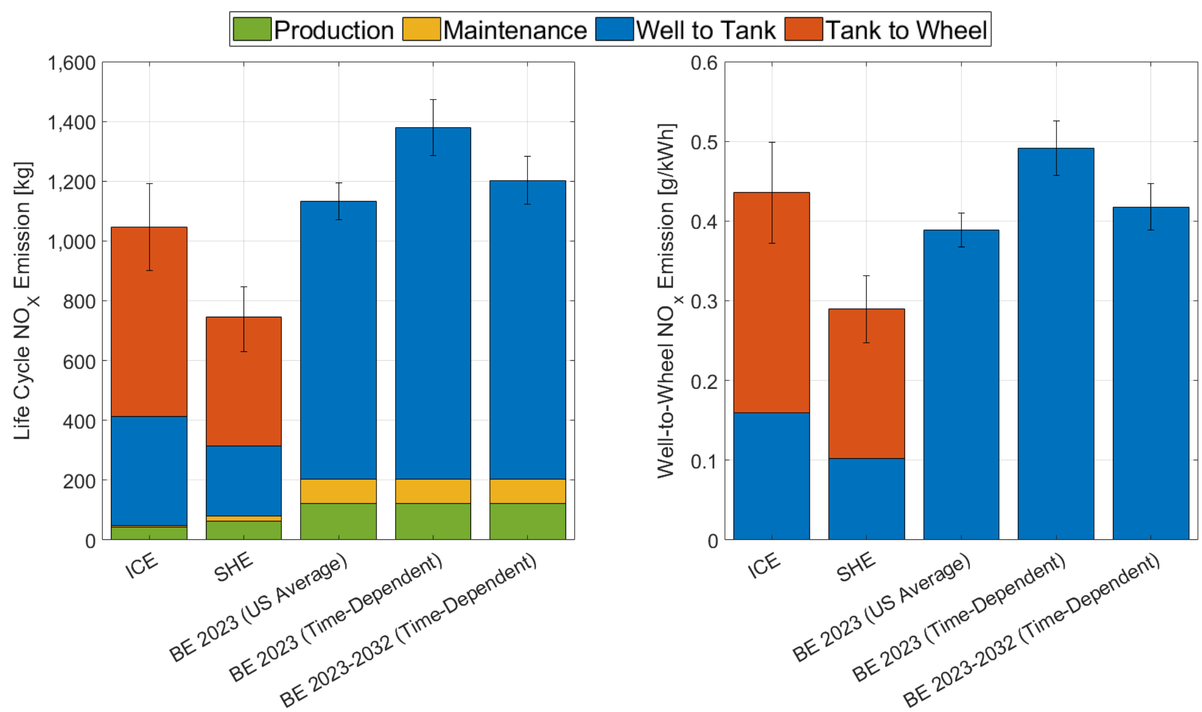

(a) (b)

Figure 5.3.2.1.2 *NO_x emissions from Class 8 trucks on the long-haul route using route-based time-dependent analysis (a) LCA (b) WTW*

5.3.2.2. Drayage Route

Figure 5.3.2.2.1 CO_2 emissions from Class 8 trucks on the drayage routes using route-based time-dependent analysis (a) LCA (b) Freight and **Error! Reference source not found.** present the CO_2 and NO_x emissions from three trucks driving along the long-haul route. In terms of both CO_2 and NO_x emissions, the BE truck was the best option for the drayage route in California. We see notably reduced life-cycle emissions at 1,051 tons of CO_2 and 831 kg of NO_x. Even when the WTW emissions rates are isolated, the BE truck has lower rates at 35.6 g CO_2/ton-mile and 0.23 g NO_x/kWh. This is about a 36% and 22% reduction in the WTW CO_2 and NO_x emissions rates respectively when compared to the SHE trucks. The ICE truck demonstrated over 1.8 times the CO_2 and NO_x emissions rate compared to the BE truck along the California drayage route.

Comparing the BE truck's performance along California and Indiana drayage routes is where see the impact location has on the WTW emissions. The BE truck shows much greater emissions rates, 84.4 g CO_2/ton-mile and 0.55 g NOx/kWh, along the Indiana route. This means that for the BE truck in Indiana to transport the same amount of cargo through the same distance as in California, over twice the amount of CO_2 and NO_x will be emitted. The BE truck's freight emissions along the Indiana route were now comparable to that of the ICE truck but the NO_x rate was still 20% higher. Even with the application of the future grid assumption which reduces emissions by 10-13%, the BE truck's WTW NOx emissions rate were now comparable to the ICE truck's. The disparity in the BE truck's WTW emissions between the California and Indiana drayage routes is because of the differences in their respective electricity grids. When charging along the California route, the electricity grid mix primarily consisted of natural gas, solar, hydroelectric, and wind power. On the other hand, the grid in Indiana consisted primarily of natural gas and coal. The coal powerplants are the primary contributor to the BE truck's high charging emissions as the emissions intensity of the coal plant is over double that of a natural gas plant which can be seen in **Error! Reference source not found.**.

The SHE truck, in total, emitted 1,378 tons of CO_2 and 883 kg of NO_x in its lifetime. This made the SHE truck the best option for operation along the Indiana drayage route, as it demonstrated a 30-33% reduction in freight CO_2 and WTW NO_x emissions rate compared to the ICE truck. The ICE and SHE trucks demonstrated higher life-cycle emissions along the drayage routes when compared to the long-haul route despite the lower average power requirement of the drive cycle. This is because of the reduced fuel economy from the increased number of stops along the drayage routes, which in turn increased in lifetime WTW CO_2 and NO_x emissions. This showed that diesel engines are not as well suited to more transient operation.

In the previous section, we saw that the BE truck is not well suited to cross-country journeys that mostly involve highway driving as its life-cycle emissions were comparable to that of today's ICE truck. The drayage route results illustrate the strengths of the BE and SHE trucks. An electric motor is more efficient at "stop-and-go" driving which is more common in drayage and more urban routes such as last-mile delivery [6]. The BE and SHE trucks can better utilize regenerative braking on such routes. This combined with operation in areas with significant renewable electricity use can net major benefits in emissions for the BE truck. On the other hand, the SHE truck is better suited for operations along routes confined in regions with large portions of the generated electricity coming from coal and natural gas use.

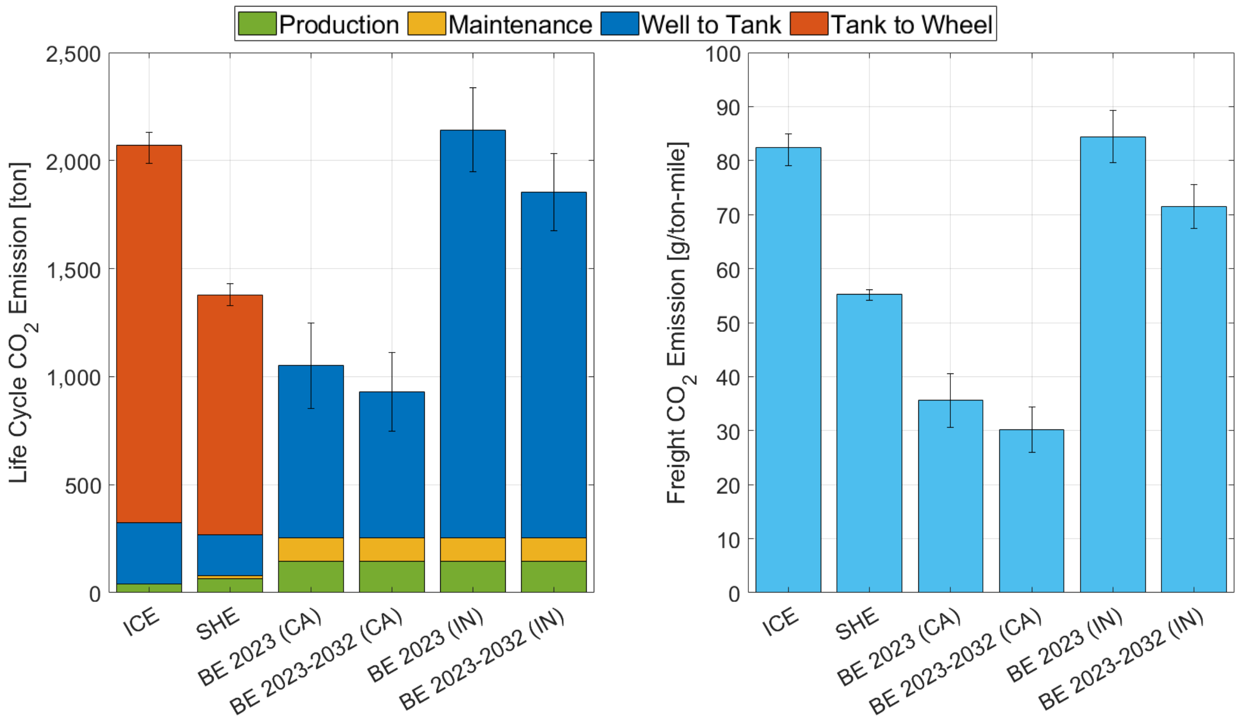

(a) (b)

Figure 5.3.2.2.1 *CO_2 emissions from Class 8 trucks on the drayage routes using route-based time-dependent analysis (a) LCA (b) Freight*

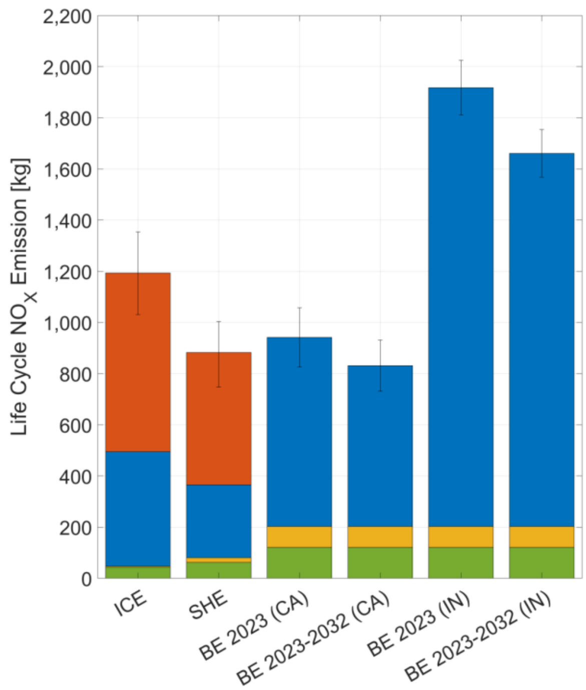

(a)

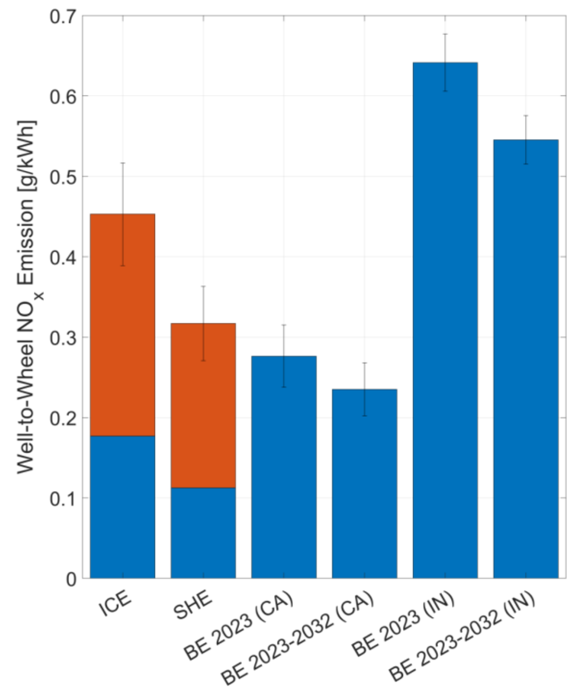

(b)

Figure 5.3.2.2.2 *NO_x emissions from Class 8 trucks on the drayage routes using route-based time-dependent analysis (a) LCA (b) WTW*

6. Conclusions and future work

This chapter will present the conclusions from this study followed up by recommendations for future developments to expand this study.

6.1. Conclusions

In this research, a dynamic and modular vehicle-powertrain simulation tool was used to simulate the performance and emissions impact of powertrain choice for class 8 trucks in two different use cases: long-haul and drayage. The powertrains considered were a conventional diesel engine (ICE), a battery electric (BE), and a series-hybrid electric (SHE) powertrain. A life-cycle analysis (LCA) was performed for a more comprehensive look at CO_2 and NO_x emissions in a truck's lifecycle by incorporating emissions from production, maintenance, fuel, and electricity production. The analysis included the BE truck charging with the current US average grid mixture and a route-based time-dependent grid mixture. The route-based time-dependent approach incorporated regional and time-based variations in the electricity grid and its consequent impact on CO_2 generation. Lastly, a future grid decarbonization assumption was applied to the BE truck. Based on the scope and assumptions of this study, the conclusions and insight gained are as follows:

The US average grid assumption resulted in the CO_2 and NO_x emissions from charging the BE truck being underestimated for regions with heavy coal and natural gas use and overestimated for regions with large shares of renewable sources of electricity. This misrepresented the LCA, freight, and WTW emissions rate when operating along the cross-country long-haul route, as the time-dependent analysis resulted in higher emissions for the BE truck than the ICE and SHE trucks. The LCA and WTW emissions rate results demonstrated that BE trucks are only suited for operation on routes within regions with large shares of renewable sources of electricity. However, class 8 trucks often travel across multiple regions, operating in regions and periods with higher-than-average electricity grid emissions intensity. Additionally, the future grid assumption reduced the BE truck's LCA and freight emissions to be comparable to the ICE truck's but still greater than the SHE truck's emissions for the long-haul trip.

The LCA, freight CO_2, and WTW NO_x rate emissions results showed that for cross-country trips and operations in regions with large shares of electricity from coal and natural gas, the SHE truck has the highest potential for lowering CO_2 and NO_x emissions. This is because of the following reasons: first, the SHE truck's smaller lithium-ion battery, compared to the BE truck's, reduces its production environmental impact. Secondly, since the diesel engine operates at an efficient point to power the generator and experiences less transient operation than the ICE truck's engine, it greatly reduces its tailpipe emissions. Lastly, electric motors are more efficient at stop-and-go driving required for drayage use when compared to a heavy-duty diesel engine. The electrified trucks can better take advantage of regenerative braking on such routes when compared to highway driving. Hybrid trucks can serve as a crucial step towards reducing emissions as they can use existing refueling infrastructure in regions with more carbon-intensive electricity generation.

6.2. Recommendations for future work

Despite the novelties of this study, there is room for additional developments. The SHE powertrain requires a more reliable and sophisticated control method. The current rule-based control scheme for the SHE powertrain was adapted from the work of Gao et at. [34]. The charging operation was managed by keeping the battery's SOC between 20% and 80%. This control scheme provided a constant engine speed and current for the engine and generator to provide sufficient current to charge the battery at a c-rate below 1. However, the current required from the motor to the battery fluctuates based on the simulated drive cycle which in turn fluctuates the required current from the generator to charge the battery at the desired c-rate. This means that a constant setpoint, at times, causes the charging c-rate of the battery to fluctuate above and below 1 C. Therefore, a more complex control scheme that can vary the setpoint of the engine and generator in accordance to the drive cycle load needs to be developed. The Ideal Operation Line (IOL) control strategy [79] can be implemented in the model. The IOL strategy prioritizes minimum fuel consumption of the engine by tracking the minimum BSFC operation line and tracing the input from both the battery SOC and the motor power required.

Stronger emissions standards are on the horizon for HD vehicles. In 2022, the EPA set ultra-low NO_x emissions standards for HD trucks made in the year 2027 or later at 0.035 g NO_x/bhp-hr which is about an 80% reduction from the standards over 20 years ago [19]. This would lead to drastic tailpipe NO_x emissions reductions for diesel and hybrid trucks and therefore this study should be conducted in a 2027 setting, accounting for improvements in the electricity grid and stricter emissions standards.

Lastly, similar studies often consider the outlook on the decarbonization of the electricity grid as described in section 2. Rarely attention is directed towards the LCA emissions impact of decarbonizing fuel production and using renewable fuels. Xu et al. [86] conducted an LCA of renewable diesel and biodiesel by covering emissions from land use change to consumption via vehicle operation. The authors concluded that renewable diesel and biodiesel led to GHG emissions reductions ranging from 40% to 69% when compared to petroleum diesel. Hydrogen (H_2) is another potential prospect for reducing GHG emissions as it is carbon-free and conventional ICEs can be modified to work with H_2 as a fuel [87]. Although H_2 combustion does emit NO_x from high-temperature oxidation, after-treatment systems can reduce those emissions as well [88]. These reduced TTW emissions can be combined with decarbonized H_2 production to reduce the WTT emissions of an ICE truck as well. Iyer et al. [6] noted over an 88% reduction in WTT CO_2 emissions when they switched H_2 production from steam methane reforming of natural gas to electrolysis of water using electricity from solar energy.

7. References

[1] EPA, "Inventory of U.S. Greenhouse Gas Emissions and Sinks: 1990–2022," U.S. Environmental Protection Agency, EPA 430-R-24-004. Accessed: Jan. 22, 2024. [Online]. Available: https://www.epa.gov/ghgemissions/inventory-us-greenhouse-gas-emissions-and-sinks

[2] D.-Y. Lee, A. Elgowainy, A. Kotz, R. Vijayagopal, and J. Marcinkoski, "Life-cycle implications of hydrogen fuel cell electric vehicle technology for medium- and heavy-duty trucks," *Journal of Power Sources*, vol. 393, pp. 217–229, Jul. 2018, doi: 10.1016/j.jpowsour.2018.05.012.

[3] H. Lohse-Busch *et al.*, "Automotive fuel cell stack and system efficiency and fuel consumption based on vehicle testing on a chassis dynamometer at minus 18 °C to positive 35 °C temperatures," *International Journal of Hydrogen Energy*, vol. 45, no. 1, pp. 861–872, Jan. 2020, doi: 10.1016/j.ijhydene.2019.10.150.

[4] C. Ledna, M. Muratori, A. Yip, P. Jadun, and C. Hoehne, "Decarbonizing Medium- & Heavy-Duty On-Road Vehicles: Zero-Emission Vehicles Cost Analysis," NREL/TP-5400-82081, 1854583, MainId:82854, Mar. 2022. doi: 10.2172/1854583.

[5] P. Egede, T. Dettmer, C. Herrmann, and S. Kara, "Life Cycle Assessment of Electric Vehicles – A Framework to Consider Influencing Factors," *Procedia CIRP*, vol. 29, pp. 233–238, 2015, doi: 10.1016/j.procir.2015.02.185.

[6] R. K. Iyer, J. C. Kelly, and A. Elgowainy, "Vehicle-cycle and life-cycle analysis of medium-duty and heavy-duty trucks in the United States," *Science of The Total Environment*, vol. 891, p. 164093, Sep. 2023, doi: 10.1016/j.scitotenv.2023.164093.

[7] Argonne National Laboratory, *GREET 2023*. Argonne National Laboratory. [Online]. Available: https://greet.anl.gov/

[8] "A Matter of Balance," Transmission Agency of Northern California (TANC). [Online]. Available: https://www.tanc.us/understanding-transmission/a-matter-of-balance/

[9] U.S. Energy Information Administration (EIA), "Hourly Electric Grid Monitor." Accessed: Oct. 20, 2023. [Online]. Available: https://www.eia.gov/electricity/gridmonitor/index.php

[10] "What is U.S. electricity generation by energy source?," U.S. Energy Information Administration (EIA). Accessed: Apr. 05, 2024. [Online]. Available: https://www.eia.gov/tools/faqs/faq.php?id=427&t=3

[11] "Annual Energy Outlook 2023," U.S. Energy Information Administration (EIA), AEO2023. [Online]. Available: https://www.eia.gov/outlooks/aeo/

[12] B. Marmiroli, M. Venditti, G. Dotelli, and E. Spessa, "The transport of goods in the urban environment: A comparative life cycle assessment of electric, compressed natural gas and diesel light-duty vehicles," *Applied Energy*, vol. 260, p. 114236, Feb. 2020, doi: 10.1016/j.apenergy.2019.114236.

[13] S. Martinez-Boggio, J. Monsalve-Serrano, A. García, and P. Curto-Risso, "High Degree of Electrification in Heavy-Duty Vehicles," *Energies*, vol. 16, no. 8, p. 3565, Apr. 2023, doi: 10.3390/en16083565.

[14] V. Balboa-Espinoza, J. Segura-Salazar, C. Hunt, D. Aitken, and L. Campos, "Comparative life cycle assessment of battery-electric and diesel underground mining trucks," *Journal of Cleaner Production*, vol. 425, p. 139056, Nov. 2023, doi: 10.1016/j.jclepro.2023.139056.

[15] Y. Zhao and O. Tatari, "Carbon and energy footprints of refuse collection trucks: A hybrid life cycle evaluation," *Sustainable Production and Consumption*, vol. 12, pp. 180–192, Oct. 2017, doi: 10.1016/j.spc.2017.07.005.

[16] J. C. Kelly *et al.*, "Comprehensive Cradle to Grave Life Cycle Analysis of On-Road Vehicles in the United States Based on GREET," presented at the WCX SAE World Congress Experience, Detroit, Michigan, United States, Apr. 2024, pp. 2024-01–2830. doi: 10.4271/2024-01-2830.

[17] B. Sen, T. Ercan, and O. Tatari, "Does a battery-electric truck make a difference? – Life cycle emissions, costs, and externality analysis of alternative fuel-powered Class 8 heavy-duty trucks in the United States," *Journal of Cleaner Production*, vol. 141, pp. 110–121, Jan. 2017, doi: 10.1016/j.jclepro.2016.09.046.

[18] J. Short and D. Crownover, "Understanding the CO2 Impacts of Zero-Emission Trucks," American Transport Research Institute (ATRI), May 2022. [Online]. Available: https://truckingresearch.org/2022/05/new-atri-research-quantifies-the-environmental-impacts-of-zero-emission-trucks/

[19] G. Wartgow, "Closer look: Heavy-duty engine trends," Fleet Owner. Accessed: Apr. 20, 2024. [Online]. Available: https://www.fleetowner.com/equipment/article/21284802/diesel-engines-navigating-the-2027-emissions-regulations-and-beyond

[20] X. Liu, A. Elgowainy, R. Vijayagopal, and M. Wang, "Well-to-Wheels Analysis of Zero-Emission Plug-In Battery Electric Vehicle Technology for Medium- and Heavy-Duty Trucks," *Environ. Sci. Technol.*, vol. 55, no. 1, pp. 538–546, Jan. 2021, doi: 10.1021/acs.est.0c02931.

[21] R. Guderian, "EFFECTS OF PHOTOCHEMICAL OXIDANTS ON PLANTS." U.S. Environmental Protection Agency, May 24, 2002. Accessed: May 02, 2024. [Online]. Available: https://cfpub.epa.gov/si/si_public_record_Report.cfm?Lab=NHEERL&dirEntryId=36285

[22] V. Saj *et al.*, "A Model-Based Design Framework for Electric VTOL Aircraft." Oct. 22, 2023. Accessed: Feb. 20, 2023. [Online]. Available: https://www.researchgate.net/publication/374900905_A_Model-Based_Design_Framework_for_Electric_VTOL_Aircraft

[23] L. Guzzella and C. H. Onder, *Introduction to Modeling and Control of Internal Combustion Engine Systems*. Berlin, Heidelberg: Springer Berlin Heidelberg, 2010. doi: 10.1007/978-3-642-10775-7.

[24] Mathworks, "CI Engine Speed-Density Air Mass Flow Model - MATLAB & Simulink." Accessed: Aug. 06, 2024. [Online]. Available: https://www.mathworks.com/help/autoblks/ug/compression-ignition-engine-speed- density-breathing-model.html

[25] J. B. Heywood, *Internal combustion engine fundamentals*, Second edition. New York: McGraw-Hill Education, 2018.

[26] P. Moraal and I. Kolmanovsky, "Turbocharger Modeling for Automotive Control Applications," presented at the International Congress & Exposition, Mar. 1999, pp. 1999-01–0908. doi: 10.4271/1999-01-0908.

[27] M. J. Abedin, H. H. Masjuki, M. A. Kalam, A. Sanjid, S. M. A. Rahman, and B. M. Masum, "Energy balance of internal combustion engines using alternative fuels," *Renewable and Sustainable Energy Reviews*, vol. 26, pp. 20–33, Oct. 2013, doi: 10.1016/j.rser.2013.05.049.

[28] B. Fulton, S. Petrovic, M. Van Nieuwstadt, J. Dixon, D. Roettger, and A. Arevalo, "Turbocharger Turbine Inlet Isentropic Pressure Observer Model," *SAE Int. J. Engines*, vol. 8, no. 4, pp. 1638–1651, Apr. 2015, doi: 10.4271/2015-01-1617.

[29] H. Jääskeläinen, "Diesel Exhaust Gas," DieselNet. [Online]. Available: https://dieselnet.com/tech/diesel_exh.php

[30] S. M. Mousavi G. and M. Nikdel, "Various battery models for various simulation studies and applications," *Renewable and Sustainable Energy Reviews*, vol. 32, pp. 477–485, Apr. 2014, doi: 10.1016/j.rser.2014.01.048.

[31] O. Tremblay and L.-A. Dessaint, "Experimental Validation of a Battery Dynamic Model for EV Applications," *WEVJ*, vol. 3, no. 2, pp. 289–298, Jun. 2009, doi: 10.3390/wevj3020289.

[32] M. Mayur, S. C. DeCaluwe, B. L. Kee, and W. G. Bessler, "Modeling and simulation of the thermodynamics of lithium-ion battery intercalation materials in the open-source software Cantera," *Electrochimica Acta*, vol. 323, p. 134797, Nov. 2019, doi: 10.1016/j.electacta.2019.134797.

[33] B. Shabani and M. Biju, "Theoretical Modelling Methods for Thermal Management of Batteries," *Energies*, vol. 8, no. 9, pp. 10153–10177, Sep. 2015, doi: 10.3390/en80910153.

[34] J.-P. Gao, G.-M. G. Zhu, E. G. Strangas, and F.-C. Sun, "Equivalent fuel consumption optimal control of a series hybrid electric vehicle," *Proceedings of the Institution of Mechanical Engineers, Part D: Journal of Automobile Engineering*, vol. 223, no. 8, pp. 1003–1018, Aug. 2009, doi: 10.1243/09544070JAUTO1074.

[35] K. Yu, R. Vijayagopal, and N. Kim, "Design of a Rule-Based Controller and Parameter Optimization Using a Genetic Algorithm for a Dual-Motor Heavy-Duty Battery Electric Vehicle," presented at the WCX SAE World Congress Experience, Mar. 2022, pp. 2022-01–0413. doi: 10.4271/2022-01-0413.

[36] National Renewable Energy Laboratory (NREL), "Drive Cycle Analysis Tool (DriveCAT)." [Online]. Available: https://www.nrel.gov/transportation/drive-cycle-tool/

[37] X. Liu, S. Singh, E. L. Gibbemeyer, B. E. Tam, R. A. Urban, and B. R. Bakshi, "The carbon-nitrogen nexus of transportation fuels," *Journal of Cleaner Production*, vol. 180, pp. 790–803, Apr. 2018, doi: 10.1016/j.jclepro.2018.01.090.

[38] X. Liu, K. Reddi, A. Elgowainy, H. Lohse-Busch, M. Wang, and N. Rustagi, "Comparison of well-to-wheels energy use and emissions of a hydrogen fuel cell electric vehicle relative to a conventional gasoline-powered internal combustion engine vehicle," *International Journal of Hydrogen Energy*, vol. 45, no. 1, pp. 972–983, Jan. 2020, doi: 10.1016/j.ijhydene.2019.10.192.

[39] L. Athanasopoulou, H. Bikas, and P. Stavropoulos, "Comparative Well-to-Wheel Emissions Assessment of Internal Combustion Engine and Battery Electric Vehicles," *Procedia CIRP*, vol. 78, pp. 25–30, 2018, doi: 10.1016/j.procir.2018.08.169.

[40] M. Q. Wang, "Development and use of GREET 1.6 fuel-cycle model for transportation fuels and vehicle technologies.," ANL/ESD/TM-163, 797947, Aug. 2001. doi: 10.2172/797947.

[41] C. Zhang, A. Kotz, K. Kelly, and L. Rippelmeyer, "Development of heavy-duty vehicle representative driving cycles via decision tree regression," *Transportation Research Part D: Transport and Environment*, vol. 95, p. 102843, Jun. 2021, doi: 10.1016/j.trd.2021.102843.

[42] R. Prohaska, A. Konan, K. Kelly, and M. Lammert, "Heavy-Duty Vehicle Port Drayage Drive Cycle Characterization and Development," *SAE Int. J. Commer. Veh.*, vol. 9, no. 2, pp. 331–338, Sep. 2016, doi: 10.4271/2016-01-8135.

[43] "New California requirements for on-road and off-road heavy-duty vehicles," California Air Resources Board (CARB). Accessed: Jun. 17, 2024. [Online]. Available: https://ww2.arb.ca.gov/new-california-requirements-road-and-road-heavy-duty-vehicles#:~:text=Beginning%20January%201%2C%202024%2C%20only,be%20zero%2Demission%20by%202035

[44] "X15 Performance Series (2024)," Cummins Inc. Accessed: Nov. 03, 2023. [Online]. Available: https://www.cummins.com/engines/x15-performance-series-2024

[45] "Trucking," Engine Technology Forum. Accessed: Oct. 07, 2022. [Online]. Available: https://enginetechforum.org/trucking

[46] S. Moghadasi, Y. Long, L. Jiang, S. Munshi, G. McTaggart-Cowan, and M. Shahbakhti, "Design and performance analysis of hybrid electric class 8 heavy-duty regional-haul trucks with a micro-pilot natural gas engine in real-world highway driving conditions," *Energy Conversion and Management*, vol. 309, p. 118451, Jun. 2024, doi: 10.1016/j.enconman.2024.118451.

[47] R. Morris, "How Many Gallons of Fuel Do Semi-Trucks Hold (Answers Here)?," Certified Fleet Services. Accessed: Jun. 30, 2024. [Online]. Available: https://certifiedfleetservices.com/how-many-gallons-of-fuel-do-semi-trucks-hold-answers-here/

[48] Tesla Inc., *Tesla Semi Delivery Event*, (Dec. 01, 2022). Accessed: Aug. 23, 2023. [Online Video]. Available: https://www.youtube.com/watch?v=LtOqU2o81iI

[49] G. Solberg, "The Magic of Tesla Roadster Regenerative Braking," Tesla. Accessed: Mar. 05, 2023. [Online]. Available: https://www.tesla.com/blog/magic-tesla-roadster-regenerative-braking

[50] J. Zhang, X. Lu, J. Xue, and B. Li, "Regenerative Braking System for Series Hybrid Electric City Bus," *WEVJ*, vol. 2, no. 4, pp. 363–369, Dec. 2008, doi: 10.3390/wevj2040363.

[51] M. Kane, "New Photo Reveals Tesla Semi's Massive Battery System," InsideEVs. Accessed: Feb. 17, 2024. [Online]. Available: https://insideevs.com/news/633133/photo-tesla-semi-battery-system/

[52] "Samsung 40T 21700 4000mAh 35A Battery," Sriko Batteries. Accessed: Apr. 25, 2023. [Online]. Available: https://srikobatteries.com/product/samsung-40t-21700-4000mah-35a-battery/

[53] D.-M. Kim, P. Benoliel, D.-K. Kim, T. H. Lee, J. W. Park, and J.-P. Hong, "Framework Development of Series Hybrid Powertrain Design for Heavy-Duty Vehicle Considering Driving Conditions," *IEEE Trans. Veh. Technol.*, vol. 68, no. 7, pp. 6468–6480, Jul. 2019, doi: 10.1109/TVT.2019.2914868.

[54] I. Kulikov, A. Kozlov, A. Terenchenko, and K. Karpukhin, "Comparative Study of Powertrain Hybridization for Heavy-Duty Vehicles Equipped with Diesel and Gas Engines," *Energies*, vol. 13, no. 8, p. 2072, Apr. 2020, doi: 10.3390/en13082072.

[55] "X10," Cummins Inc. Accessed: Mar. 02, 2023. [Online]. Available: https://www.cummins.com/engines/x10

[56] D. Dehesa, "STUDY OF CONTROL SCHEMES FOR SERIES HYBRID-ELECTRIC POWERTRAIN FOR UNMANNED AERIAL SYSTEMS," Master of Science in Mechanical Engineering, Louisiana State University and Agricultural and Mechanical College, 2020. doi: 10.31390/gradschool_theses.5221.

[57] P. Sun *et al.*, "Criteria Air Pollutant and Greenhouse Gases Emissions from U.S. Refineries Allocated to Refinery Products," *Environ. Sci. Technol.*, vol. 53, no. 11, pp. 6556–6569, Jun. 2019, doi: 10.1021/acs.est.8b05870.

[58] G. Neely, C. Sharp, M. Pieczko, and J. E. McCarthy, "Simultaneous NO_X and CO_2 Reduction for Meeting Future California Air Resources Board Standards Using a Heavy-Duty Diesel Cylinder Deactivation-NVH Strategy," *SAE Int. J. Engines*, vol. 13, no. 2, pp. 03-13-02–0014, Dec. 2019, doi: 10.4271/03-13-02-0014.

[59] T. Ma *et al.*, "In-use NOx and black carbon emissions from heavy-duty freight diesel vehicles and near-zero emissions natural gas vehicles in California's San Joaquin Air Basin," *Science of The Total Environment*, vol. 907, p. 168188, Jan. 2024, doi: 10.1016/j.scitotenv.2023.168188.

[60] J. Dow, "VW's Electrify America opens California's first 350kW ultra-fast charger, before cars can actually use it," Electrek. Accessed: Oct. 20, 2022. [Online]. Available: https://electrek.co/2018/12/06/electrify-america-first-350kw-charger-california/

[61] "Is your EV battery getting all the energy you pay for?," Recurrent Auto. Accessed: Feb. 05, 2024. [Online]. Available: https://www.recurrentauto.com/research/why-doesnt-your-battery-get-all-the-energy-you-pay-for#:~:text=A%20typical%20Level%202%20home,which%20typically%20maximize%20charging%20efficiency.

[62] J. Schonek, "How big are Power line losses?," Schneider Electric Blog. Accessed: Apr. 28, 2024. [Online]. Available: https://blog.se.com/energy-management-energy-efficiency/2013/03/25/how-big-are-power-line-losses/

[63] R. Campbell, "Increasing the Efficiency of Existing Coal- Fired Power Plants," Congressional Research Service, R43343, Dec. 2013. Accessed: Apr. 19, 2024. [Online]. Available: https://www.ourenergypolicy.org/wp-content/uploads/2014/01/R43343.pdf

[64] National Renewable Energy Laboratory (NREL), "Annual Technology Baseline (ATB)." [Online]. Available: https://atb-archive.nrel.gov/electricity/2018/index.html?t=cg

[65] C. Cleveland, "Power plant efficiency since 1900," Boston University, Jul. 2023. [Online]. Available: https://visualizingenergy.org/power-plant-efficiency-since-1900/

[66] "Nuclear power plant," *Energy Education*. University of Calgary. [Online]. Available: https://energyeducation.ca/encyclopedia/Nuclear_power_plant

[67] "Google Maps," Google Maps. Accessed: Oct. 30, 2022. [Online]. Available: https://www.google.com/maps/@43.073536,-89.4140416,13z

[68] I. Miller, M. Arbabzadeh, and E. Gençer, "Hourly Power Grid Variations, Electric Vehicle Charging Patterns, and Operating Emissions," *Environ. Sci. Technol.*, vol. 54, no. 24, pp. 16071–16085, Dec. 2020, doi: 10.1021/acs.est.0c02312.

[69] "Common United States Truck Routes." Accessed: Oct. 19, 2022. [Online]. Available: https://rockwellscales.com/2017/11/common-united-states-truck-routes/

[70] U.S. Energy Information Administration (EIA), "State Energy Data System (SEDS)." Jun. 20, 2024. [Online]. Available: https://www.eia.gov/state/

[71] "What is Drayage?," iContainers. Accessed: Aug. 15, 2023. [Online]. Available: https://www.icontainers.com/help/what-is-drayage/

[72] "CA Truck Network," State of California. [Online]. Available: https://dot.ca.gov/programs/traffic-operations/legal-truck-access/truck-network-map

[73] "National Highway Freight Network Map and Tables for Indiana, 2022," United States Department of Transportation - Federal Highway Administration (FHWA), Mar. 11, 2023. Accessed: Aug. 15, 2023. [Online]. Available: https://ops.fhwa.dot.gov/freight/infrastructure/ismt/state_maps/states/indiana.htm

[74] G. Finnveden *et al.*, “Recent developments in Life Cycle Assessment,” *Journal of Environmental Management*, vol. 91, no. 1, pp. 1–21, Oct. 2009, doi: 10.1016/j.jenvman.2009.06.018.

[75] H. Ma, F. Balthasar, N. Tait, X. Riera-Palou, and A. Harrison, “A new comparison between the life cycle greenhouse gas emissions of battery electric vehicles and internal combustion vehicles,” *Energy Policy*, vol. 44, pp. 160–173, May 2012, doi: 10.1016/j.enpol.2012.01.034.

[76] J. Short and D. Crownover, “A Comparative Life-Cycle Analysis of Battery Electric, Hydrogen Fuel Cell and Traditional Diesel Trucks.” American Transportation Research Institute.

[77] *The Consolidated Appropriations Act, 2019, Truck Size and Weight Provisions*, Oct. 25, 2019. Accessed: Apr. 05, 2024. [Online]. Available: https://ops.fhwa.dot.gov/freight/pol_plng_finance/policy/fastact/tswprovisions2019/index.htm

[78] J. Mathers, E. Craft, M. Norsworthy, and C. Wolfe, “The Green Freight Handbook A Practical Guide for Developing a Sustainable Freight Transportation Strategy for Business.” Environmental Defense Fund.

[79] H. Hao, Q. Qiao, Z. Liu, F. Zhao, and Y. Chen, “Comparing the life cycle Greenhouse Gas emissions from vehicle production in China and the USA: implications for targeting the reduction opportunities,” *Clean Techn Environ Policy*, vol. 19, no. 5, pp. 1509–1522, Jul. 2017, doi: 10.1007/s10098-016-1325-6.

[80] A. M. Syré, P. Shyposha, L. Freisem, A. Pollak, and D. Göhlich, “Comparative Life Cycle Assessment of Battery and Fuel Cell Electric Cars, Trucks, and Buses,” *WEVJ*, vol. 15, no. 3, p. 114, Mar. 2024, doi: 10.3390/wevj15030114.

[81] O. Winjobi, J. C. Kelly, and Q. Dai, “Life-cycle analysis, by global region, of automotive lithium-ion nickel manganese cobalt batteries of varying nickel content,” *Sustainable Materials and Technologies*, vol. 32, p. e00415, Jul. 2022, doi: 10.1016/j.susmat.2022.e00415.

[82] “Truck maintenance and operation, 2020 and 2021 X15 Efficiency Hardware: QUICK REFERENCE GUIDE.” Cummins Inc., Sep. 22, 2022. [Online]. Available: https://mart.cummins.com/imagelibrary/data/assetfiles/0064269.pdf

[83] “Mobil 1™ 10W-30,” Mobil Canada. [Online]. Available: https://www.mobil.ca/en-ca/lubricants/for-personal-vehicles/personal-vehicle-lubricants/products/mobil-1-10w-30

[84] S. Sutarik, “Run on Less roadshow: Average MPG results,” GeoTab. Accessed: Mar. 04, 2024. [Online]. Available: https://www.geotab.com/blog/run-on-less/

[85] “Nebraska: State Profile and Energy Estimates,” U.S. Energy Information Administration (EIA). Accessed: Feb. 05, 2024. [Online]. Available: https://www.eia.gov/state/?sid=NE#tabs-5

[86] H. Xu, L. Ou, Y. Li, T. R. Hawkins, and M. Wang, “Life Cycle Greenhouse Gas Emissions of Biodiesel and Renewable Diesel Production in the United States,” *Environ. Sci. Technol.*, vol. 56, no. 12, pp. 7512–7521, Jun. 2022, doi: 10.1021/acs.est.2c00289.

[87] N. S. Matthias, T. Wallner, and R. Scarcelli, “A Hydrogen Direct Injection Engine Concept that Exceeds U.S. DOE Light-Duty Efficiency Targets,” *SAE Int. J. Engines*, vol. 5, no. 3, pp. 838–849, Apr. 2012, doi: 10.4271/2012-01-0653.

[88] V. Knop, A. Benkenida, S. Jay, and O. Colin, “Modelling of combustion and nitrogen oxide formation in hydrogen-fuelled internal combustion engines within a 3D CFD code,” *International Journal of Hydrogen Energy*, vol. 33, no. 19, pp. 5083–5097, Oct. 2008, doi: 10.1016/j.ijhydene.2008.06.027.

[89] “Autonomie Suite,” Argonne National Laboratory Vehicle & Mobility Systems Department (VMS). Accessed: Aug. 20, 2023. [Online]. Available: https://vms.taps.anl.gov/tools/autonomie/

[90] J. Ramsey, “Tesla Semi parts diagrams and sample VIN tag hit Twitter,” Autoblog. Accessed: Mar. 10, 2023. [Online]. Available: https://www.autoblog.com/2023/01/03/tesla-semi-weight-load-battery-packs/

[91] M. Lascurain, “Effects of Tire Rolling Resistance On Class 8 Tractor-Trailer Stopping Distance,” National Highway Traffic Safety Administration (NHTSA), DOT HS 812 176, Jun. 2015. Accessed: Aug. 20, 2023. [Online]. Available: https://www.nhtsa.gov/sites/nhtsa.gov/files/812176-tirerollresistclass8tractrtrailrstopdistperfm.pdf

[92] “Freightliner Cascadia® Specs,” Freightline. Accessed: Jul. 18, 2023. [Online]. Available: https://www.freightliner.com/trucks/cascadia/specifications/

[93] P. Subramanian, “Tesla Semi unveiled with tri-motor setup, megawatt charging tech,” Yahoo Finance. Accessed: Jan. 05, 2023. [Online]. Available: https://finance.yahoo.com/news/tesla-semi-unveiled-with-tri-motor-setup-megawatt-charging-tech-121619247.html

[94] “2023 Tesla Model S Plaid - Specifications,” EVSpecifications. Accessed: Jul. 21, 2023. [Online]. Available: https://www.evspecifications.com/en/model/fe20295

[95] “2018 Tesla Model S P100D - Specifications,” EVSpecifications. Accessed: Jul. 21, 2023. [Online]. Available: https://www.evspecifications.com/en/model/399355

[96] F. Lambert, “Tesla is upgrading Model S/X with new, more efficient electric motors,” Electrek. Accessed: Sep. 01, 2023. [Online]. Available: https://electrek.co/2019/04/05/tesla-model-s-new-electric-motors/

[97] M. Kane, “Elon Musk: Tesla Semi Efficiency Is 1.7 kWh/mile,” InsideEVs. Accessed: Aug. 29, 2022. [Online]. Available: https://insideevs.com/news/624904/elon-musk-tesla-semi-efficiency-17kwhmile/

8. Appendix

8.1. Uncertainty analysis parameters and values

Table 8.1.1 *Parameters included in the uncertainty analysis.*

Parameter	Minimum	Maximum	Average	Standard Deviation	Source
Trip start times on 7/1/2023	3,6,9 AM, 12,3,6,9PM, 12AM				-
Gross Indicated Efficiency (GIE) [%]	46.7	47.8	47.25	0.18	Moghadasi et al. [46]
Diesel Feedstock CO_2 [g/L]	150	380	265	38.3	Sun et al. [57]
Diesel Feedstock NO_x [mg/L]	16.8			0	GREET 2023 [7]
Diesel Fuel Stage CO_2 [g/L]	181			0	GREET 2023 [7]
Diesel Fuel Stage NO_x [mg/L]	60.	82.6	71.35	3.75	Sun et al. [57]
Diesel TTW CO_2 [kg/L]	2.683			0	GREET 2023 [7]
Diesel TTW NO_x [g/kWh]	0.22	0.34	0.28	0.02	Neely et al. [58] and Ma et al. [59]
Battery Production CO_2 [kg/kWh]	73	170	121.5	16.17	Syre et al. [80]
Battery Production NO_x [g/kWh]	84.1	97.2	90.65	2.18	Winjobi et al. [81]
Regenerative Braking Efficiency	58%	64%	61%	1%	Solberg [49] and Zhang et al. [50]
Level 3 EV Charger Efficiency	85%	95%	90%	1.5%	Recurrent Auto [61]
Electricity Transmission Efficiency	85%	92%	89%	1.2%	Schonek [62]
Coal Powerplant Efficiency	27%	37%	32%	1.7%	Campbell [63]
Natural Gas Powerplant Efficiency	50%	60%	55%	1.7%	NREL [64]
Petroleum Powerplant Efficiency	30%	32%	31%	0.3%	Cleveland [65]
Nuclear Powerplant Efficiency	33%	37%	35%	0.66%	University of Calgary [66]

8.2. Tesla Semi Validation

The BE truck powertrain model developed in Simulink must be validated to substantiate the simulation results. This was done by having the model replicate the real-world performance of the Tesla Semi. On November 25th, Tesla Motors conducted an independent test with the Tesla Semi. The truck loaded with cargo at a total weight of 81,000 lbs. drove from Tesla's factory in

Fremont, CA to San Diego, CA mostly via the I-5 on a single charge [48]. Tesla showcased a plot of distance covered in miles vs Battery State of charge (SOC). The elevation in feet was also plotted on the right y-axis. Distance, elevation, and SOC data were extracted. No speed data had been published by Tesla and therefore a constant speed of 55 mph had been assumed as the truck was mostly doing highway driving on the I-5. The distance and elevation data were used to calculate the grade.

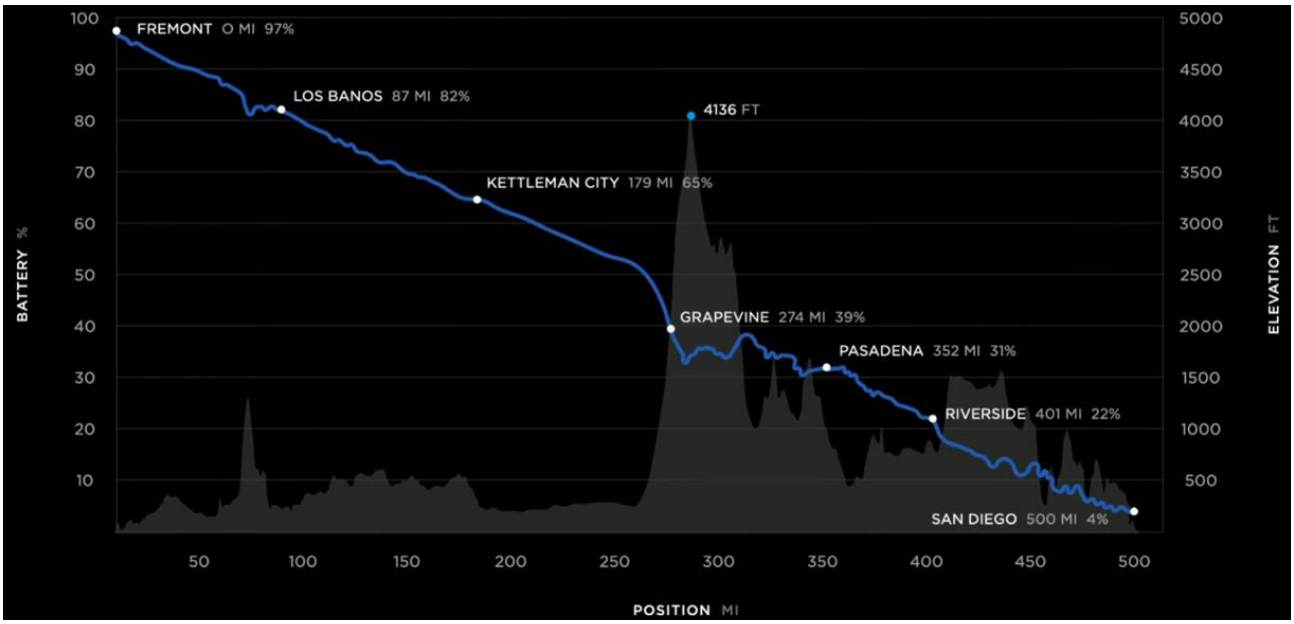

Figure 8.2.1 *Tesla Semi testing data showcased by Tesla Motors [37]*

The BE truck model needed torque and speed data to function, which was not published by Tesla. A vehicle load model from Autonomie, co-developed by Argonne National Laboratory (ANL) and the US Department of Energy (DOE), was utilized for this purpose [89]. The speed assumption and grade from the testing data were used as input for the vehicle load model. In order for the load model to output load torque and motor speed for the Simulink model, a few vehicle specifications were required. According to Tesla, the drag coefficient of the truck is 0.36 [48]. The wheels have a diameter of 40 inches with a width of 275 mm [90]. The rolling resistance was unknown and was therefore selected from a range for semi-trucks which is 0.0044 – 0.0072 [91]. A rolling resistance of 0.0044 led to the best match in results between Tesla's data and the Simulink output.

The parameters of the BE truck model's two motors, battery, and motor controller were modified to best match the Tesla Semi truck. The Tesla Semi has three motors: two motors for the front axle are called the "Accelerator Unit" and a single motor for the rear axle is called the "Highway Unit" [48]. As per their namesake, the "Accelerator Unit" is designed to handle high-load scenarios such as climbing a steep grade, and the "Highway Unit" handles low-load scenarios such as highway driving. The motor controller was designed to fit this operation and have the "Highway Unit" assist the "Accelerator Unit" in very high load cases. The twin "Accelerator Unit" motors at the front axle have been assumed to be a single motor for simplification in the Simulink simulation tool. Tesla Motors claims that the Semi produces three times the power of a conventional diesel semi-truck [48]. Using the power figure of the bestselling diesel semi-truck in the United States, the Freightliner Cascadia [92], the power figure for the Tesla Semi comes out to be 1046 hp (780 kW). The Tesla Semi uses a modified version of the motors from their passenger car, The Tesla Model S [93]. The total power figure calculated also closely matches the specification of the Model S Plaid (750 kW) which further supports the estimate [94]. The Model S has a roughly 70/30 power split between its twin rear motors and its single front motor [95]. This power split was also assumed to be the case for the Tesla Semi with 70% of the total power coming from the Accelerator Unit (735 hp or 548 kW) and 30% of the total power coming from the Highway Unit (315 hp or 235 kW). A maximum motor efficiency of 97% was assumed [96]. The regenerative braking efficiency was set to 64% [49] [50]. The Tesla Semi has a single gear with no transmission [48].

The exact battery pack capacity of the Tesla Semi truck is unknown, but it can be estimated using specifications claimed by Tesla Motors. The Tesla Semi has an efficiency of 1.7 kWhr/mile and is claimed to have a range of 500 miles while fully loaded [97]. This gives us a battery pack capacity estimate of 850 kWh. A safety factor was applied and hence a capacity of 900 kWhr was used. The battery pack consists of Tesla's own 21700 lithium-ion cells [51]. The manufacturer's specification sheet for this cell was not found and therefore the specifications of a similar lithium-ion cell, the Samsung 40T were used. The Samsung cell has similar specs in terms of size, capacity, voltage, and chemistry [52]. The cell specifications have been summarized in **Error! Reference source not found.**. These specifications were used in the Simulink battery model. Tesla claims that the Semi has a 1000 V powertrain [48]. This number, 900 kWhr pack capacity, and the cell voltage were used to calculate 239 cells in series and 209 cells in parallel in the battery pack.

Table 8.2.1 *Comparing cell specifications of Tesla's 2170 and Samsung's 40T cell.*

	Tesla 2170	**Samsung 40T**
Nominal Voltage	3.7 V	3.6 V
Maximum Voltage	4.2 V	4.2 V
Maximum Capacity	4.8 Ah	4 Ah
Internal Resistance	15 mOhm	15 mOhm

The Simulink model was run once all the changes had been made. **Error! Reference source not found.** a compares Tesla's data to the Simulink model's output. The figure also compares and showcases the battery voltage, "Highway", and "Accelerator" motor torque.

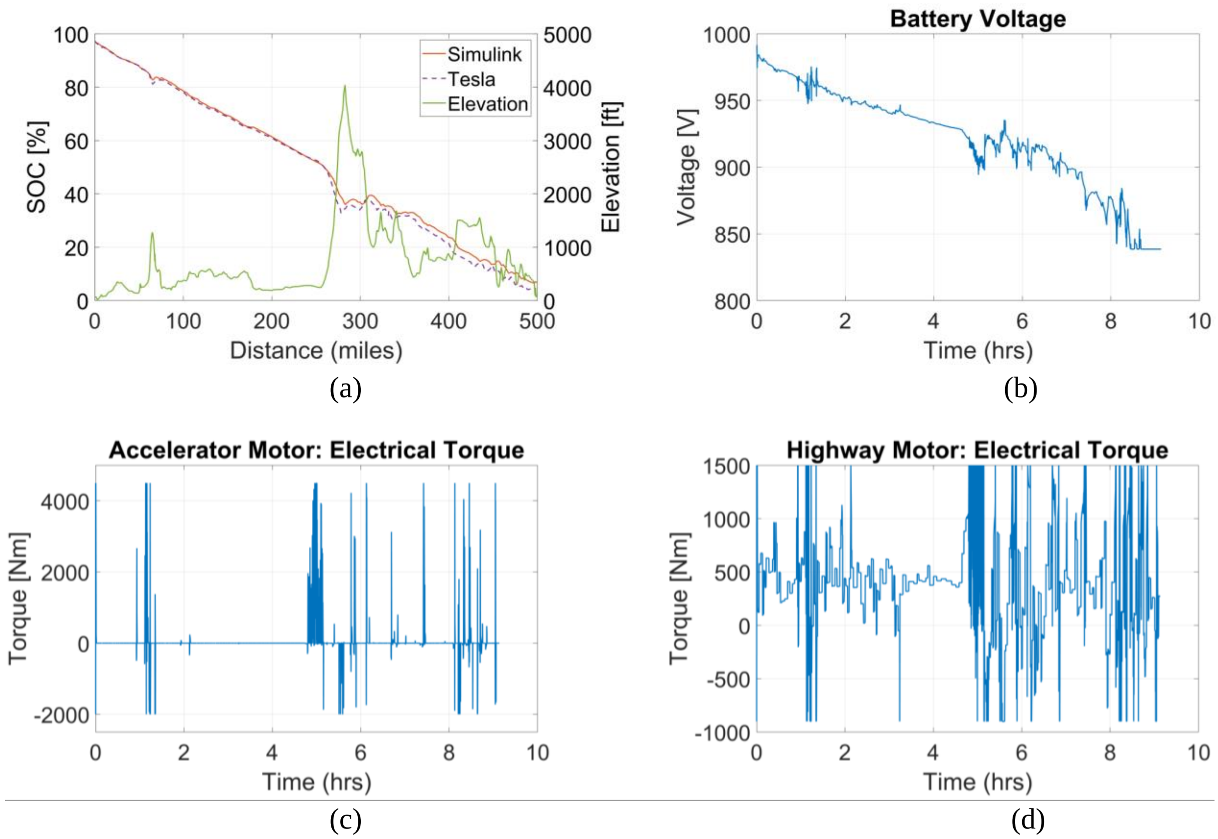

Figure 8.2.2 *Comparing Tesla's data and Simulink model results (a) Replicating data presented by Tesla [30] (b) Battery voltage vs time (c) Accelerator motor electrical torque vs time (d) Highway motor electrical torque vs time.*

8.3. Simulink model component parameters and inputs

Table 8.3.1 *Simulink engine model input parameters and values.*

Parameter	Description	ICE Truck	SHE Truck
Vd	Engine displacement [m^3]	0.0149 (14.9 L)	0.01 (10 L)
GIEta	Gross indicated efficiency [%/100]	0.467-0.479	
Hloss	Engine heat loss as % of fuel energy input [%/100]	0.25	
nC	number of Carbon atoms in fuel	13	
nH	number of Hydrogen atoms in fuel	19.6	
nO	number of Oxygen atoms in fuel	0	
LHV	Fuel LHV [J/kg]	42.2e6 (low-sulfur diesel)	
Comp_IsEta	Compressor isentropic efficiency [%/100]	0.8	
Turbo_IsEta	Turbine isentropic efficiency [%/100]	0.8	
Turbo_MEta	Turbocharger mechanical efficiency	0.98	

Table 8.3.2. *Simulink battery model input parameters and values.*

Parameter	Description	BE Truck	SHE Truck
powertrain_voltage	Powertrain voltage [V]	1000	750
SOC_init	Initial SOC [%]	100	100
N_series	Number of cells in series	239	179
N_parallel	Number of cells in parallel	209	62
Vcell_max	Max battery cell voltage [V]	4.2	
Bat_lambda	Polarization resistance shift	0.1	
Bat_A	Exponential zone amplitude [V]	0.2451	
Bat_B	Charge at the end of exponential zone	0.68068	
Bat_K	Polarization constant [V/Ah]	0.0080297	
tau_bat	Exponential zone time constant [1/Ah]	499	
E0	Battery constant Voltage [V]	3.7	
Bat_Rint	Internal resistance [ohm]	0.015	
Q_max	Maximum cell capacity [Ah]	4.8	

Table 8.3.3. *Simulink motor model input parameters and values.*

Parameter	Description	BE Truck		SHE Truck
T_mot	Design or rated torque [N-m]	1300	3000	2500
Kp_torqcntrl	Torque controller Proportional-gain	35.327		
Ki_torqcntrl	Torque controller Integral-gain	1.1912		
rotor_rpm	Design or rated rotor rpm for sizing [rpm]	5000		
Udc	Design or rated DC bus voltage [V]	1000		750

Table 8.3.4. *Simulink shaft model input parameters and values.*

Parameter	Description	All trucks
I_shaft_PM	Inertia of components connected to shaft [kgm^2]	200
Int_n_PM	Integrator initial condition	10

***Table 8.3.5**. Simulink generator model input parameters and values.*

Parameter	Description	SHE Truck
T_gen	Design or rated torque [N-m]	1900
Kp_GenVCntrl	Voltage controller Proportional-gain	1
Ki_GenVCntrl	Voltage controller Integral-gain	1
rotor_rpm	Design or rated rotor rpm for sizing [rpm]	2000
GenV_Upl	Design or rated DC bus voltage [V]	750
Eta_gen	Generator efficiency [%/100]	0.9

Table 8.3.6. *Simulink motor controller model input parameters and values.*

Parameter	Description	BE truck
Max_T_Mot1	Maximum Torque of larger motor [N-m]	5000
Max_T_Mot2	Maximum Torque of smaller motor [N-m]	1500

Table 8.3.7. *Simulink rule-based controller model input parameters and values.*

Parameter	Description	SHE truck
Nref	Engine speed setpoint [rpm]	1200
Iref	Current setpoint [A]	700
SOCmax	Max state-of-charge (SOC) during charging [%]	80
SOCmin	Min state-of-charge (SOC) during charging [%]	20

8.4. Future grid intensity values

Table 8.4.1. *Future grid CO_2 and NO_x emissions annual reductions and US Average grid intensities from 2023 to 2032.*

	2023	2024	2025	2026	2027	2028	2029	2030	2031	2032
CO_2 reduction from 2023	0%	0.3%	-3.9%	-9.6%	-15.3%	-20.2%	-23.8%	-26%	-27%	-27.6%
US Average CO_2 grid intensity (g/kWh)	470.4	471.9	451.8	425.1	398.4	375.6	358.6	348.1	343.5	340.4
NO_x reduction from 2023	0%	0.2%	-4%	-9.5%	-15%	-19.7%	-23.2%	-25.3%	-26.3%	-27%
US Average NO_x grid intensity (mg/kWh)	369.5	370.1	354.8	334.5	314.1	296.8	283.9	275.9	272.3	269.9

8.5. BE Truck Recharging Stops

Table 8.5.1. *Charging stops for BE truck along long-haul route with journey starting at 6:00 am (7/1/2023)*

Location on Map	Location	Balancing Authorities	Charging Period	CO_2 Emitted [kg]	NO_x Emitted [g]
1	Lovelock, NV	NEVP (Nevada Power Company)	12:39 pm - 2:44 pm (7/1/2023)	269	212
2	Elko, NV	NEVP (Nevada Power Company)	7:38 pm - 9:11 pm (7/1/2023)	327	259
3	Evanston, WY	PACE (PacifiCorp East)	2:10 am - 4:18 am (7/2/2023)	542	414
4	Rock Springs, WY	PACE (PacifiCorp East)	6:05 am - 6:45 am (7/2/2023)	164	125
5	Cheyenne, WY	PACE (PacifiCorp East)	12:28 pm - 2:15 pm (7/2/2023)	443	337
6	Lexington, NE	SWPP (Southwest Power Pool)	9:35 pm - 11:44 pm (7/2/2023)	467	358
7	Council Bluffs, IA	MISO (Midcontinent Independent System Operator, Inc)	3:27 am - 4:56 am (7/3/2023)	307	237
8	Williamsburg, IA	MISO (Midcontinent Independent System Operator, Inc)	9:54 am -11:24 am (7/3/2023)	370	286
B	Chicago, IL	PJM (PJM Interconnection, LLC)	5:19 pm -7:17 pm (7/3/2023)	389	303
1	Williamsburg, IA	MISO (Midcontinent Independent System Operator, Inc)	12:25 am - 2:04 am (7/4/2023)	374	289
2	Lincoln, NE	SWPP (Southwest Power Pool)	6:41 am - 8:36 am (7/4/2023)	418	321
3	Ogalla, NE	SWPP (Southwest Power Pool)	2:29 pm - 4:22 pm (7/4/2023)	429	329
4	Cheyenne, WY	PACE (PacifiCorp East)	7:59 pm -9:06 pm (7/4/2023)	364	277
5	Rock Springs, WY	PACE (PacifiCorp East)	3:21 am - 5:21 am (7/5/2023)	666	507
6	Salt Lake City, UT	PACE (PacifiCorp East)	8:21 am - 9:31 am (7/5/2023)	274	209
7	Battle Mountain, NV	NEVP (Nevada Power Company)	3:48 pm - 5:54 pm (7/5/2023)	309	244
8	Truckee, CA	CISO (California Independent System Operator)	11:10 pm (7/5/2023) - 12:52 am (7/6/2023)	191	150
A	San Francisco, CA	CISO (California Independent System Operator)	5:30 am - 6:55 am (7/6/2023)	159	125

Table 8.5.2. *Charging stops for BE truck along the California drayage route with journey starting at 6:00 am (7/1/2023)*

Location on Map	Location	Balancing Authorities	Charging Period	CO_2 Emitted [kg]	NO_x Emitted [g]
1	Burbank, CA	CISO (California Independent System Operator)	10:11 pm (7/1/2023) - 12:09 am (7/2/2023)	253	200
2	Bakersfield, CA	CISO (California Independent System Operator)	6:31 pm - 8:42 pm (7/2/2023)	126	100
3	Santa Clarita, CA	CISO (California Independent System Operator)	2:14 pm - 4:20 pm (7/3/2023)	211	167
4	Culver City, CA	CISO (California Independent System Operator)	6:37 pm - 8:24 pm (7/4/2023)	178	140
5	Bakersfield, CA	CISO (California Independent System Operator)	11:30 pm (7/4/2023) - 1:11 am (7/5/2023)	100	78
6	Journey End	CISO (California Independent System Operator)	12:05 am - 1:58 am (7/5/2023)	212	166

Table 8.5.3. *Charging stops for BE truck along the Indiana drayage route with journey starting at 6:00 am (7/1/2023)*

Location on Map	Location	Balancing Authorities	Charging Period	CO_2 Emitted [kg]	NO_x Emitted [g]
1	Indianapolis, IN	MISO (Midcontinent Independent System Operator, Inc)	8:11 pm - 10:10 pm (7/1/2023)	489	378
2	Indianapolis, IN	MISO (Midcontinent Independent System Operator, Inc)	12:40 pm - 2:29 pm (7/2/2023)	441	341
3	Clarksville, IN	MISO (Midcontinent Independent System Operator, Inc)	5:11 am - 7:18 am (7/3/2023)	475	368
4	Indianapolis, IN	MISO (Midcontinent Independent System Operator, Inc)	11:09 pm (7/3/2023) - 1:02 pm (7/4/2023)	430	333
5	Indianapolis, IN	MISO (Midcontinent Independent System Operator, Inc)	1:51 am - 3:44 pm (7/4/2023)	460	355
6	Journey Ends	MISO (Midcontinent Independent System Operator, Inc)	1:08 am - 2:16 am (7/5/2023)	244	189

8.6. ICE Truck Refueling Stops

Table 8.6.1. *Location and periods of all refueling stops for the ICE truck on the long-haul trip with journey starting at 6:00 am (7/1/2023)*

Location on Map	Location	Fueling Period
1	Grantsville, UT	8:56 pm – 9:00 pm (7/1/2023)
2	Sutherland, NE	12:33 pm – 12:36 pm (7/2/2023)
B	Chicago, IL	2:16 am – 2:19 am (7/3/2023)
1	Kearny, NE	5:46 pm – 5:49 pm (7/3/2023)
2	Evanston, WY	8:15 am – 8:18 am (7/4/2023)
3	Dutch Flat, CA	11:44 pm – 11:48 pm (7/4/2023)
A	San Francisco, CA	12:38 am – 12:40 am (7/5/2023)

Table 8.6.2. *Location and periods of all refueling stops for the ICE truck on the California drayage trip with journey starting at 6:00 am (7/1/2023)*

Location on Map	Location	Fueling Period
1	Santa Clarita, CA	4:30 pm – 4:34 pm (7/2/2023)
2	Bakersfield, CA	3:03 am – 3:06 am (7/4/2023)

Table 8.6.3. *Location and periods of all refueling stops for the ICE truck on the Indiana drayage trip with journey starting at 6:00 am (7/1/2023)*

Location on Map	Location	Fueling Period
1	Lafayette, IN	4:30 pm – 4:34 pm (7/2/2023)
2	Clarksville, IN	3:03 am – 3:06 am (7/4/2023)

8.7. SHE Truck Refueling Stops

Table 8.7.1. *Location and periods of all refueling stops for SHE truck on the long-haul trip with journey starting at 6:00 am (7/1/2023)*

Location on Map	Location	Fueling Period
1	Buford, WY	5:39 pm – 5:42 am (7/2/2023)
B	Chicago, IL	2:18 am – 2:21 am (7/3/2023)
2	Walcott, WY	1:31 am – 1:34 am (7/4/2023)
A	San Francisco, CA	12:12 am – 12:16 am (7/5/2023)

Table 8.7.2. *Location and periods of all refueling stops for SHE truck on the California drayage trip with journey starting at 6:00 am (7/1/2023)*

Location on Map	Location	Fueling Period
1	Burbank, CA	5:15 pm – 5:18 pm (7/3/2023)

Table 8.7.3. *Location and periods of all refueling stops for SHE truck on the Indiana drayage trip with journey starting at 6:00 am (7/1/2023)*

Location on Map	Location	Fueling Period
1	Indianapolis, IN	5:15 pm – 5:18 pm (7/3/2023)